

論文 / 著書情報
Article / Book Information

題目(和文)	
Title(English)	A study on lateral-type spin-photodiodes based on metal-insulator-semiconductor junctions
著者(和文)	ロカロネルクリスチャンインタル
Author(English)	Ronel Christian Intal Roca
出典(和文)	学位:博士(工学), 学位授与機関:東京工業大学, 報告番号:甲第10660号, 授与年月日:2017年9月20日, 学位の種別:課程博士, 審査員:宗片 比呂夫,筒井 一生,宮本 智之,渡辺 正裕,菅原 聡
Citation(English)	Degree:Doctor (Engineering), Conferring organization: Tokyo Institute of Technology, Report number:甲第10660号, Conferred date:2017/9/20, Degree Type:Course doctor, Examiner:,,,,
学位種別(和文)	博士論文
Type(English)	Doctoral Thesis

A study on lateral-type spin-photodiodes based on metal-insulator-semiconductor junctions

Ronel Christian Intal Roca

Doctoral Dissertation

submitted to the

Department of Electronics and Applied Physics
Interdisciplinary Graduate School of Science and Engineering
Tokyo Institute of Technology

in partial fulfillment of the requirements for the degree of
Doctor of Engineering

August 2017

Doctoral supervisor: Professor Hiro Munekata

Doctoral Thesis Committee:

Thesis Supervisor:

Hiro Munekata

Professor

Department of Physics

Tokyo Institute of Technology

Thesis Examiners:

Kazuo Tsutsui

Professor

Department of Electrical and Electronics

Engineering

Tokyo Institute of Technology

Tomoyuki Miyamoto

Associate Professor

Department of Electrical and Electronics

Engineering

Tokyo Institute of Technology

Satoshi Sugahara

Associate Professor

Department of Electrical and Electronics

Engineering

Tokyo Institute of Technology

Masahiro Watanabe

Associate Professor

Department of Electrical and Electronics

Engineering

Tokyo Institute of Technology

Doctoral Defense Schedule

Preliminary Examination: May 26, 2017

Public Defense: July 24, 2017

Final Defense: August 2, 2017

Final Submission: August 24, 2017

Abstract

A comprehensive study on lateral-type spin-photodiodes based on metal-insulator-semiconductor junctions operating at room temperature is presented. The performance of a simple cleaved-edge Fe/ AlO_x /p-GaAs Schottky junction spin-photodiode has been investigated. In addition to conventional sidewall illumination experiments, oblique angle surface illumination measurements were also carried out. Experimental results show a spin collection efficiency F of 0.14% for sidewall illumination, and an improved F of 1.3% for oblique angle surface illumination. A simulation model based on the optical selection rules, carrier and spin drift-diffusion, and spin dependent tunneling has also been developed. Simulation results show a good match with experiment data for oblique angle illumination. A further comparison of experiment and simulation results suggests that the low F for side illumination has been caused either by the damage to the AlO_x tunnel barrier at the cleaved edge or by magnetic edge curling. Furthermore, a novel Fe/ AlO_x /p-InGaAs spin-photodiode design with a refracting facet has also been presented. An experimental F of 0.4% has been achieved for the fabricated refracting-facet spin-photodiodes. This value is the highest so far for purely lateral spin-photodiodes. In addition to experiments, a simulation model for the refracting-facet spin-photodiode involving the optical selection rules, carrier and spin collection probability, and spin-dependent tunneling, has also been developed. Simulation results show that a potential F up to 19% is achievable for the proposed spin-photodiode design. A comparison of the simulation and experimental results suggests that the quality of the Fe electrode is poor, and that an improvement of the electrode quality will lead to a significantly enhancement in the F . With these results, a significantly improved understanding of the physics of lateral spin-photodiodes, as well as a practical demonstration of a lateral spin-photodiode, has been achieved.

Table of Contents

Title.....	1
Abstract	3
List of Figures	6
1. Introduction	9
1.1 Background	9
1.2 Semiconductor spintronics.....	11
1.3 Spin-optoelectronics	13
1.4 Spin-photodiodes.....	15
1.5 Scope and organization of this dissertation.....	17
References	18
2. Physics of spin-photodiodes	22
2.1 Device characteristics of spin-photodiodes	22
2.2 Basic semiconductor physics.....	24
2.3 Semiconductor physics in Schottky photodiodes.....	27
2.4 Transport of carriers in a semiconductor.....	29
2.5 Spin dynamics in a semiconductor	30
2.6 Optical spin injection into semiconductors.....	32
2.7 Electrical spin injection into semiconductors	33
2.8 Electrical spin detection from semiconductors.....	38
References	41
3. Experimental techniques	45
3.1 Molecular beam epitaxy	45
3.2 Device fabrication	46
3.3 Helicity-resolved photocurrent measurement.....	48
3.4 Lock-in Technique.....	50
References	52
4. Simulation of spin-photodiodes	53
4.1 General approach in simulation of spin-photodiodes.....	53
4.2 Photogeneration of spin-polarized carriers.....	55
4.3 Transport of charge and spins	57
4.4 Spin dependent tunneling.....	68
References	69
5. Investigation of a cleaved-edge spin-photodiode with oblique angle surface illumination	72
5.1 Introduction	72
5.2 Methodology	73
5.3 Results and discussions.....	77

5.4 Conclusions	84
References	84
6. Refracting-facet spin-photodiode.....	86
6.1 Introduction	86
6.2 Methodology	87
6.3 Results and discussions.....	93
6.4 Conclusions	101
References	101
7. Conclusions	103
Acknowledgements	105
List of publications and presentations.....	106
Curriculum Vitae	107

List of Figures

Figure 1.1 Schematic diagrams of an MTJ in the (a) parallel state and (b) anti-parallel state.	10
Figure 1.2 Schematic diagrams of various methods of introducing spins into semiconductors: (a) dilute magnetic semiconductor, (b) electrical spin injection, and (c) optical spin injection.	12
Figure 1.3 Schematic diagrams of the process of producing CPL from (a) a conventional LED and (b) a spin-LED.	14
Figure 1.4 Schematic diagrams of the CPL-resolved photocurrent measurement using (a) a conventional PD and (b) a spin-PD.	15
Figure 1.5 Schematic diagrams of (a) a vertical spin-PD and (b) a lateral spin-PD.	17
Figure 2.1 Energy band diagram of (a) an undoped or intrinsic semiconductor, (b) a n-type semiconductor, and (c) a p-type semiconductor.	25
Figure 2.2 Schematic diagrams of (a) optical pumping and (b) electrical pumping.	26
Figure 2.3 Energy band diagrams of (a) p-type and (b) n-type Schottky diodes.....	27
Figure 2.4 Working principle of p-type Schottky photodiode.....	28
Figure 2.5 Energy band diagram of an intrinsic semiconductor with spin-polarized carriers.	31
Figure 2.6 Spin optical selection rules for zincblende and diamond structure semiconductors.	32
Figure 2.7 (a) Schematic of a FM-SC junction. (b) Voltage profile for the junction assuming the bulk FM polarization is fully injected across. (c) Voltage profile for the junction assuming the spin splitting voltage is continuous across the junction.	33
Figure 2.8 Schematic diagrams of densities of states for the two spin bands in the case of	

(a) a FM and (b) a SC.....	34
Figure 2.9 Voltage profiles for (a) a DMS-SC junction and (b) a FM-TB-SC junction.....	37
Figure 2.10 Schematic diagram of the density of states at the tunnel contact in a spin-PD.	40
Figure 2.11 Power curve of a spin-PD plotted along the load line of the tunnel contact. The photocurrent is the intersection of the power curve and load line.....	40
Figure 3.1 Schematic diagram of an MBE chamber during crystal growth.....	46
Figure 3.2 Schematic diagram of the device fabrication process for the spin-PD in Chapter 6.	47
Figure 3.3 Schematic diagram of the helicity-resolved photocurrent measurement setup.	48
Figure 4.1 Diagram of a spin photodiode and a summary of proposed models. (a) A simple model using photogeneration and transport distance, but assumes an ideal contact. (b) An elaborate theoretical model that simultaneously solves the spin-polarized carrier transport and the tunneling effect. (c) A drift-diffusion model that only considers the transport inside the semiconductor (device contacts were not considered). (d) The proposed model in this work: a modular model that combines transport in the semiconductor and tunneling.....	54
Figure 4.2 Schematic diagrams of (a) a vertical-type GaAs spin-PD and (b) a cleaved-edge lateral-type GaAs spin-PD.....	58
Figure 4.3 Profiles of (a) Δn and (b) Δs as functions of z . Inset of (b): rescaled (zoomed in) plot of Δs . Parameters used are $\Phi_0 = 3.4 \times 10^{19} \text{ cm}^{-2} \text{ s}^{-1}$, $A = 1.26 \times 10^{-3} \text{ cm}^2$, $D = 62 \text{ cm}^2/\text{s}$, $\alpha = 10^4 \text{ cm}^{-1}$, ²⁰ $T = 0.1$, ²¹ $E = 2.1 \times 10^5 \text{ V/cm}$, $\mu = 2400 \text{ cm}^2 \text{ V}^{-1} \text{ s}^{-1}$, ²⁶ $\tau_{rec} = 7.15 \times 10^{-8} \text{ s}$, ²⁵ $\tau_s = 2.33 \times 10^{-10} \text{ s}$. ²⁷	60
Figure 4.4 Profiles of (a) Δn and (b) Δs as functions of x and z . Parameters used are $\Phi_0 = 3.4 \times 10^{19} \text{ cm}^{-2} \text{ s}^{-1}$, $A = 1.26 \times 10^{-3} \text{ cm}^2$, $D = 62 \text{ cm}^2/\text{s}$, $\alpha = 10^4 \text{ cm}^{-1}$, ²⁰ $T = 0.1$, ²¹ $E = 2.1 \times 10^5 \text{ V/cm}$, $\mu = 2400 \text{ cm}^2 \text{ V}^{-1} \text{ s}^{-1}$, ²⁶ $\tau_{rec} = 7.15 \times 10^{-8} \text{ s}$, ²⁵ $\tau_s = 2.33 \times 10^{-10} \text{ s}$, ²⁷ and $S = 7.7 \times 10^7 \text{ cm/s}$. ²⁹	68
Figure 5.1 (a) Schematic cross section of the sample structure: from the top, 10-nm Au, 5-nm Ti, 50-nm Fe, 1-nm AlO_x , 100-nm Be-doped GaAs epilayer, and a p-GaAs:Zn (001) substrate. (b) Schematic of the helicity-resolved photocurrent measurement setup. Linearly polarized light from a 20mW laser was converted to CPL using LP and a QWP. The CPL beam was focused on the sample using a lens with the focal length $f = 50 \text{ cm}$. (c) Calculated transmittance of the two orthogonal linear polarizations as functions of the incidence angle θ . Inset: Schematic of refraction through the top metal layers for oblique-angle illumination with θ_{GaAs} , the angle of a light beam inside the GaAs.	73
Figure 5.2 Schematic diagram of the simulation geometry for (a) sidewall illumination and (b) oblique angle illumination.	76
Figure 5.3 Profile of the photogenerated charges Δn and spins Δs in the z - x plane for sidewall illumination. Arrows indicate the flow of charges and spins inferred from the gradient of the profile: the diffusion current $J_e, \text{ diff}$, the surface recombination current $J_e, \text{ surf}$, the photocurrent $J_e, \text{ ph}$, and the spin photocurrent J_e, s	77
Figure 5.4 Profile of the photogenerated spins Δs along the z -direction for oblique angle illumination. Inset: Corresponding profile of the photogenerated charges Δn . Arrows indicate the flow of charges and spins inferred from the gradient of the profile: the photocurrent $J_e, \text{ ph}$, and the spin photocurrent J_e, s	78

Figure 5.5 (a) Profiles of photocurrent as a function of time for two opposite applied fields $H = \pm 1.35$ kOe for sidewall illumination. (b) F as a function of applied field for sidewall illumination plotted with magnetization hysteresis loop. (c) Profiles of photocurrent as a function of time for two opposite remanent magnetization direction +Rem and -Rem for oblique angle illumination. (d) F as a function of applied field for sidewall illumination plotted with magnetization hysteresis loop. No applied voltage was applied for all measurements. 79

Figure 5.6 F as a function of applied field for oblique angle illumination plotted with magnetization hysteresis loop for (a) $V = -1$ [V] and (b) $V = +1$ [V]. 80

Figure 5.7 (a) Measured F vs applied field H for different incidence angles. (b) Simulated values for the photocurrent I_{ph} , helicity-dependent photocurrent ΔI , and F as functions of the surface recombination velocity S and the surface recombination time $T_{surf} = \delta/S$. 81

Figure 5.8 (a) Experimental photocurrent I_{ph} (blue diamonds), helicity-dependent photocurrent ΔI (red squares), and F (green triangles), simulated photocurrent I_{ph} (blue lines), helicity-dependent photocurrent ΔI (red lines), and F (green lines) plotted as functions of the beam position. Dashed and solid lines correspond to calculations with and without contribution from light hitting the sidewall, respectively. (b) A schematic diagram of the beam scan in the spin-PD. 82

Figure 6.1 (a) Schematic of the refracting-facet spin-PD. (b) A cross-sectional SEM image of the fabricated refracting facet. (c) A bird's-eye-view SEM image of the fabricated refracting-facet spin-PD. 87

Figure 6.2 (a) Schematic of the helicity-resolved photocurrent measurement setup. (b) Image of an actual spin-PD chip mounted on a sample holder. (c) A bird's-eye-view SEM image of the fabricated refracting-facet spin-PD. 88

Figure 6.3 (a) Calculated photocurrent I_{ph} and spin-photocurrent I_s as functions of the active layer thickness d . (b) Calculated F as a function of d 93

Figure 6.4 Calculated spin-photocurrent I_s (a) and F (b) for θ_{facet} : 65° (blue), 75° (red), and 85° (green) as functions of the active layer thickness d 94

Figure 6.5 (a) Temporal plot of the measured photocurrent I_{ph} from a spin-PD with $d = 0.4 \mu\text{m}$ for two remanent magnetization states. (b) Plot of I_{ph} and F as functions of the wavelength of the incident beam. 95

Figure 6.6 (a) Plot of I_{ph} and ΔI as functions of the applied bias voltage for the spin-PD with $d = 0.4 \mu\text{m}$. (b) Plot of F as a function of bias. (c) Plot of the estimated EQE and f as functions of bias. 97

Figure 6.7 (a) Temporal plot of the measured photocurrent I_{ph} from a spin-PD with $d = 0.04 \mu\text{m}$ for two remanent magnetization states. Profiles were vertically separated for visibility. (b) Plot of I_{ph} and ΔI as functions of the applied bias voltage. (c) Plot of F as a function of bias. (d) Plot of the estimated EQE and f as functions of bias. 98

1. Introduction

1.1 Background

Spintronics is an emerging field that aims to circumvent the limitations of conventional electronics by utilizing the spin degree of freedom. Through the years, there have been several proposed spintronic devices. Some of these are analogs of their conventional charge (electron) based counterparts. To name a few, examples include: the spin-transistor,¹ spin-Esaki diode,² spin-light-emitting diode (spin-LED),^{3,4} and spin-photodiode (spin-PD).⁵ As their names suggest, these devices are modified versions of their conventional semiconductor device counterparts. By exploiting the spin degree of freedom (also referred to as the spin property of electrons), additional functionalities can be achieved. In the case of the spin-LED for example, circularly polarized emission can be realized without the need for external optical components. These devices will be discussed in more detail in the proceeding sections.

There are other novel spintronic devices that have no conventional device counterparts. One of the best examples is the magnetic tunnel junction (MTJ).⁶⁻⁸ In essence, these are junctions formed by inserting a thin insulating layer between two ferromagnetic metal layers, thereby creating a ferromagnet-insulator-ferromagnet (FM-I-FM) junction. It was shown by Julliere⁶ that, in the first order, the tunneling probability, and hence the conductance across the junction, depends on the relative orientation of the magnetizations of the two ferromagnetic layers. In particular, the conductance is maximum when the magnetizations of

the two ferromagnetic layers are aligned parallel to each other, and lowest when aligned anti-parallel to each other (as shown in Fig. 1.1). This effect is known as tunnel magnetoresistance (TMR). Due to their wide adoption as magnetic field sensors (also called read sensors) in hard disk drives (HDDs), the MTJ is one of the most commercially successful spintronic devices.⁹

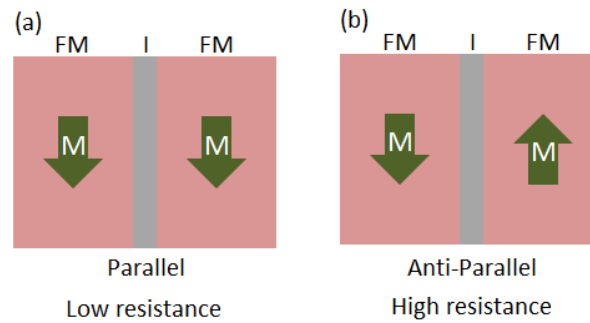


Figure 1.1 Schematic diagrams of an MTJ in the (a) parallel state and (b) anti-parallel state.

The TMR effect is just one kind of magnetoresistance phenomena. Others examples include: anisotropic magnetoresistance (AMR) and giant magnetoresistance (GMR). Both of which have also been applied commercially as read sensors to HDDs.⁹ TMR and GMR are sometimes also referred to as spin valve effects.¹⁰

A related spintronic device that has found some degree of commercial success is the magnetoresistive random access memory (MRAM). This is a hybrid device, in which an MTJ is combined with conventional silicon transistors.¹¹⁻¹⁴ Whereas conventional random-access memory (RAM) cells use the gate charge in silicon transistors (or in the case of dynamic RAMs, charge in capacitors), which require a constant power supply to keep data, MRAM cells rely on the remanent magnetization property of MTJs to store data, hence require no power to maintain data. This feature makes the MRAM a non-volatile type of memory.

There are many more novel spintronic devices, such as magnonic devices^{15,16} and spin-photonic devices.¹⁷⁻²¹ Magnons are spin waves which can be generated, guided, manipulated, and detected. Many logic circuit implementations using magnons have already been proposed.¹⁶ Proponents of magnonics argue that magnon circuit implementations tend to be much simpler than their conventional electronic counterparts. Furthermore, magnon transport does not involve the flow of charge carriers. Therefore, energy loss due to Joule (resistive) heating is minimized. However, commercial adoption and practical implementations of magnon devices have yet to be demonstrated. Spin-photonic devices, on

the other hand, aim to control and utilize the photon helicity (spin angular momentum). One proposed implementation of such a device involves the use of metamaterials.¹⁷ Metamaterials are nanostructures engineered to interact with electromagnetic waves so as to achieve a desired response. Using such materials the photon spins can be manipulated. Other examples of materials that can be used to manipulate the photon spin are semiconductors doped with magnetic impurities^{19,20} and quantum dots (QD).²¹

From this brief overview, it can be seen that spintronics, as a field, has a very wide range of potential application. The common feature among spintronic devices is that they possess functionalities that are very difficult (or sometimes impossible) to achieve through conventional electronics. From here on, the discussion will be focused on semiconductor spintronics. In particular a detailed discussion about spin-optoelectronics will be presented in proceeding sections.

1.2 Semiconductor spintronics

In this section, the discussion will be limited to classical semiconductor spintronics. There is actually a whole separate emerging field called quantum spintronics that deals with: spin coherence, entanglement, and manipulation of quantum states; and have applications in quantum computing and quantum cryptography; which is different from the topic of the present work.²³

In contrast with the relatively wide commercial adoption of MTJ devices (also referred to as metallic spintronic devices),²³ semiconductor based spintronic devices have yet to be commercially realized. There are two main reasons for this. Firstly, conventional semiconductors are inherently not spin-polarized. At equilibrium, the number of spin-up and spin-down carriers in a conventional semiconductor are equal. In order to introduce spin-polarization into the semiconductor, we would need to somehow generate a non-equal amount of spin-up and spin-down carriers. Naturally, any spin-polarization that is introduced would automatically put the semiconductor into a non-equilibrium state. Hence, the system will try to restore equilibrium via a process called spin-relaxation,²⁴ in which the majority spins are converted (reoriented) into minority spin until spin-up and spin-down numbers become equal again. Typically, this process takes place in a very fast pace. In GaAs for example, the spin relaxation time is in the order of 1 ns at room temperature.²⁵ With spins depolarizing at such a fast rate, it is difficult to produce a significant amount of spin-polarization in conventional semiconductors.

Secondly, the process of introducing spin-polarization into the semiconductor efficiently

is a problem of its own, and there is currently no consensus on the best approach. One approach is to introduce magnetic impurities into the conventional semiconductor.^{26,27} These materials are sometime referred to as dilute magnetic semiconductors (DMS). The main motivation is that, as opposed to a conventional semiconductor, a ferromagnetic semiconductor has a spontaneous spin-polarization at equilibrium. Perhaps the most famous example of these is GaMnAs.²⁸ Ferromagnetic GaMnAs has been achieved, but only at low temperature (with Curie temp typically below 110 K). Of course, there are other materials presently being investigated. In particular, wide bandgap magnetic semiconductors can potentially exhibit room temperature ferromagnetism.²⁹ There are also other unresolved issues in DMS materials. One weak point of DMS is that, due to their high doping levels, their carrier transport and optical properties are inferior to those of their conventional counterparts.²³ If we were to make a purely DMS-based LED, for example, it would suffer from very poor quantum efficiency.

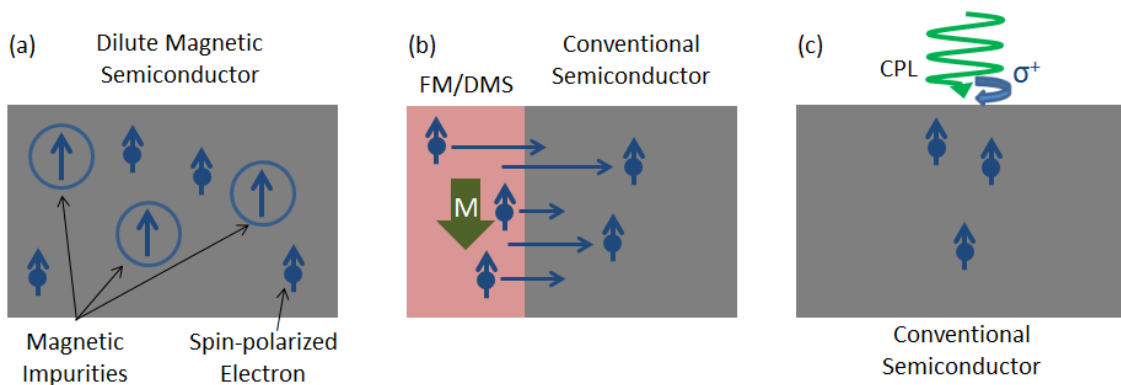


Figure 1.2 Schematic diagrams of various methods of introducing spins into semiconductors: (a) dilute magnetic semiconductor, (b) electrical spin injection, and (c) optical spin injection.

Perhaps a better approach in introducing spin-polarization to semiconductors is using a hybrid structure. That is, the active part of the device would be made from conventional semiconductors, while a spin-injector somewhere else would be the source of spin. This method is referred to as electrical spin injection. Ferromagnetic metals (FM), such as Fe that have an equilibrium spin-polarization, can be used as the spin-injector.³⁰⁻³² In addition, DMS materials can also be used as spin-injector.³³ In the case of a FM spin-injector, there is another issue that needs to be address in order to achieve effective spin injection.³⁴ This would be discussed in detail in Ch. 2. In device level studies, electrical spin injection is one of the most popular approaches.

Yet another approach in introducing spin-polarization is using the spin angular momentum light. When circularly polarized light is incident in a zinc-blende or diamond structure semiconductor, the photogenerated electrons in the conduction band of the semiconductor is spin-polarized (spin-polarized holes in the valence band are also generated but they tend to rapidly depolarize).^{35,36} This method of introducing spin polarization can be accomplished without using a spin-injector material, and hence, is compatible with most conventional semiconductor processes. The main disadvantage of this approach is that it only works effectively for direct bandgap materials such as GaAs and Ge, but not Si. This optical spin orientation (optical spin injection) approach has become popular recently,³⁷ due to its compatibility with vertical external-cavity surface-emitting lasers (VECSELs). Furthermore, optical spin injection is one of the foundations of spin-PD operation. In this case, optical spin injection is not used simply to introduce spins into the semiconductor, but rather, in order to convert the CPL information of the light into spin polarization. The spin polarization in turn can then be converted into current through a process called electrical spin detection (which is the other foundation of spin-PD operation).

Overall, bulk of the effort in semiconductor spintronics has been on generation of spin in conventional semiconductors (i.e. spin injection),^{38,39} and this still continues to be as one of the biggest bottlenecks in the development of spintronics in semiconductor devices. In contrast, the various advantages and new applications of spin-polarized semiconductor devices (should they be realized) have already been explored relatively well.^{40,41}

1.3 Spin-optoelectronics

Having briefly discussed spins in semiconductors, we now move on to spin-optoelectronics. Optoelectronics is usually considered to be a subfield of photonics. In conventional optoelectronics, charge (electrical) signals are converted into light (optical fields) or *vice versa*.⁴² This is accomplished by utilizing the effect of optical fields to the electronic properties of semiconductors. Examples of conventional optoelectronic devices include: semiconductor devices that convert current to light, e.g. laser diodes (LD) and light-emitting diodes (LED), and semiconductor devices that convert light to current or voltage, e.g. photodiodes (PD) and phototransistors (PT).

Let us first consider the conventional LED. A conventional LED converts charge current into light via the spontaneous emission process. This process produces output light that is unpolarized (or randomly polarized). For some applications, the polarization state of the output light is of no consequence, but for other applications, specific polarization states such

as circularly polarized light (CPL) may be required. These include, for example, CPL based imaging.⁴³ If we wanted to convert light from a conventional LED into CPL, we would need at least two other optical components [i.e. a linear polarizer (LP) and a quarter-wave plate (QWP)] and these two external components would form bulk of the setup [as shown in Fig. 1.3 (a)]. Furthermore, it would be difficult to miniaturize setup. This is where spin-optoelectronics come in.

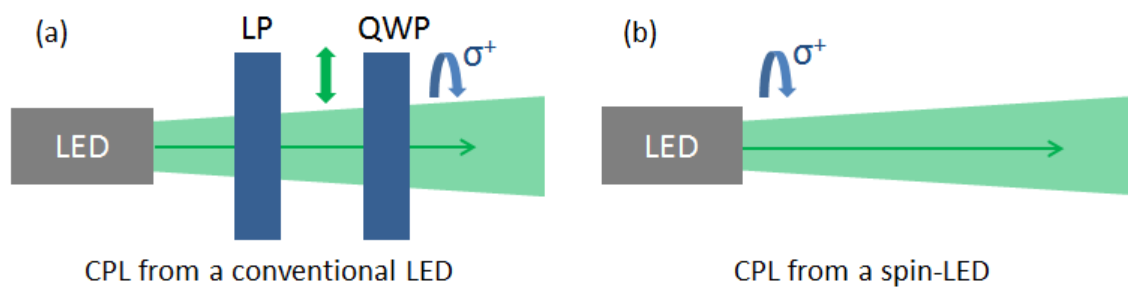


Figure 1.3 Schematic diagrams of the process of producing CPL from (a) a conventional LED and (b) a spin-LED.

One proposed monolithic CPL source is the spin-LED (a spin-optoelectronic device). Output light from a spin-LED is already circularly polarized (or more accurately, elliptically polarized,³⁹ since presently, 100% CPL output has yet to be demonstrated). This allows the spin-LED to be a compact CPL emitter [as shown in Fig. 1.3 (b)], which can easily be miniaturized. Of course there are other candidate monolithic CPL emitters, such as chiral nanostructures,⁴⁴ polymer semiconductors,⁴⁵ spiral plasmonics,⁴⁶ spiral cavity lasers,⁴⁷ and valley polarization of monolayer materials.⁴⁸ The main advantage of spin-LEDs compared to these competing technologies is that, the spin-LED is mostly compatible with the conventional semiconductor processes. Whereas competing technologies involve complicated nanostructures or new materials that would complicate the device fabrication process, a spin-LED involves a conventional semiconductor active region that has a relatively mature fabrication process. Another advantage of the spin-LED is the tunability of the helicity of the output CPL. Helicity tuning is accomplished by simply changing the magnetization orientation of the spin injector in the spin-LED. This cannot be accomplished with chiral nanostructures, polymer semiconductors, plasmonics, and spiral cavities. The main disadvantage of spin-LEDs is the rather complicated fabrication of the spin-injector. The spin-injector is typically composed of a thin (preferably crystalline) insulating layer and a ferromagnetic metal (preferably of similarly crystalline quality). Each of these need to be deposited or grown via different methods. In this simple example, we have shown some of

the advantages and disadvantages of a spin-optoelectronic device, the spin-LED.

1.4 Spin-photodiodes

We have finally arrived at the topic of the present work: spin-photodiodes (spin-PD). In order to understand what a spin-PD can do, let us first consider a conventional photodiode (PD). The purpose of a conventional PD is essentially the inverse of the LED: to convert light (optical field) into current. Photocurrent is the resulting current when light is incident into a PD, which is a result of the optical absorption process in semiconductors. For a given active area, the photocurrent is a function of the intensity of the incident light, regardless of the polarization state of the incident light (note here that some PDs do have indirect linear polarization dependencies due to, for instance, an aperture transmittance that depend on the linear polarization direction, but there is almost always no CPL helicity dependence). Incidentally, there are applications where we want to measure not just the intensity of the light, but also the helicity and degree of circular polarization (CPL polarimetry).⁴³ Since a conventional PD cannot resolve the degree of circular polarization, CPL polarimetry is typically accomplished by using at least two additional external components (i.e. a linear polarizer and a quarter-wave plate), and again these components tend to make the bulk of the size polarimeter system [as shown in Fig. 1.4 (a)]. In addition, in order to perform a full measurement, the QWP has to be rotated in order to resolve the CPL components. This mechanical motion is slow.

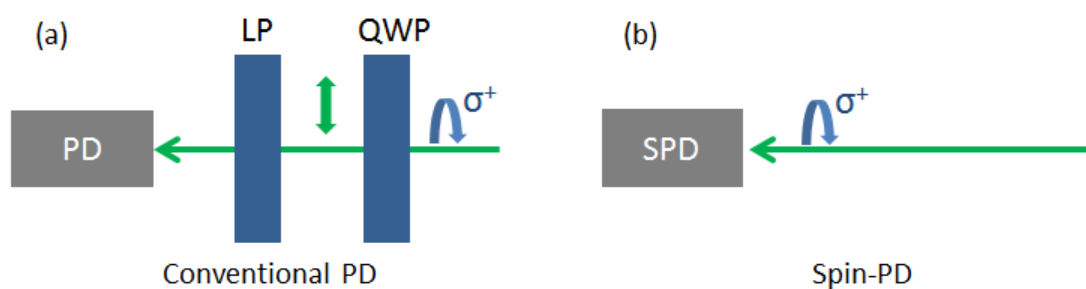


Figure 1.4 Schematic diagrams of the CPL-resolved photocurrent measurement using (a) a conventional PD and (b) a spin-PD.

A spin-optoelectronic device that can potentially simultaneously measure the intensity and degree of circular polarization of light is the spin-PD. In contrast to that of a conventional LED, the photocurrent in a spin-LED depends on both the intensity and the degree of circular polarization of the incident light.⁴⁹ This allows the spin-PD to be used as a

monolithic CPL polarimeter [as shown in Fig. 1.4 (b)]. Of course, there are also competing technologies and candidate devices for monolithic CPL detectors. These include chiral metamaterials,⁵⁰ chiral organic transistors,⁵¹ and inverse spin Hall effect (ISHE) based sensors.⁵² Analogous to the spin-LED, whereas these competing technologies involve either complicated structures or new materials, the fabrication process of spin-PDs is relatively mature. In addition, the quantum efficiencies of chiral organic semiconductors and ISHE sensors tend to be low (in the order of 0.1%). Metamaterials have a higher efficiencies by require nanofabrication. Another key advantage of the spin-PD is the ability to change the orientation of the magnetization of the spin detection contact. This allows for another degree of freedom in the measurement, so that modulation techniques such as lock-in amplification are possible. These are not possible with other competing technologies. The main weak point of spin-PDs is their ability to convert helicity information into a change in current tend to be low (the current highest is about 5%).

Typically, a spin-PD is composed of two parts: a conventional semiconductor PD, which serves as the light detector, and a spin detection contact, which would convert the photogenerated spins into a measurable change in the photocurrent. This hybrid structure was greatly inspired by spin-LEDs, where a similar approach has been used. Since semiconductor PDs are relatively well established, bulk of the research effort is being exerted into developing an efficient spin detection contact. A typical spin detection contact is a tunnel contact composed of a ferromagnetic metal and a tunnel barrier. The detailed physics of the spin detection process will be discussed in more detail in Ch. 2.

Moreover, spin-PDs generally come in two geometries or configurations: vertical and lateral (as shown Fig. 1.5). By far the more common type is the vertical or surface-illuminated type.^{5,49,53-55} In a vertical-type spin-PD, light is incident into the top surface of the device, usually through the top ferromagnetic contact. In this configuration, the spin detection contact has to be magnetized along the out-of-plane direction. This is accomplished by either using a ferromagnet that exhibit perpendicular magnetic anisotropy (PMA) or by applying a large out-of-plane magnetic field. The former restricts the choice of materials, while the latter is difficult and impractical for a monolithic device. In addition, because the light is transmitted through the top metal, light suffers severe losses due to the absorption in the metal contact, which lowers the quantum efficiency of the spin-PD, and a magneto-circular dichroism (MCD) component is introduced to the photocurrent. In particular, the MCD signal can mask the actual spin signal unless appropriately accounted for.⁵⁶ On the other hand, there are also several advantages of the vertical geometry, such as

large active area, relatively simple fabrication, and inherently high collection efficiency of photogenerated spins. Their geometry is also ideal for fiber-optic coupling and optical interconnects. These advantages are the main reason why most of the studies up to now have been focused on the vertical spin-PD.^{5,49,53-55}

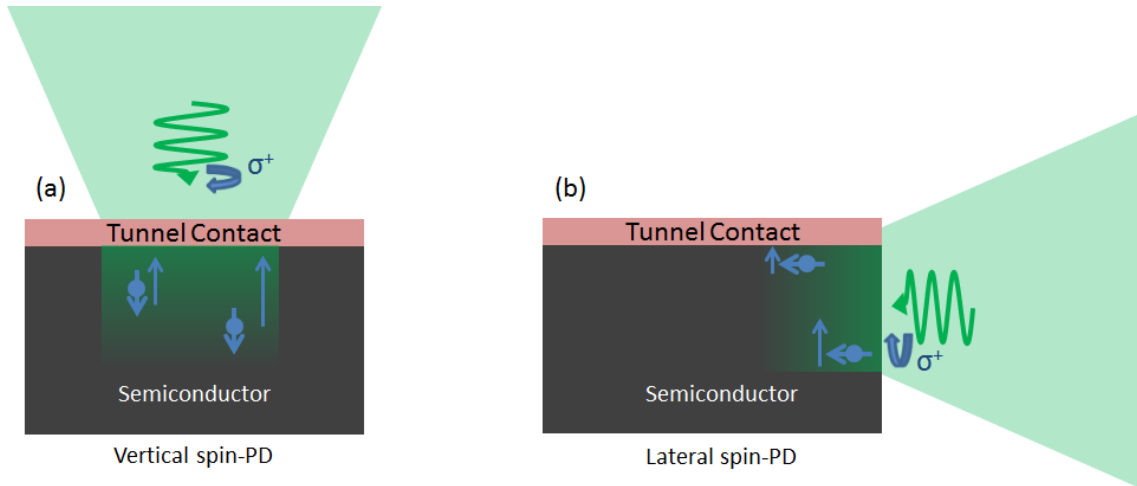


Figure 1.5 Schematic diagrams of (a) a vertical spin-PD and (b) a lateral spin-PD.

Compared to the vertical spin-PD, the lateral or side-illuminated spin-PD is far less common. In fact, in my knowledge, there are only a few reports on lateral spin-PD.^{57,58,59} The main reason for this scarcity is the difficulty of measuring the spin signal and the inherently lower spin collection efficiency in the lateral geometry. Of course, there are also several advantages of the lateral spin-PD. These include: the PMA requirement for the ferromagnetic contact is relaxed; there is no MCD component in the photocurrent; and the lateral geometry is better suited for intra-chip device-to-device communication. In particular, the last point is important for monolithic optoelectronic integrated circuit applications. In addition, because the light does not pass through the top metal, a higher quantum efficiency is expected. In spite of these advantages, the development of lateral spin-PDs has been rather slow (in part because of the discouraging difficulty of getting experimental results). More detailed discussion about lateral spin-PDs will be presented in the proceeding chapter.

1.5 Scope and organization of this dissertation

This dissertation presents a comprehensive study on lateral-type spin-PD based on ferromagnet-insulator-semiconductor junctions. Theoretical calculations as well as experimental results will be presented. The purpose of the study is to analyze and improve the performance of lateral spin-PDs. In particular, the goals of the study are as follows: first,

to experimentally investigate the origin of the low F in lateral spin-PDs; second, to develop a simulation model for lateral spin-PDs; and third, to improve the design of lateral spin-PDs with the following in mind: room temperature operation, no external magnetic field operation, improved quantum efficiency, and improved F .

In chapter 1, a general background of spintronics, as well as the place where spin-PDs fit in the overall picture, has been discussed. In particular, a literature survey of previous reports on spin-PDs, as well as competing technologies, has been presented.

In chapter 2, a two-pronged discussion about the empirical characteristics of a spin-PD and the theoretical aspects of a spin-PD will be discussed. In particular, at the device level, the key characteristics of spin-PD like the helicity-dependent photocurrent, photocurrent asymmetry, and the figure of merit will be presented. In the theoretical side, discussions on a brief background of relevant semiconductor physics, spin dynamics in semiconductors, spin transport physics, and various methods of spin injection and detection will be presented.

In chapter 3, the basic experimental techniques used in the study will be discussed. Crystal growth using molecular beam epitaxy, which was used to make the wafers in this study, will be introduced. The device fabrication process of the refracting-facet spin-PDs, including an important wet etching step, will also be discussed. Finally, a general description of the helicity-resolved photocurrent measurement technique used to characterize the fabricated spin-PDs will be presented.

In chapter 4, a detailed discussion about the method of simulating spin-PDs will be presented. The step-by-step process in modelling spin-PDs, starting with optical spin injection, through spin transport, and finally spin dependent tunneling, will be discussed.

In chapter 5, a study of a simple cleaved edge lateral spin-PD will be presented. Here, in addition with conventional edge illumination measurement results, results from oblique angle surface illumination measurements will also be presented. On top of experimental results, model calculation results will also be presented.

In chapter 6, a study of a novel lateral spin-PD structure, a refracting-facet spin-PD, will be presented. Results from both model calculations and experimental measurements will be presented.

In chapter 7, overall conclusions, as well as future prospects, will be presented. The overall success of the study in meeting its goals will also be discussed.

References

- 1) S. Datta and B. Das, Appl. Phys. Lett. **56**, 665 (1990).

- 2) M. Kohda, Y. Ohno, K. Takamura, F. Matsukura, and H. Ohno, *Jpn. J. Appl. Phys.* **40**, L1274 (2001).
- 3) H. Kioseoglou and A. Petrou, *J. Low Temp. Phys.* **169**, 324 (2012).
- 4) R. Fiederling, M. Keim, G. Reuscher, W. Ossau, G. Schmidt, A. Waag, and L. W. Molenkamp, *Nature* **402**, 787 (1999).
- 5) A. Hirohata, Y. B. Xu, C. M. Guertler, J. A. C. Bland, and S. N. Holmes, *Phys. Rev. B* **63**, 104425 (2001).
- 6) M. Julliere, *Phys. Lett. A* **54**, 225 (1975).
- 7) T. Miyazaki and N. Tezuka, *J. Magn. Magn. Mater.* **139**, L231 (1995).
- 8) J. S. Moodera, L. R. Kinder, T. M. Wong, and R. Meservey, *Phys. Rev. Lett.* **74**, 3273 (1995).
- 9) C. Chappert, A. Fert, and F. N. Van Dau, *Nat. Mater.* **6**, 813 (2007).
- 10) P. P. Freitas, F. Silva, N. J. Oliveira, L. V. Melo, L. Costa, N. Almeida, *Sens. Actuators A Phys.* **81**, 2 (2000).
- 11) S. S. P. Parkin, K. P. Roche, M. G. Samant, P. M. Rice, R. B. Beyers, R. E. Scheuerlein, E. J. O'Sullivan, S. L. Brown, J. Bucchigano, D. W. Abraham, Y. Lu, M. Rooks, P. L. Trouilloud, R. A. Wanner, and W. J. Gallagher, *J. Appl. Phys.* **85**, 5828 (1999).
- 12) S. Tehrani, E. Chen, M. Durlam, M. De Herrera, J. M. Slaughter, J. Shi, and G. Kerszykowski, *J. Appl. Phys.* **85**, 5822 (1999).
- 13) J. G. Zhu, Y. Zheng, and G. A. Prinz, *J. Appl. Phys.* **87**, 6668 (2000).
- 14) S. Tehrani, J. M. Slaughter, M. De Herrera, B. N. Engel, N. D. Rizzo, J. Salter, M. Durlam, R. W. Dave, J. Janesky, B. Butcher, K. Smith, and G. Grynkewich, *Proc. IEEE* **91**, 703 (2003).
- 15) V. V. Kruglyak, S. O. Demokritov, and D. Grundler, *J. Phys. D: Appl. Phys.* **43**, 264001 (2010).
- 16) A. Khitun, M. Bao, and K. L. Wang, *J. Phys. D: Appl. Phys.* **43**, 264005 (2010).
- 17) N. Shitrit, I. Yulevich, E. Maguid, D. Ozeri, D. Veksler, V. Kleiner, and E. Hasman, *Science* **340**, 724 (2013).
- 18) X. Ling, X. Yi, X. Zhou, Y. Liu, W. Shu, H. Lou, and S. Wen, *Appl. Phys. Lett.* **105**, 151101 (2014).
- 19) H. Nakayama, H. Ohta, and E. Kulatov, *Physica B* **302-303**, 419 (2001).
- 20) R. P. Panguluri, B. Nadgorny, T. Wojtowicz, W. L. Lim, X. Liu, and J. K. Furdyna, *Appl. Phys. Lett.* **84**, 4947 (2004).
- 21) W. B. Gao, A. Imamoglu, H. Bernien, and R. Hanson, *Nat. Photon.* **9**, 363 (2015).

- 22) D. D. Awschalom, L. C. Bassett, A. S., Dzurak, E. L. Hu, J. R. Petta, *Science* **339**, 1174 (2013).
- 23) D. D. Awschalom and M. Flatte, *Nat. Phys.* **3**, 153 (2007).
- 24) M. I. Dyakonov, *Spin Physics in Semiconductors* (Springer-Verlag Berlin Heidelberg, 2008) Ch. 1, p. 17.
- 25) I. Favorskiy, D. Vu, E. Peytavit, S. Arscott, D. Paget, and A. C. H. Rowe, *Rev. Sci. Instrum.* **81**, 103902 (2010).
- 26) K. Sato and H. Katayama-Yoshida, *Semicond. Sci. Technol.* **17**, 367 (2002).
- 27) J. K. Furdyna, *J. Appl. Phys.* **64**, R29 (1988).
- 28) S. Lee, J. H. Chung, X. Liu, J. K. Furdyna, and B. J. Kirby, *Mater. Today* **12**, 14 (2009).
- 29) S. J. Pearton, C. R. Abernathy, D. P. Norton, A. F. Herbard, Y. D. Park, L. A. Boatner, J. D. Budai, *Mater. Sci. Eng. R* **40**, 137 (2003).
- 30) R. J. Soulen Jr., J. M. Byers, M. S. Osofsky, B. Nadgorny, T. Ambrose, S. F. Cheng, P. R. Broussard, C. T. Tanaka, J. Nowak, J. S. Moodera, A. Barry, J. M. D. Coey, *Science* **282**, 85 (1998).
- 31) M. B. Stearns, *J. Magn. Magn. Mater.* **5**, 167 (1977).
- 32) T. Miyazaki and N. Tezuka, *J. Magn. Magn. Mater.* **139**, 231 (1995).
- 33) G. Schmidt and L. W. Molenkamp, *Physica E* **10**, 484 (2001).
- 34) E. I. Rashba, *Phys. Rev. B* **62**, R16267 (2000).
- 35) B. I. Zakharchenya, V. G. Fleisher, R. I. Dzhioev, Yu. P. Veshchunov, and I. B. Rusanov, *JETP Lett.* **13**, 137 (1971).
- 36) M. I. Dyakonov and V. I. Perel, *JETP* **38**, 177 (1974).
- 37) A. Joly, J. Frougier, G. Baili, M. Alouini, J. M. George, I. Sagnes, and D. Dolfi, *Proc. SPIE* **9755**, 97551E (2016).
- 38) J. Fabian, A. Matos-Abiague, C. Ertler, P. Stano, and I. Zutic, *ACTA Phys. Slovaca* **57**, 565 (2007).
- 39) G. Schmidt, *J. Phys. D: Appl. Phys.* **38**, R107 (2005).
- 40) I. Sugahara, Y. Tamura, Y. Shuto, and S. Yamamoto, *Devices and Applications: Spin Transistors and Spin Logic Devices in Handbook of Spintronics* (Springer Netherlands, 2014) eds. Y. Xu, D. D. Awschalom, J. Nitta, p. 1 – 31.
- 41) I. Zutic and P. E Faria Jr., *Nat. Nanotechnol.* **9**, 750 (2014).
- 42) Chuang, S. L., *Physics of Optoelectronic Devices* (John Wiley & Sons New York, 1995), Ch. 1, pp. 1 – 8.
- 43) I. Meglinski, C. Macdonald, A. Doronin, and M. Eccles, *OSA Technical Digest*, paper

BM2A.4 (2013).

- 44) K. Konishi, M. Nomura, N. Kumagai, S. Iwamoto, Y. Arakawa, and M. Kuwata-Gonokami, *Phys. Rev. Lett.* **106**, 057402 (2011).
- 45) E. Peeters, M. P. T. Christiaans, R. A. J. Janssen, H. F. M. Schoo, H. P. J. M. Dekkers, and E. W. Meijer, *J. Am. Chem. Soc.* **119**, 9909 (1997).
- 46) K. A. Bachman, J. J. Peltzer, P. D. Flammer, T. E. Furtak, R. T. Collins, and R. E. Hollingsworth, *Opt. Express* **20**, 1308 (2012).
- 47) C. L. Yu, S. W. Liao, Y. H. Hsiao, H. C. Kuo, and M. H. Shih, CLEO, OSA Technical Digest, STh1C.4 (2017).
- 48) H. Zeng, J. Dai, W. Yao, D. Xiao, and X. Cui, *Nat. Nanotechnol.* **7**, 490 (2012).
- 49) C. Rinaldi, M. Cantoni, D. Petti, A. Sottocorno, M. Leone, N. Caffrey, S. Sanvito, and R. Bertacco, *Adv. Mater.* **24**, 3037 (2012).
- 50) W. Li, J. Coppens, L. V. Besteiro, W. Wang, A. O. Govorov, and J. Valentine, *Nat. Comm.* **6**, 8379 (2015).
- 51) Y. Yang, R. C. da Costa, M. J. Fuchter, and A. J. Campbell, *Nat. Photon.* **7**, 634 (2013).
- 52) S. K. Khamari, S. Porwal, S. M. Oak, and T. K. Sharma, *Appl. Phys. Lett.* **107**, 072108 (2015).
- 53) S. Hövel, N. C. Gerhardt, M. R. Hofmann, F.-Y. Lo, D. Reuter, A. D. Wieck, E. Schuster, W. Keune, H. Wende, O. Petracic, and K. Westerholt, *Appl. Phys. Lett.* **92**, 242102 (2008).
- 54) T. Taniyama, G. Wastlbauer, A. Ionescu, M. Tselepi, and J. A. C. Bland, *Phys. Rev. B* **68**, 134430 (2003).
- 55) Y. J. Park, M. C. Hickey, M. J. Van Veenhuizen, J. Chang, D. Heiman, C. H. Perry, and J. S. Moodera, *J. Phys.: Condens. Matter* **23**, 116002 (2011).
- 56) S. J. Steinmueller, C. M. Gürtler, G. Wastlbauer, and J. A. C. Bland, *Phys. Rev. B* **72**, 045301 (2005).
- 57) H. Ikeda, N. Nishizawa, K. Nishibayashi, and H. Munekata, *J. Magn. Soc. Jpn.* **38**, 151 (2014).
- 58) R. C. Roca, N. Nishizawa, K. Nishibayashi, and H. Munekata, *Jpn. J. Appl. Phys.* **56**, 04CN05 (2017).
- 59) R. C. Roca, N. Nishizawa, K. Nishibayashi, and H. Munekata, submitted to JJAP (2017).

2. Physics of spin-photodiodes

2.1 Device characteristics of spin-photodiodes

Without initially going through the microscopic physics in a spin-PD, let us first try to discuss the macroscopic device characteristics of a spin-PD. The theoretical framework of spin-PDs will be discussed in the proceeding sections. Here we will take a phenomenological approach. The defining characteristic of a spin-PD is that its photocurrent I_{ph} depends not only to the power of the incident light but also to the helicity or circular polarization of the incident light. Whereas for a conventional photodiode, the photocurrent I_{ph} is only dependent on the power of the incident light (i.e. $I_{ph} = R_{ph} \cdot P_0$, the photocurrent I_{ph} is directly related to the incident power through the responsivity R_{ph}); for a spin-PD, the photocurrent $I_{ph} = I_{ph}(P_c)$ where P_c is the degree of circular polarization. The degree of circular polarization of light P_c is usually defined as^{1,2}

$$P_c = \frac{P^+ - P^-}{P^+ + P^-} = \frac{W^+ - W^-}{W^+ + W^-} = \frac{\Phi^+ - \Phi^-}{\Phi^+ + \Phi^-}. \quad (2.1)$$

Here, P^+ and P^- are the power (in watts) of the right σ^+ and left σ^- CPL components of the incident light, respectively. P_c can also be defined in terms of the intensities W^\pm (in W/cm^2) or photon fluxes Φ^\pm (in number of photons / $cm^2 \cdot s$) since these quantities are proportional to the power. Particularly, P_c can take any value between 1 and -1 . Since the component of I_{ph} that depends on helicity is typically small, we can linearize the helicity-dependent component and express I_{ph} as follows

$$I_{ph}(P_c) = I_{ph,0} + I_{hd} \cdot P_c. \quad (2.2)$$

Here, the first term $I_{ph,0}$ is the component of I_{ph} that does not depend on the helicity, the second term $I_{hd} \cdot P_c$ is the helicity-dependent component of I_{ph} , and I_{hd} is a positive constant that describes the strength of the helicity dependence. Note that the $I_{ph,0}$ term is essentially identical to the photocurrent from conventional photodiode, i.e. $I_{ph,0} = R_{ph} \cdot P_0$. Furthermore, the highest physically possible value for I_{hd} is $I_{ph,0}$. There is a theoretical explanation for this (which will be discussed later). For now, let us argue that since $|P_c| \leq 1$, and if I_{hd} becomes larger than $I_{ph,0}$, we can have a negative photocurrent (which cannot happen). Therefore, it has to be that $I_{hd} \leq I_{ph,0}$. In typical spin-PD, I_{hd} is a small fraction of $I_{ph,0}$.² We can therefore rewrite Eq. (2.1) as follows

$$I_{ph}(P_c) = I_{ph,0} + I_{ph,0} \cdot A_{SF} \cdot P_c = I_{ph,0} \cdot (1 + A_{SF} \cdot P_c). \quad (2.3)$$

Here, we have expressed I_{hd} as a fraction of $I_{ph,0}$, and $A_{SF} = I_{hd}/I_{ph,0}$ is a constant (usually express in %) that describes the relative strength of the helicity-dependent component to the helicity-independent component of I_{ph} . A_{SF} has historically been referred to as the spin filtering asymmetry (since the asymmetry in the photocurrent comes from spin filtering or spin transport).³ A high A_{SF} is generally considered desirable for spin-PD applications. The A_{SF} of a spin-PD depends on the design, geometry, as well as the materials properties of the spin-PD. A_{SF} can experimentally be obtained by measuring the photocurrents from σ^+ and σ^- illumination and then taking their difference, $\Delta I = I_{ph}(P_c = 1) - I_{ph}(P_c = -1)$. ΔI is referred to as the helicity-dependent photocurrent and is described by

$$\Delta I = I_{ph}(P_c = 1) - I_{ph}(P_c = -1) = 2A_{SF} \cdot I_{ph,0}. \quad (2.4)$$

In order to isolate A_{SF} , we need to divide ΔI with $I_{ph,0}$. This can be done by taking the average of the photocurrents from σ^+ and σ^- illumination, $I_{ph,0} = [I_{ph}(P_c = 1) + I_{ph}(P_c = -1)]/2$. Combining this with Eq. (2.3) leads us to

$$F = \frac{\Delta I}{I_{ph,0}} = \frac{2[I_{ph}(P_c=1) - I_{ph}(P_c=-1)]}{I_{ph}(P_c=1) + I_{ph}(P_c=-1)} = 2A_{SF}. \quad (2.4)$$

Here, F is the figure of merit of a spin-PD² (also sometimes referred to as the spin conversion efficiency). F is the main performance metric of a spin-PD. Due to recent advancements, F as high as 5% has been achieved at room temperature for vertical spin-PD.^{2,4}

One thing to note is that F can be defined in several ways. For instance, in Ref. 2, F was defined as the ratio of ΔI to the photocurrent for linearly polarized illumination. This is also correct and is equivalent to the definition of Eq. (2.4). In later chapters of this work,

shorthand notations may be used such as $\frac{\Delta I}{I_{ph}}$ instead of $\frac{\Delta I}{I_{ph,0}}$, $I_{ph}(\sigma^\pm)$ instead of $I_{ph}(\pm 1)$, or $P_c(\sigma^\pm)$ instead of $P_c = \pm 1$. These refer to the same things (and are possibly redundant), but using them can sometimes provide better context.

As a final point, one often overlooked ‘‘advantage’’ of a vertical-type spin-PD is the effect of magneto-circular dichroism to the photocurrent. In general, the effect of MCD is small (within a few percent at most), but since A_{SF} also tends to be small (also within a few percent), MCD can be significant. In the presence of MCD Eq. (2.2) becomes

$$I_{ph}(P_c) = [I_{ph,0} \cdot (1 + A_{SF} \cdot P_c)] \cdot (1 + D \cdot P_c) \approx I_{ph,0} \cdot [1 + (A_{SF} + D) \cdot P_c]. \quad (2.5)$$

Here, D is the MCD component of the photocurrent,^{2,5} and we have dropped the higher order term. The corresponding F with MCD is

$$F = \frac{\Delta I}{I_{ph,0}} = 2(A_{SF} + D). \quad (2.6)$$

It can clearly be seen that D tends to improve F , and we have to keep this in mind to make a fair comparison between vertical-type and lateral-type spin-PDs. In the present study, owing to the lateral geometry, data is generally free of MCD (except for the oblique angle illumination in Ch. 5), but this discussion has been presented for the sake of completeness.

2.2 Basic semiconductor physics

Semiconductor devices have become ubiquitous in recent times. The property that distinguishes semiconductors from other materials such as metals and insulators is the existence of an energy band gap in their electronic band structures. Show in Fig. 2.1 (a) is a schematic of the band structure of an intrinsic (undoped) semiconductor.^{6,7} In the band gap, there are no electronic states. The size of the energy gap E_g depends on the material. Common values at room temperature are: 1.12 eV for Si,⁸ 1.42 eV for GaAs,⁹ 0.66 eV for Ge,¹⁰ and 3.2 eV for GaN.¹¹ Below the gap is the valence band (VB) and above the gap is the conduction band (CB). There are electronic states in the VB and CB.

For an undoped semiconductor, the Fermi level is located at the middle of the gap. The Fermi level (also referred to as the chemical potential) determines which states are filled with electrons and which ones are vacant. At absolute zero, all the states below the Fermi level are filled with electrons, while all the states above the Fermi level are vacant. In this case the entire VB is filled with electrons, while the entire CB is empty. At temperatures other than absolute zero, some of the electrons in the VB are thermally excited to the CB. The amount of thermally excite electrons in the CB is described by Fermi-Dirac statistics.¹²

In particular, the electron concentration at the bottom edge of the CB is

$$n = \int D(E) \cdot f(E, E_F) dE \approx D_{CB} \cdot \exp\left(\frac{E_F - E_C}{k_B T}\right). \quad (2.7)$$

Here, n is electron concentration at the CB, $D(E)$ is the density of states, D_{CB} is the effective density of states at the edge of the CB E_C , $f(E, E_F) = \left[\exp\left(\frac{E - E_F}{k_B T}\right) + 1\right]^{-1}$ is the Fermi-Dirac distribution function, which we can be approximated (for most semiconductors at room temperature) as the Boltzmann distribution $\exp\left(\frac{E_C - E_F}{k_B T}\right)$, k_B is the Boltzmann constant, and T is the temperature. $k_B T$ is referred to as the thermal energy, which is about 25.7 eV at room temperature. Note also that for an intrinsic semiconductor, due to conservation of charge, electrons thermally excited into the CB leave behind vacancies or holes in the VB. The number of holes p is equal to n . Furthermore, only electrons in the CB n and holes in the VB p can actually participate in conduction. Electrons locked deep in the VB cannot move because there is no place for them to move since all of the states are occupied.

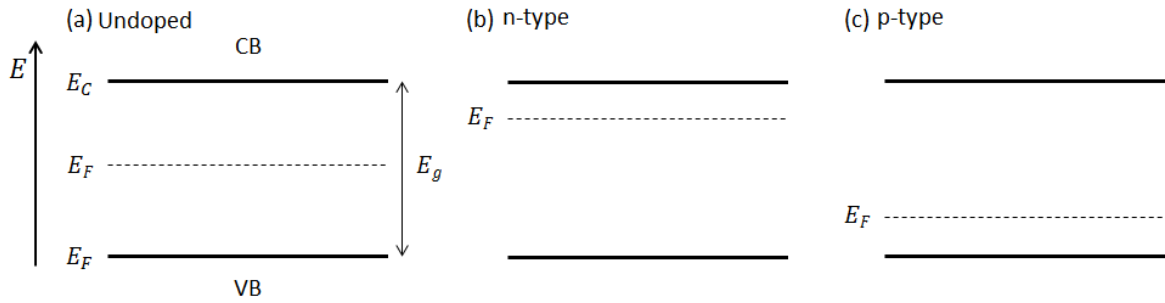


Figure 2.1 Energy band diagram of (a) an undoped or intrinsic semiconductor, (b) a n-type semiconductor, and (c) a p-type semiconductor.

For an intrinsic semiconductor at room temperature, n is typically small, about $2 \times 10^6 \text{ cm}^{-3}$ for GaAs (this is called the intrinsic carrier concentration n_i). In comparison, a typical commercial n-type GaAs substrate has n of about 10^{18} cm^{-3} . This high electron concentration is needed in order to achieve a low resistivity. So that one can imagine that an undoped semiconductor is practically an insulator.

In order to increase the number of carriers in a semiconductor, impurities can be added to the semiconductor crystal. This process is referred to as doping. In the case of GaAs, Si can be added in small amounts. Silicon atoms act as donors giving off electrons each to the CB. The net effect of this is that the Fermi level would move towards the CB, forming an n-type semiconductor as shown in Fig. 2.1 (b). From Eq. (2.7) we immediately recognize that as

E_F becomes closer to E_C , the exponential term increases. The doping level is described by the concentration of donor atoms N_D . For moderate doping levels, up to about $N_D \approx 10^{17} \text{ cm}^{-3}$, all of the donor atoms are ionized, so that the n is approximately equal to N_D . Similarly, doping GaAs with Be or Zn atoms, which act as electron acceptors, creates holes in the VB, where the density of holes p is approximately equal to the density of acceptor atoms N_A . This leads to the movement of the Fermi level towards the VB edge, forming a p-type semiconductor, as shown in Fig 2.1 (c).

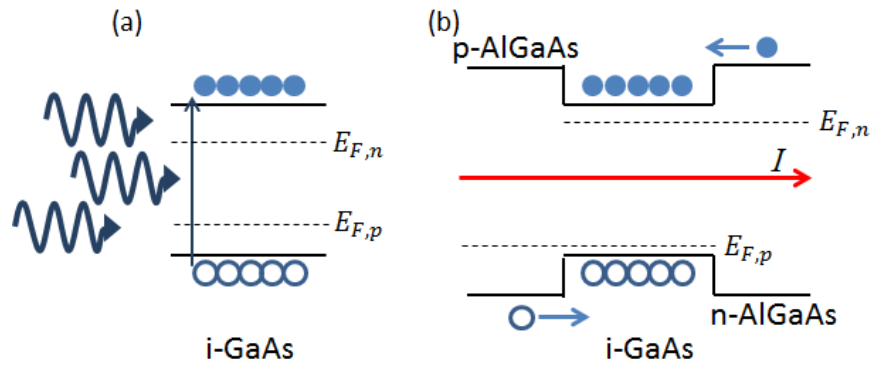


Figure 2.2 Schematic diagrams of (a) optical pumping and (b) electrical pumping.

So far we've only discussed about equilibrium carrier concentrations. It is also possible to create non-equilibrium carriers into semiconductors. This process is referred to as pumping. There are two general kinds of pumping: optical and electrical. Shown in Fig. 2.2 (a) is a schematic diagram of optical pumping. When photons with energy greater than the energy gap hit a semiconductor, photons are absorbed creating an electron-hole pair. Electrons in the VB are excited to the CB leaving a hole in the VB. Excited electrons naturally relax and recombine with holes in the VB after some time. This relaxation process has a characteristic recombination lifetime τ_{rec} . As long as the pumping continues, at the CB, there will be a non-equilibrium electron concentration $\Delta n = n - n_0$, where n_0 is the electron concentration at equilibrium. Likewise, in the VB, there will be a non-equilibrium hole concentration $\Delta p = p - p_0$. Again the subscript 0 indicates an equilibrium value. Note that owing to charge neutrality, Δn is always equal to Δp . The net effect is that the Fermi level is split into distinct quasi-Fermi levels: $E_{F,n}$ for electrons and $E_{F,p}$ for holes.

Pumping can also be achieved electrically. In this case, a p-type/intrinsic/n-type (p-i-n) junction is required. Shown in Fig. 2.2 (b) is a schematic diagram of electrical pumping. When a forward bias is applied to the p-i-n junction, a current passes through. In particular, electrons from the n-type material are injected into the intrinsic material. Likewise, holes

from the p-type material are injected into the intrinsic material. Note that the current has to be continuous anywhere in the junction so that overall charge neutrality is kept. This means again that, in the i-GaAs, $\Delta n = \Delta p$. Furthermore, at a high enough bias, the quasi-Fermi levels in the i-GaAs form, such that $E_{F,n}$ is continuous and matches the Fermi level of the n-type material and $E_{F,p}$ is also continuous and matches the Fermi level of the p-type material.

2.3 Semiconductor physics in Schottky photodiodes

We now move the discussion to the physics of photodiodes. Emphasis will be placed on Schottky photodiodes,¹³⁻¹⁷ since the structure of the spin-PDs in the present work are based on them. A Schottky photodiode (sometimes referred to as Schottky junction photodiode or Schottky barrier photodiode) is formed by a junction of a metal and a semiconductor (in the case of the spin-PDs here, we have inserted a thin insulating tunnel barrier between the metal and semiconductor, but the physics is the same). When a junction of a semiconductor with a metal is formed, a barrier along with a depletion region is formed in the semiconductor, as shown in Fig. 2.3. The height of the barrier ϕ_B and the width of the depletion region w depend of the properties of the metal and semiconductor.¹⁸

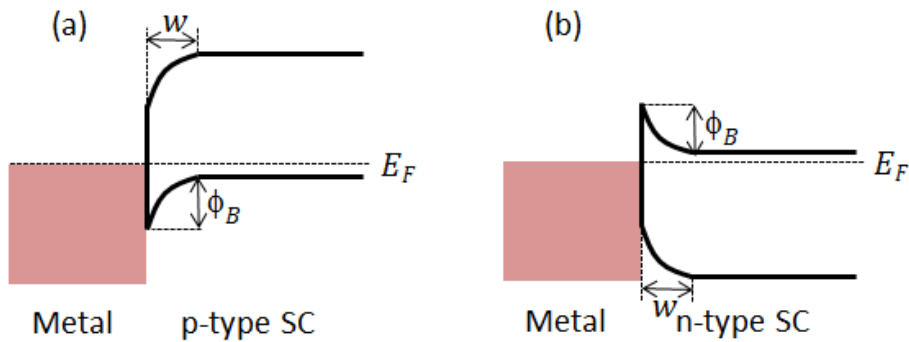


Figure 2.3 Energy band diagrams of (a) p-type and (b) n-type Schottky diodes.

In the first approximation, the barrier height is proportional to the difference between the work function of semiconductor and that of the metal. Inside the depletion region, (as the name suggests) carriers are depleted and there is a built-in electric field. This electric field can be utilized to collect photogenerated carriers. Schottky diodes can be constructed with a variety of metal and semiconductor combinations. If a p-type semiconductor is used [as shown in Fig. 2.3 (a)],¹⁹ the built-in electric field is directed away from the metal, and the barrier is formed at the VB. On the other hand, if an n-type semiconductor is used [as

shown in Fig. 2.3 (b)],²⁰ the built-in electric field is directed towards from the metal, and the barrier is formed at the CB. For the present work, p-type semiconductors have been used in order to collect electrons at the contact, so that we are going to focus on the p-type case.

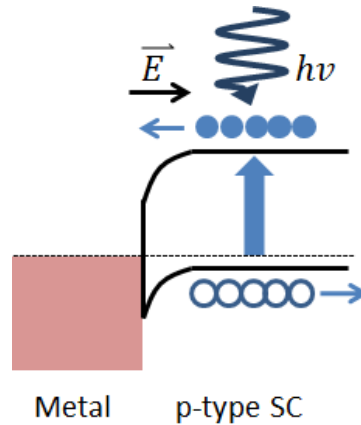


Figure 2.4 Working principle of p-type Schottky photodiode.

The working principle of a p-type Schottky photodiode is shown in Fig. 2.4. When light, with photon energy ($h\nu$) higher than the band gap (E_g) of the semiconductor ($h\nu > E_g$), is incident onto the semiconductor, carriers (electrons and holes) are photogenerated. The built-in electric field in the depletion region separates the electrons from the holes, with electrons being collected at the metal contact and holes being pushed into the bulk. At the metal contact, the collected minority carriers (electrons in this case) form the photocurrent. The principle of charge separation is an essential component in photodiode and solar cell operation. Furthermore, there are two components to the photocurrent: the drift component and the diffusion component. The drift component comes from electrons that are photogenerated inside the depletion width. These are immediately swept by electric field. On the other hand, the diffusion component comes from electrons that are photogenerated outside the depletion width but are transported via diffusion to the depletion region. Outside the depletion width, there is no electric field, but as more and more electrons pile up, a concentration gradient forms (with a low concentration near the depletion region and a high concentration at the bulk). Owing to the concentration gradient, electrons diffuse to the depletion region. The distance that electrons diffuse on average is described by the diffusion length λ_n . Electrons that are photogenerated within a distance λ_n from the depletion region have a high probability of being transported via diffusion and collected. On the other hand, electrons that are photogenerated at distances greater than λ_n from the depletion region have a small probability of being transported and collected. Therefore only electrons

photogenerated within λ_n contribute efficiently to the photocurrent. In a typical Schottky photodiode, the diffusion component tends to be larger than the drift component. This is because the Schottky depletion width is typically small, in the order of 10 to 100 nm,²¹ whereas the diffusion length is typically in the order of 1 to 10 μm .²²

2.4 Transport of carriers in a semiconductor

In the previous section, we have qualitatively discussed the concept of a Schottky photodiode. In order to quantitatively describe the carrier dynamics in the photodiode, we need to utilize the charge continuity equation.²³ This is also referred to as the drift-diffusion equation. The general form of the continuity equation is as follows:

$$\frac{\partial \Delta n}{\partial t} = D \nabla^2 \Delta n + \mu E \nabla \Delta n - \frac{\Delta n}{\tau_{rec}} + G. \quad (2.8)$$

Here, Δn is the non-equilibrium electron concentration at the CB, D is the diffusion coefficient, μ is the electron mobility, E is the electric field, τ_{rec} is the electron lifetime, and G is the generation rate. The term on the left side of the equation is the total change in Δn with respect to time, while on the right side of the equation, the first term is the diffusion term, the second is the drift term, the third is the recombination term, and the last is the generation term. The continuity equation is a differential equation which we can solve to find the dynamics of our electron system.

Let us consider the 1-dimensional (1-D) system shown in Fig. 2.4. In our photodiode, photons are incident to the semiconductor so that there is a non-zero G . For simplicity, let first only solve for the region outside the depletion region, where there is no electric field. Let us also assume that the illumination is uniform so that G is a constant. We are interested in finding the carrier distribution $\Delta n(x)$, where we let $x = 0$ be the boundary between the depletion region and the bulk of the semiconductor, so that we are solving for the region $x \geq 0$. We know that far from the depletion region (in the bulk, where $x \gg 0$), both the drift and diffusion terms in Eq. (2.8) vanish. If we were to look for the steady-state solution, we would get

$$0 = -\frac{\Delta n}{\tau_{rec}} + G. \quad (2.9)$$

Here, it becomes obvious that $\Delta n = G\tau_{rec}$. We've already found the value of Δn far from the depletion region. The only remaining problem is to solve for Δn closer to the depletion region, where the diffusion term is not zero. In this case, Eq. (2.8) becomes

$$0 = D \frac{\partial^2 \Delta n}{\partial x^2} - \frac{\Delta n}{\tau_{rec}} + G. \quad (2.10)$$

Here, we actually have the following boundary conditions: at $x \rightarrow \infty$, $\Delta n \rightarrow G\tau_{rec}$ and at $x = 0$, the charge and current have to be continuous, $J = D \cdot \frac{\partial \Delta n}{\partial x} = \mu E \Delta n(x = 0)$. The solutions to Eq. (2.10) are exponentials, and after imposing the boundary conditions the solution becomes

$$\Delta n(x) = G\tau_{rec}[1 - \exp(-x/\lambda_n)] + G\lambda_n/\mu E. \quad (2.11)$$

Here, $\lambda_n = \sqrt{D\tau_{rec}}$ is the electron diffusion length. It can also be shown that the current at $x = 0$ is

$$J(x = 0) = G\lambda_n. \quad (2.12)$$

This means that the diffusion component of the photocurrent is equal to number of photogenerated electron within λ_n . Now let us try to find the solution inside the depletion region. For simplicity, let us to shift coordinates to $x' = x + w$, so that $x' = 0$ is the interface between the metal and semiconductor. In this region, there is strong electric field so that we can ignore the diffusion and recombination terms. The continuity equation becomes

$$0 = \mu E \frac{\partial \Delta n(x')}{\partial x'} + G. \quad (2.13)$$

Here the following boundary conditions need to be imposed: at $x' = w$ or $x = 0$, both $J(x = 0) = G\lambda_n$ and $\Delta n(x = 0) = G\lambda_n/\mu E$ have to be continuous. It can be shown that the solution is

$$\Delta n(x') = (G/\mu E) \cdot (w - x') + G\lambda_n/\mu E. \quad (2.14)$$

And the current at $x' = 0$ is $J = \mu E \Delta n(x' = 0)$. Solving for this we get

$$J = G(w + \lambda_n). \quad (2.15)$$

This means that the total photocurrent is just equal to the total photogenerated electrons within $w + \lambda_n$. Since typically $w < \lambda_n$, it can be seen that the diffusion component of the photocurrent is larger than the drift component. Also, this again suggests that in electrons that are photogenerated far from the depletion region do not contribute efficiently to the photocurrent. Keeping this in mind is important in analyzing the spin-PDs in the present work.

2.5 Spin dynamics in a semiconductor

In this section, we now introduce the concept of spin polarization in semiconductors. In a semiconductor, electrons in the CB can either be spin-up or spin-down. Normally, there would be no point in distinguishing between the two since they are almost always equal in numbers (i.e. $n^\uparrow = n^\downarrow$). The electrons in the CB are spin polarized when $n^\uparrow \neq n^\downarrow$. As briefly mentioned in the preceding chapter, for a conventional (non-magnetic) semiconductor at

equilibrium, carriers are not spin-polarized.²⁴ Therefore, when any spin polarization present the system is not at equilibrium. The carrier spin polarization is usually defines as

$$P_n = \frac{\Delta n^\uparrow - \Delta n^\downarrow}{\Delta n^\uparrow + \Delta n^\downarrow} = \frac{\Delta s}{\Delta n}. \quad (2.13)$$

Here, Δn^\uparrow and Δn^\downarrow are the non-equilibrium carrier concentration for the spin-up and spin-down bands, respectively, Δs is the concentration of spins, and Δn is the total non-equilibrium carrier concentration. Shown in Fig 2.5 is the band diagram of intrinsic semiconductor with spin-polarization. Since $\Delta n^\uparrow \neq \Delta n^\downarrow$, the quasi-Fermi level for spin-up electrons $E_{F,n}^\uparrow$ is also not equal to the quasi-Fermi level for spin-down electrons $E_{F,n}^\downarrow$. Moreover, the difference $E_{F,n}^\uparrow - E_{F,n}^\downarrow$ is called the spin-splitting energy $\Delta\mu$.

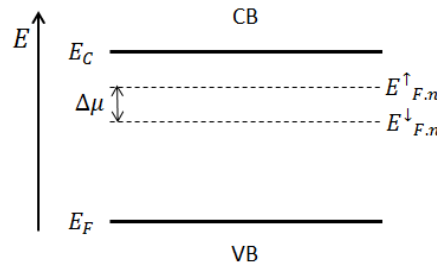


Figure 2.5 Energy band diagram of an intrinsic semiconductor with spin-polarized carriers.

Spin polarization in conventional semiconductor eventually vanishes as the system restores equilibrium in a process called spin relaxation. There are several mechanisms of spin relaxation semiconductors. For instance, in p-GaAs, the dominant spin relaxation mechanism is the Dyakonov-Perel (DP) mechanism.²⁵ Regardless of the mechanism, the net result is the same; electrons in the majority spin-band undergo spin flipping and get converted into electrons of the minority spin-band. This process is repeated until the two spin-bands have the same number of electrons. The time scale for this relaxation process is described by the characteristic spin lifetime τ_s . The spin lifetime τ_s is typically much faster than the carrier lifetime τ_{rec} .²²

In general, holes in the VB can also be spin-polarized, but in most cases, due to degeneracy of the light hole and heavy hole bands, the spin relaxation time of holes (in the order of 100 fs) is much faster than that of electrons.²⁶ So the spin polarization in holes practically vanishes immediately, so that for the rest of the analyses here, we will ignore hole spin polarization.

2.6 Optical spin injection into semiconductors

In the previous section, we have described the spin dynamics in a semiconductor without specifically talking about how spin polarization is introduced. The process of introducing spins is called spin injection. The simplest way of introducing spin polarized carriers into zincblende and diamond structure semiconductors is through optical spin injection. Shown in Fig. 2.6 is the spin optical selection rules (also referred to as the angular momentum conservation rules) for a bulk zincblende (e.g. GaAs) and diamond (e.g. Ge) crystal semiconductors.²⁷

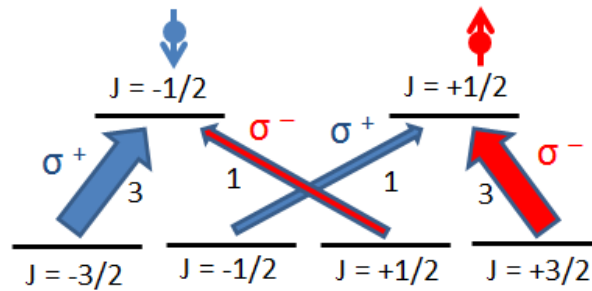


Figure 2.6 Spin optical selection rules for zincblende and diamond structure semiconductors.

Here, J is the angular momentum quantum number: $J = \pm 1/2$ for electrons in the CB, $J = \pm 3/2$ for heavy holes, and $J = \pm 1/2$ for light holes in the VB. The + sign is taken for spin-up, while the - sign is taken for spin-down. Since the charge of the electron is negative, the magnetic moment μ_j is directed down (up) for spin-up (spin-down) electrons. Furthermore, the transition probability for the heavy hole bands is 3 times that for the light hole bands. So that when σ^+ light is incident, the number of spin-up electrons photogenerated per unit time is 3 times that of spin-down electrons (i.e. $G^\uparrow = 3 \cdot G^\downarrow$). This leads to a spin generation rate of $G_S = G^\uparrow - G^\downarrow = 0.5 \cdot (G^\uparrow + G^\downarrow)$.

Optical spin injection is one of the earliest experimentally demonstrated methods of introducing spin into semiconductors.^{28,29} But due to the need for an external CPL source, practical applications have been scarce. Although recently, it has again become quite popular, thanks to the development of advanced vertical external cavity surface emitting lasers (VECSELs).^{1,30}

In the present study, the optical selection rules have been exploited to generate spin-polarized carriers in a Schottky photodiode. The photodiode then naturally collects these spin-polarized carriers as photocurrent. In this case, a special contact is actually needed

in order to convert the collected spins into an actual current, but these will be discussed in the latter sections.

2.7 Electrical spin injection into semiconductors

Electrically injecting spin into semiconductors effectively is one of the most active research topics in semiconductor spintronics today. It is not possible to directly inject spins, so the standard approach is to indirectly inject spins by using charge currents from a spin source such as a ferromagnetic metal. The idea is rather simple but actual implementation is difficult and complicated. Any good discussion in electric spin injection starts by talking about the conductivity mismatch problem (also referred to as the conductance mismatch problem).³¹ While the conductivity mismatch problem was originally formulated through rigorous theoretical calculations, here we will follow the more empirical argument presented in Ref. 32. (On an interesting side note, the first author of Ref. 31 also wrote Ref. 32.)

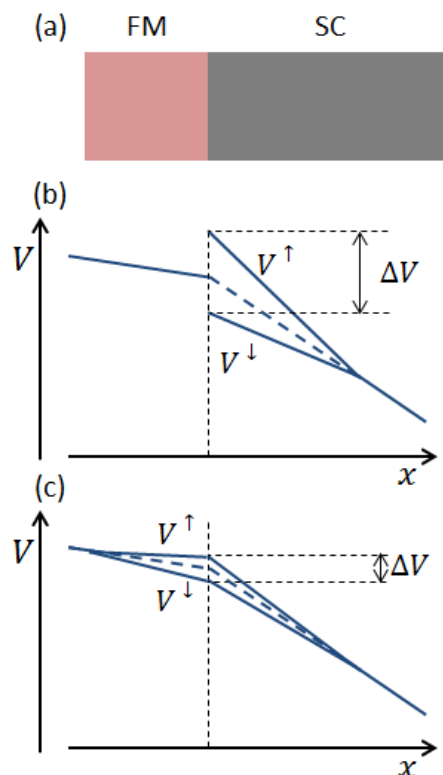


Figure 2.7 (a) Schematic of a FM-SC junction. (b) Voltage profile for the junction assuming the bulk FM polarization is fully injected across. (c) Voltage profile for the junction assuming the spin splitting voltage is continuous across the junction.

The problem formulation starts as follows: we want to inject spins from a ferromagnetic metal (FM) into a semiconductor (SC). So, we form a FM-SC junction as shown in Fig. 2.7

(a), in which the FM acts as an ohmic contact to the SC. We then drive a current across the junction. For simplicity, let us assume that the dimensions of the FM and SC are much larger than the spin diffusion lengths λ_s (all the spin dynamics are contained inside the FM-SC system). Typically, in a FM, $\lambda_{s,FM}$ is in the order of 10 nm, whereas in a SC, $\lambda_{s,SC}$ is in the order of 1 μm .³²

The basic idea is simple. Conduction electrons in a FM are spin-polarized at equilibrium. This is because there is an imbalance the densities of states D of the two spin bands as shown in Fig. 2.8. This is in contrast with that of a SC, where there is no spin polarization at equilibrium and that any spin-polarization is non-equilibrium. At the CB of the FM, the density of conducting electrons for each spin band is given by $N^{\uparrow(\downarrow)} = f(E_F) \cdot D^{\uparrow(\downarrow)}$, where $f(E_F)$ is the Fermi-Dirac distribution function and $D^{\uparrow(\downarrow)}$ is the effective density of states at the fermi level for the spin-up (spin-down) band. From the Drude model,³³ the current density in the FM is given by $J = \sigma_{drude} \cdot E = \left(\frac{Ne^2\tau^*}{m^*}\right) \cdot E$, where σ_{drude} is the Drude conductivity, E is the applied electric field, N the total density of conducting electrons, e the electron charge, τ^* the scattering time, and m^* the (effective) mass of the electrons. Now, we don't really care so much about the validity of the Drude model, only as much as that we can intuitively express the current density for each spin band as follows:

$$J = \left[\frac{(N^{\uparrow}+N^{\downarrow})e^2\tau^*}{m^*}\right] \cdot E = \left[\left(\frac{N^{\uparrow}e^2\tau^*}{m^*}\right) + \left(\frac{N^{\downarrow}e^2\tau^*}{m^*}\right)\right] \cdot E = (\sigma^{\uparrow} + \sigma^{\downarrow}) \cdot E = J^{\uparrow} + J^{\downarrow}. \quad (2.14)$$

Here, $\sigma^{\uparrow(\downarrow)}$ is the conductivity for the spin-up (spin-down) electrons and $J^{\uparrow(\downarrow)}$ is the spin-up (spin-down) component of the current density. The important point is that we have shown that $J^{\uparrow(\downarrow)} \propto \sigma^{\uparrow(\downarrow)} \propto D^{\uparrow(\downarrow)}$. That is when we drive a current through a FM the current is automatically spin-polarized due to the difference in density of states for the two spin bands.

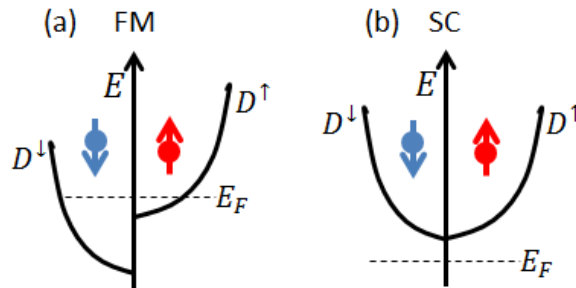


Figure 2.8 Schematic diagrams of densities of states for the two spin bands in the case of (a) a FM and (b) a SC.

It is also important to note that there are actually two spin-polarizations here. One is the

spin-polarization of the current $P_J = \frac{J^\uparrow - J^\downarrow}{J^\uparrow + J^\downarrow} = \frac{J_S}{J}$, where J_S is the spin current density, and the other being the spin-polarization of the electrons (carriers) $P_n = \frac{N^\uparrow - N^\downarrow}{N^\uparrow + N^\downarrow}$, which is also sometimes referred to as the bulk spin polarization β . If we only consider an isolated FM, these two are the same, but in general they can have different values. This is especially true when we deal with junction between FM and other materials.

Now, going back to the original problem, suppose we assume that, upon driving a current J across the FM-SC junction, the current spin-polarization $P_{J,FM}$ is the same as $P_{n,FM}$ in the FM, and that the $P_{J,FM}$ from the FM is conserved across the junction, so that at the SC just next to the junction $P_{J,SC} = P_{J,FM}$. Of course, inside the SC spin relaxation occurs, and at distances much larger than λ_s the spin-polarization vanishes. Shown in Fig 2.7 (b) is a diagram of what the voltage profile would look like in this case. To provide some context on the P_n value of a typical FM, Fe for example has a P_n of about 0.42.³⁴⁻³⁶ In order to create a $P_{J,SC}$ of 0.42 at the SC just next to the junction, there would have to be a large spin-splitting voltage $\Delta V_{SC} = \Delta\mu/e = (\mu^\uparrow - \mu^\downarrow)/e$. But this situation results in a discontinuity in the voltage profile of each spin band at the junction. Discontinuities in the voltages lead to near infinite voltage gradients and hence near infinite currents at the junction, a situation that is not possible. Hence, the voltage for each spin band should be continuous across the junction, so that a schematic the correct voltage profile is shown in Fig. 2.7 (c). At the far left of the junction, the spin-polarization of the current is $P_{J,FM} = P_{n,FM}$, but as we approach junction, the voltages of the two spin bands starts to split. At this region, the spin-polarization of the current is reduced ($P_{J,FM} \neq P_{n,FM}$), and is converted into a spin-voltage ΔV_{FM} . The spin-voltage at the left side of the junction is equal to the spin-splitting at the right side of the junction, $\Delta V_{FM} = \Delta V_{SC}$. Note that due to the gradient of ΔV_{FM} , it can be seen that $P_{J,FM} < P_{n,FM}$. Furthermore, in the SC, the spin-polarization of the current $P_{J,SC}$ is always the same as the spin-polarization of the carriers $P_{n,SC}$ because the conductivities of the two spin bands are always equal.

So where exactly is the problem? From the spin-polarized equivalent of Ohm's law, the spin current density at the SC side is

$$J_S = \sigma_{SC} \cdot \Delta V_{SC} / (2 \cdot \lambda_{s,SC}). \quad (2.15)$$

At the FM side, the spin current has two contributions, one from bulk spin polarization $P_{n,FM}$, and one from the spin-voltage ΔV_{FM} . Hence,

$$J_S = P_{n,FM} \cdot J - \sigma_{FM} \cdot \Delta V_{FM} / (2 \cdot \lambda_{s,FM}). \quad (2.16)$$

Here, the first term is just the bulk spin-polarization. The second term is negative because the direction of the gradient of ΔV_{FM} creates a spin current that is opposite that of the bulk, reducing the net spin current. Combining the expressions for the spin current for the two sides of the junction, it can finally be shown that

$$J_s = \frac{P_{n,FM} J}{\left(1 + \frac{\sigma_{FM} \lambda_{s,SC}}{\sigma_{SC} \lambda_{s,FM}}\right)}. \quad (2.17)$$

This (rather straightforward) expression tells us that value of the spin current J_s is simply proportional to the bulk spin polarization of the FM $P_{n,FM}$ multiplied with the total current being driven J , which makes sense. But notice also that spin current also depends on the terms in the denominator. Now let's try to run some numbers, σ_{FM} is about 10^7 S/m for Fe,³⁷ while σ_{SC} is about 10^3 S/m for highly doped GaAs.³⁸ Since we already have an idea for $\lambda_{s,SC}$ (about 1 μm) and $\lambda_{s,FM}$ (about 10 nm), it is clear that the denominator is of the order 10^6 , J_s is literally less than a millionth of the total current J . Hence, any attempt to electrically inject spins from a FM to a SC through an ohmic contact would results into a negligible spin current. The problem primarily arises from the difference in conductivities of the FM and SC. Metals tend to have high conductivities, while semiconductors (especially when not doped) tend to have very low conductivities.

Another point of interest here is that spin-voltage ΔV_{FM} at the FM can also be expressed as the product of the total current J and difference in the resistance (times area) of the spin-up and spin-down channels.

$$-\Delta V_{FM} = J \cdot (R^\uparrow - R^\downarrow) = J \cdot \left[\frac{2\lambda_{s,FM}}{\sigma_{FM}(1+P_{n,FM})} - \frac{2\lambda_{s,FM}}{\sigma_{FM}(1-P_{n,FM})} \right] = \frac{J \cdot 2\lambda_{s,FM}}{\sigma_{FM}} \cdot \left(\frac{-2P_{n,FM}}{1-P_{n,FM}^2} \right). \quad (2.18)$$

Here we only consider the region with the spin-voltage (within the distance $\lambda_{s,FM}$ from the junction). If we try to solve for the spin current J_s using Eq. (2.15), we get

$$J_s = \frac{\sigma_{SC} J (R^\uparrow - R^\downarrow)}{2 \cdot \lambda_{s,SC}} = \frac{\sigma_{SC} \lambda_{s,FM} J}{\sigma_{FM} \lambda_{s,SC}} \cdot \left(\frac{2P_{n,FM}}{1-P_{n,FM}^2} \right). \quad (2.19)$$

This expression essentially has the same message as Eq. (2.17). But what it does show more clearly is that in order to inject a J_s anywhere near J , the resistance difference $R^\uparrow - R^\downarrow$ (in units of $\Omega \cdot \text{cm}^2$) of the contact should be comparable to the resistance $\sigma_{SC}/(2\lambda_{s,SC})$ of the SC. In fact, the resistance difference $R^\uparrow - R^\downarrow$ is one of the most important figures of merit for a spin injector.³²

So, how do we solve this problem? Two solutions have been proposed. One is to use a dilute magnetic semiconductor (DMS) spin injector, and the other is to use a tunnel contact.³⁹⁻⁴¹ A typical DMS based spin contact such as GaMnAs has a conductivity of about

10^4 S/m, which is much closer to that of a SC. Shown in Fig. 2.9 (a) is the is a schematic of the voltage profile in a DMS-SC junction. There is a spontaneous spin polarization in the CB of a DMS, which is due to the actual splitting of the bottom edge of the CB for the two spin bands (much like a FM). This is in contrast with a SC, in which spin-polarization manifests a difference in the quasi-fermi level of the two spin bands. Unfortunately, so far DMS materials are only ferromagnetic at low temperatures (lower than 150 K for GaMnAs).⁴² This makes DMS spin contacts unsuited for room temperature operation, which only leaves the latter option for practical devices.

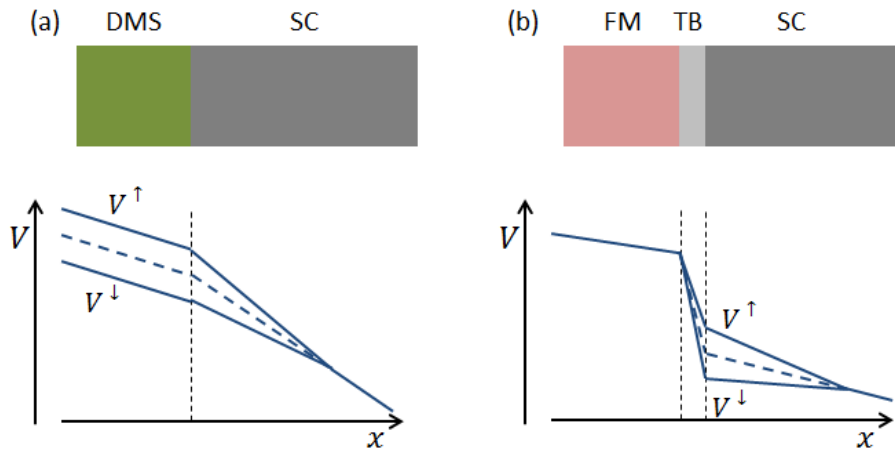


Figure 2.9 Voltage profiles for (a) a DMS-SC junction and (b) a FM-TB-SC junction.

The tunnel contact is by far the more popular choice, partially due to the successes in MTJ research. A tunnel contact is a junction formed by inserting a thin insulating tunnel barrier (TB) between a FM and a SC. Show in Fig. 2.9 (b) is a schematic of the voltage profile in a tunnel contact. There are two points of interest here: first, the resistance (times area) of the tunnel barrier is typically large (and usually dominates the total resistance) and can easily be controlled by choosing the thickness of the tunnel barrier; second, the difference in the resistances of the two spin channels is proportionally large. The latter point is essential for efficient spin injection.

Most discussions on spin injection stop at this point, but here we are going to go a step further. We are going to try to describe the properties of a tunnel contact. In a tunnel junction, the tunnel current for each spin band is described by^{43,44}

$$J^{\uparrow\downarrow} \approx T^{\uparrow\downarrow} \int D_1^{\uparrow\downarrow}(E) f_1(E - eV) D_2^{\uparrow\downarrow}(E) [1 - f_2(E)] dE. \quad (2.20)$$

Here, T is the tunneling probability (which depends on the barrier thickness), D_1 is the density of states in the left of the junction (in our case the FM), D_2 is the density of states in

the right of the junction (the SC), $f_{1,2}$ is the Fermi-Dirac distribution, E is just is the energy and eV is the electron charge times the applied voltage across the junction. The term inside the integral actually vanishes everywhere except around the CB edge of the SC E_C by virtue of the $f_{SC}(E - eV)D_{SC}(E)$ term. Also, the tunneling probability is usually the same for both spin bands, $T^\uparrow = T^\downarrow$. This is true for most tunnel barriers except for certain spinel oxides like MgO.⁴⁵ We can therefore express the tunnel current as

$$J^{\uparrow\downarrow} \approx T \cdot D_{SC}(E_C)^{\uparrow\downarrow} \cdot N_{FM}^{\uparrow\downarrow} \cdot eV. \quad (2.21)$$

Here, $D_{SC}(E_C)$ is the effective density of states at the CB edge of the SC, N_{FM} is the density conducting electrons in the FM. Note that we can express $N_{FM}^{\uparrow\downarrow}$ in terms of the total carrier density of conducting electrons N_{FM} and the polarization $P_{n,FM}$. Also, the density of states in a conventional SC is the same for both spin bands, $D_{SC}^\uparrow = D_{SC}^\downarrow$. Hence, the resistance (inverse of current) of each spin channel during tunneling is

$$R^{\uparrow\downarrow} \approx \frac{2 \cdot [T \cdot D_{SC} \cdot N_{FM} \cdot e]}{1 \pm P_{n,FM}} = \frac{2 \cdot R_{tunnel}}{1 \pm P_{n,FM}}. \quad (2.22)$$

Here, the term inside the square brackets is just the total tunnel resistance. We can finally combine this expression with Eqs. (2.15) and (2.18) to get the following:

$$J_s = \frac{\sigma_{SC} \cdot J \cdot (R^\uparrow - R^\downarrow)}{2 \cdot \lambda_{s,SC}} = J \cdot \left[\frac{\sigma_{SC} \cdot R_{tunnel}}{\lambda_{s,SC}} \cdot \left(\frac{2P_{n,FM}}{1 - P_{n,FM}^2} \right) \right]. \quad (2.23)$$

Here, we have derived a direct relation between the injected spin current J_s and total driven current J in tunnel contact. Note that J_s is always less than J , otherwise the spin splitting ΔV would be larger than the total applied voltage V , which is not possible. Therefore the term inside the square brackets is always less than 1.

Although electrical spin injection was not really experimentally carried out in the present study, the concept allows us to understand electrical spin detection, which is an essential component in the present study.

2.8 Electrical spin detection from semiconductors

As with electrical spin injection, there is no direct way of detecting or detecting spins in a semiconductor. The spin splitting itself of spin-polarized carriers in a semiconductor cannot be experimentally measured. It can, however, be converted into a voltage (or more accurately a change in the voltage) that can be measured using a tunnel.⁴⁶ Likewise, the spin current itself cannot be measured, but can be converted into an actual charge current (or change in the current) using a tunnel contact.

Let us first consider what actually happens during the tunneling process in an illuminated

spin-PD. Shown in Fig. 2.10 is a diagram of the density of states of the tunneling contact in a spin-PD during spin detection. Spin detection is essentially the reverse of spin injection. The equivalent of Eq. (2.20) in this case is

$$J^{\uparrow\downarrow} \approx T \int D_{SC}(E) D_{FM}^{\uparrow\downarrow}(E) f_{SC}(E - E_{F,n}^{\uparrow\downarrow}) [1 - f_{FM}(E)] dE. \quad (2.24)$$

Here, we assume that the tunneling probability T is the same for the two spin bands. In this case, the driving voltage is due to the photovoltaic effect, which is related to the quasi-Fermi levels in the SC, $V^{\uparrow\downarrow} = (E_{F,n}^{\uparrow\downarrow} - E_F)/e$. Compared to Eq. (2.20), where the energy in the FM was higher than the SC, here the energy at the SC is higher by virtue of the quasi-Fermi levels $E_{F,n}^{\uparrow\downarrow}$. Again, the term inside the integral vanishes everywhere due to the $f_{SC}(E - E_{F,n}^{\uparrow\downarrow}) D_{SC}(E)$ term, except at the vicinity of the CB edge E_C . Therefore, Eq. (2.24) can be written as

$$J^{\uparrow\downarrow} \approx T \cdot D_{FM}(E_C)^{\uparrow\downarrow} \cdot \Delta n^{\uparrow\downarrow}. \quad (2.25)$$

Here, $\Delta n^{\uparrow\downarrow} \approx \int D_{SC}(E) f_{FD}(E - E_{F,n}^{\uparrow\downarrow}) dE$ is simply the non-equilibrium carrier concentration in the SC for each spin band. The corresponding resistance for each spin-band is therefore

$$R^{\uparrow\downarrow} \approx \frac{R_{tunnel}}{D_{FM}^{\uparrow\downarrow} \cdot \Delta n^{\uparrow\downarrow}}. \quad (2.26)$$

Here, R_{tunnel} is some average tunnel resistance. Now, let us assume that the majority spin band for both the FM and SC is the spin-up band. Let us call this configuration the parallel (P) case, since the majority spin band on both sides of the tunnel barrier are parallel to each other. The equivalent tunnel resistance can be written as

$$R_P = \left(\frac{1}{R^{\uparrow}} + \frac{1}{R^{\downarrow}} \right)^{-1} = R_{tunnel} \left(\frac{1}{D_{maj} \Delta n_{maj}} + \frac{1}{D_{min} \Delta n_{min}} \right)^{-1}. \quad (2.27)$$

Here, R_P is the equivalent resistance for the parallel case, and the subscripts *maj* and *min* represent the majority and minority spin bands, respectively. Suppose now, we reverse the direction of the magnetization of the FM. (Likewise, we can also switch the helicity of the CPL illumination in the spin-PD). This time, the majority band in the FM is anti-parallel to the majority band in the SC. Let us call this the anti-parallel (AP) case. The equivalent tunnel resistance becomes

$$R_{AP} = R_{tunnel} \left(\frac{1}{D_{maj} \Delta n_{min}} + \frac{1}{D_{min} \Delta n_{maj}} \right)^{-1}. \quad (2.28)$$

Here, R_{AP} is the equivalent resistance for the anti-parallel case. What we are actually interested in is the tunnel magnetoresistance (TMR) ratio $/R$. It can be shown that the TMR ratio is

$$\frac{\Delta R}{R} = \frac{R_{AP} - R_P}{R_P} = \frac{2P_{FM}P_{SC}}{1 - P_{FM}P_{SC}}. \quad (2.29)$$

Here, P_{FM} is the spin polarization in the FM defined in terms of the density of states, and P_{SC} is the spin polarization in the SC defined in terms of the carrier densities.

$$P_{FM} = \frac{D_{maj} - D_{min}}{D_{maj} + D_{min}}. \quad (2.30)$$

$$P_{SC} = \frac{\Delta n_{maj} - \Delta n_{min}}{\Delta n_{maj} + \Delta n_{min}}. \quad (2.31)$$

We immediately recognize the similarity of Eqs. (2.29) to (2.30) to the Julliere model.⁴⁷ The Julliere TMR model is used to describe the tunneling between two ferromagnets. Here, we have derived an equivalent expression in the case of spin detection using a FM-based tunnel contact in a spin-PD (incidentally the form is similar to that of the Julliere model).

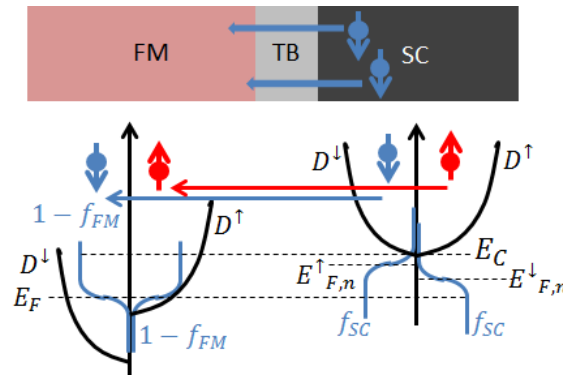


Figure 2.10 Schematic diagram of the density of states at the tunnel contact in a spin-PD.

Note that in the present study, since there is an electric field in the depletion region at the semiconductor side of the tunnel barrier (i.e. $J = \mu E \Delta n$), Eq. (2.31) can also be defined in terms of the currents:

$$P_{SC} = P_J = \frac{J_{maj} - J_{min}}{J_{maj} + J_{min}}.$$

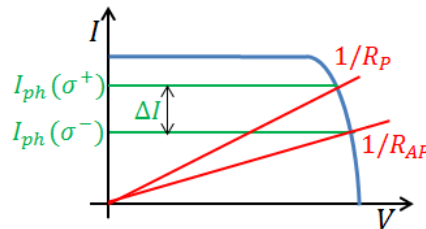


Figure 2.11 Power curve of a spin-PD plotted along the load line of the tunnel contact.

The photocurrent is the intersection of the power curve and load line.

Now that we have shown that by using a tunnel contact, the spin current manifests itself

through a change in resistance, we can easily calculate for the corresponding change in photocurrent using the load line model.³² An illuminated photodiode essentially acts like a power source. Shown in Fig. 2.11 is a schematic of the power curve of a spin-PD. The power curve is essentially the inverted I-V curve of the device (blue). Due to the high resistance of the tunnel contact, it effectively acts as a load to the spin-PD. A load in the power curve is represented as a straight line with a slope $1/R_{load}$ (red). The resulting current (photocurrent in this case) is the intersection between the power curve and the load line. In case of a spin-PD, the photocurrent is spin-polarized. In the parallel case, the equivalent load resistance would be smaller (higher slope of the load line). This leads the intersection to move to a higher current. Conversely, in the anti-parallel case, the equivalent load resistance would be bigger (lower slope of the load line). This leads the intersection to move to a lower current. The difference in the photocurrents for the parallel and anti-parallel case is therefore

$$\Delta I \approx \frac{V}{R^2} \Delta R = I_{ph} \frac{\Delta R}{R}. \quad (2.32)$$

Here, $R = (R_{AP} + R_P)/2$ is the average resistance. We have also assumed that the voltage remains approximately constant when we change the load resistance. Now we have finally derived an expression for the change in the photocurrent due to spin transport. Note that, since ΔI in Eq. (2.32) corresponds to the difference in the photocurrent between the parallel and anti-parallel cases, it is equivalent to the change in the photocurrent due to a helicity switching in the illuminated CPL. So that ΔI is also the helicity-dependent photocurrent.

As a final note, in Eq. (2.32) we assumed that the tunnel contact resistance dominates the total resistance. In the experiments in Ch. 5 and 6, however, an external load resistor is used to measure the photocurrent. In this case, the resistance of the external load has to be accounted for when computing for the spin-polarization.

This finally completes the theoretical description of the spin-PD.

References

- 1) S. S. Alharthi, J. Orchard, E. Clarke, I. D. Henning, and M. J. Adams, *Appl. Phys. Lett.* **107**, 151109 (2015).
- 2) C. Rinaldi, M. Cantoni, D. Petti, A. Sottocorno, M. Leone, N. Caffrey, S. Sanvito, and R. Bertacco, *Adv. Mater.* **24**, 3037 (2012).
- 3) A. Hirohata, Y. B. Xu, C. M. Guertler, J. A. C. Bland, S. N. Holmes, *Phys. Rev. B* **63**, 104425 (2001).
- 4) S. Hovel, N. C. Gerhardt, M. R. Hofmann, F.-Y. Lo, D. Reuter, A. D. Wieck, E. Schuster,

- W. Keune, H. Wende, O. Petravic, and K. Westerholt, *Appl. Phys. Lett.* **92**, 242102 (2008).
- 5) S. J. Steinmuller, C. M. Gurtler, G. Wastlbauer, and J. A. C. Bland, *Phys. Rev. B* **72**, 045301 (2005).
 - 6) S. M. Sze, *Physics of Semiconductor Devices* 2nd Ed. (John Wiley & Sons, New York 1981). Ch. 1, p. 14.
 - 7) S. M. Sze and M. K. Lee, *Semiconductor Devices Physics and Technology* (John Wiley & Sons Singapore, 2013), Ch. 1, pp. 26 – 29.
 - 8) W. Bludau, A. Onton, and W. Heinke, *J. Appl. Phys.* **45**, 1846 (1974).
 - 9) J. S. Blakemore, *J. Appl. Phys.* **53**, R123 (1982).
 - 10) P. J. Collings, *Am. J. Phys.* **48**, 197 (1980).
 - 11) V. Bougrov, M. E. Levinshtein, S. L. Rumyantsev, and A. Zubrilov, in *Properties of Advanced Semiconductor Materials GaN, AlN, InN, BN, SiC, SiGe* (John Wiley & Sons, New York 2001) eds. M. E. Levenshtein, S. L. Rumyantsev, and M. S. Shur, p. 1-30.
 - 12) S. M. Sze and M. K. Lee, *Semiconductor Devices Physics and Technology* (John Wiley & Sons Singapore, 2013), Ch. 1, pp. 29 – 40.
 - 13) K. W. Boer, *The Schottky Barrier Photodiode in Survey of Semiconductor Physics* (Springer Netherlands, 1992), Ch. 22, pp. 720 – 738.
 - 14) R. S. Quimby, *Photonics and Lasers An Introduction* (John Wiley & Sons, New Jersey), Ch. 14, p. 272 .
 - 15) B. G. Streetman, *Solid State Electronic Devices* (Prentice-Hall Englewood Cliffs, 1972), Ch. 6, pp. 232 – 237.
 - 16) S. M. Sze, *Physics of Semiconductor Devices* 2nd Ed. (John Wiley & Sons, New York 1981). Ch. 1, p. 749 – 763.
 - 17) S. M. Sze and M. K. Lee, *Semiconductor Devices Physics and Technology* (John Wiley & Sons Singapore, 2013), Ch. 10, pp. 333 – 334.
 - 18) R. Tung, *Appl. Phys. Rev.* **1**, 011304 (2014).
 - 19) M. Asif Khan, J. N. Kuznia, D. T. Olson, M. Blasingame, and A. R. Bhattarai, *Appl. Phys. Lett.* **63**, 2455 (1993).
 - 20) S. Y. Wang and D. M. Bloom, *Electron. Lett.* **19**, 554 (1983).
 - 21) M. K. Hudait and S. B. Krupanidhi, *Solid State Electron* **43**, 2135 (1999).
 - 22) I. Favorskiy, D. Vu, E. Peytavit, S. Arscott, D. Paget, and A. C. H. Rowe, *Rev. Sci. Instrum.* **81**, 103902 (2010).
 - 23) S. M. Sze and M. K. Lee, *Semiconductor Devices Physics and Technology* (John Wiley &

- Sons Singapore, 2013), Ch. 2, pp. 43 – 68.
- 24) M. I. Dyakonov, *Spin Physics in Semiconductors* (Springer-Verlag Berlin Heidelberg, 2008) Ch. 1, pp. 15 – 19.
 - 25) P. H. Song and K. W. Kim, Phys. Rev. B **66**, 035207 (2002).
 - 26) K. Shen and M. W. Wu, Phys. Rev. B **82**, 115205 (2010).
 - 27) M. I. Dyakonov, *Spin Physics in Semiconductors* (Springer-Verlag Berlin Heidelberg, 2008) Ch. 1, pp. 12 – 13.
 - 28) B. I. Zakharchenya, V. G. Fleisher, R. I. Dzhioev, Yu. P. Veshchunov, and I. B. Rusanov, J. Exp. Theor. Phys. Lett. **13**, 137 (1971).
 - 29) M. I. D'yakonov and V. I. Perel, J. Exp. Theor. Phys. **65**, 362 (1973).
 - 30) A. Joly, J. Frougier, G. Baili, M. Alouini, J. M. George, I. Sagnes, and D. Dolfi, Proc. SPIE **9755**, 9755E (2016).
 - 31) G. Schmidt, D. Ferrand, L. W. Molenkamp, A. T. Filip, and B. J. van Wees, Phys. Rev. B **62**, R4790(R) (2000).
 - 32) G. Schmidt, J. Phys. D: Appl. Phys. **38**, R107 (2005).
 - 33) D. J. Griffiths, *Introduction to Electrodynamics* (Prentice Hall, New Jersey 1999) Ch. 7, p. 289.
 - 34) R. J. Soulen Jr., J. M. Byers, M. S. Osofsky, B. Nadgorny, T. Ambrose, S. F. Cheng, P. R. Broussard, C. T. Tanaka, J. Nowak, J. S. Moodera, A. Barry, J. M. D. Coey, Science **282**, 85 (1998).
 - 35) M. B. Stearns, J. Magn. Magn. Mater. **5**, 167 (1977).
 - 36) T. Miyazaki and N. Tezuka, J. Magn. Magn. Mater. **139**, 231 (1995).
 - 37) R. A. Serway, *Principles of Physics* 2nd Ed. (Saunders College Pub., Fort Worth 1998), p. 602.
 - 38) M. Ohring, *Engineering Materials Science* (Academic Press Inc., San Diego 1995), Ch. 11, p. 561.
 - 39) E. I. Rashba, Phys. Rev. B **62**, R16267(R) (2000).
 - 40) D. L. Smith and R. N. Silver, Phys. Rev. B **64**, 045323 (2001).
 - 41) A. Fert and H. Jaffres, Phys. Rev. B **64**, 184420 (2001).
 - 42) F. Matsukura and H. Ohno, *III-V Based Ferromagnetic Semiconductors in Nanomagnetism and Spintronics* 2nd Ed. (Elsevier, London 2014) eds. T. Shinjo, p. 321.
 - 43) D. R. Penn, Surf. Sci. **50**, 125 (1975).
 - 44) S. M. Sze and M. K. Lee, *Semiconductor Devices Physics and Technology* (John Wiley & Sons Singapore, 2013), Ch. 2, pp. 56 – 68.

- 45) J. Zhang, X. G. Zhang, and X. F. Han, *Appl. Phys. Lett.* **100**, 222401 (2012).
- 46) Y. Ji, A. Hoffmann, J. S. Jiang, J. E. Pearson, and S. D. Bader, *J. Phys. D: Appl. Phys.* **40**, 1280 (2007).
- 47) M. Julliere, *Phys. Lett. A* **54**, 225 (1975).

3. Experimental techniques

3.1 Molecular beam epitaxy

Molecular beam epitaxy (MBE) is one of the most widely used techniques in the epitaxial growth of semiconductor wafers.¹⁻⁵ All wafers used in the current study were grown using a Riber MBE system. Here, the spin-PD wafers are mostly composed of GaAs with a thin (insulating) capping layer of AlO_x. Wafers used in Ch. 6 also have InGaAs layers grown on the GaAs layers. All the wafers were capped with 1-nm crystalline γ -like AlO_x,⁶ which was used as the tunnel barrier for spin detection.

Shown in Fig 3.1 is a schematic diagram of an MBE chamber. The substrate (wafer) is mounted on a Mo block using In metal. The temperature of the substrate is controlled using a substrate heater. A pyrometer has been used to measure the surface temperature of the wafers. Source materials placed in effusion cells are evaporated forming molecular beams that are directed to the wafer. In the present study, only 5 effusion cells have been used: Ga, As, In, Be, and Al. The MBE system is also equipped with Sn cell, but this was not used. During growth, the chamber is kept at ultra-high vacuum at around 10^{-10} Torr. The MBE chamber is also equipped with a reflection high-energy electron diffraction (RHEED) system, which allows us to assess the crystal quality of the surface of the wafer.

All the wafers were grown on p-GaAs substrates. Before the growth of each wafer, the p-GaAs substrates were thermally cleaned at 600 °C for about 10 to 20 mins. The growth starts with a p-GaAs buffer layer, grown at 580 °C, of at least 250 nm. The GaAs growth rate

was maintained at 1 μm per hour. Other specific details about the wafers used in the study will be discussed in Ch. 5 and 6.

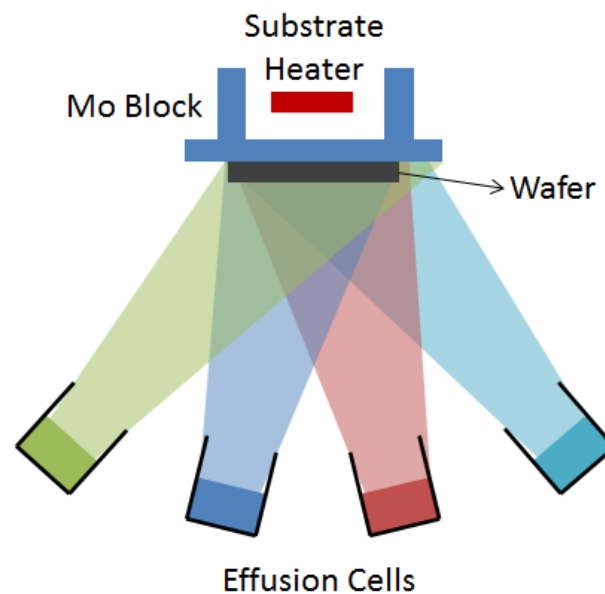


Figure 3.1 Schematic diagram of an MBE chamber during crystal growth.

After the growth of the semiconductor layers, an insulating AlO_x cap layer is also grown for each wafer. Details of the growth process have been reported in Ref. 6. The wafers are first cooled down to room temperature (at this point the thermocouple reading in the substrate heater usually reads 80 $^{\circ}\text{C}$). In addition, the As cell also has to be cooled to about 30 $^{\circ}\text{C}$ in order to lower the As pressure in the chamber. Once these conditions have been met, a 0.55 nm epitaxial Al layer (epi-Al) is grown on the wafers. This is referred to as the 1st epi-Al step. The wafers are then moved to loading chamber of the MBE system for oxidation. The oxidation is carried out by exposing the wafers with epi-Al to dry air at atmospheric pressure for at least 10 hours. This results in the formation of a 0.7-nm AlO_x film. This is referred to as the 1st oxidation step. The wafers are then moved back into the growth chamber and a 0.23 nm epi-Al is grown on top of the AlO_x . This is the 2nd epi-Al step. After this, the wafers are again moved back into the loading chamber for another 10 hours of dry air oxidation at atmospheric pressure. The final result is a 1-nm AlO_x layer. This layer has been used as the tunnel barrier for our tunnel contacts.

3.2 Device fabrication

Spin-PDs in Ch.5 require little device fabrication. Spin-PD chips are simply formed (after a single metallization step) by cleaving. On the other hand, spin-PDs in Ch. 6 require a

(relatively) more complicated fabrication. Hence, we are going to focus the discussion on the spin-PDs in Ch. 6.

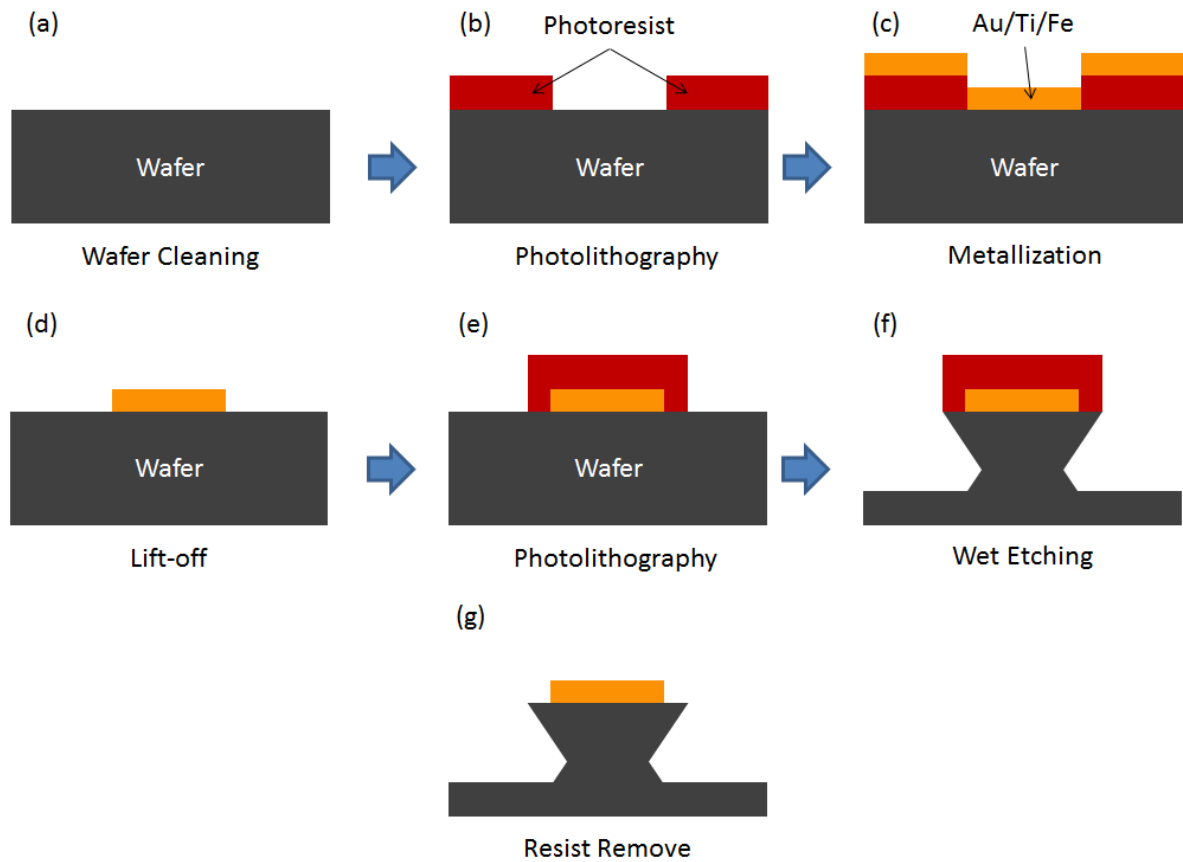


Figure 3.2 Schematic diagram of the device fabrication process for the spin-PD in Chapter 6.

Shown in Fig. 3.1 is the diagram of the fabrication process of the spin-PDs in Ch. 6. The MBE grown wafers are first cleaned using acetone and isopropyl alcohol [Fig. 3.1 (a)]. The 480- μm top contact is then fabricated using standard photolithography.^{7,8} Using a Nikon mask aligner, pattern from a 480- μm stripe photomask is transferred to a film of Microposit S1805 photoresist [Fig. 3.1 (b)]. Before exposure, the spin-coated photoresist film was pre-baked at 115 °C resulting in thickness of about 0.5 μm . The wafer with patterned photoresist was then placed inside a ULVAC for metallization (physical vapor deposition).^{9,10} A 100-nm Fe layer followed by a 10-nm Ti layer was deposited by e-beam deposition. A 20-nm Au layer was then deposited by resistive evaporation [Fig. 3.1 (c)]. Excess metal was then lifted-off by removing the photoresist [Fig. 3.1 (d)]. For back contact, a 40-nm In layer was deposited at the backside of the sample (not shown). The wafer was then annealed at 230 °C for 1 hour at ambient N_2 (also not shown).

In preparation for wet etching, a 520- μm photoresist stripe is patterned on top of the metal stripe [Fig. 3.1 (e)]. The photoresist stripe completely covered the metal stripe with a 20- μm margin in each side. Wet etching was used in order to fabricate the angled facet of the spin-PD. H_2SO_4 -based etchants are commonly used for GaAs device fabrication.¹¹⁻¹³ Here, a $\text{H}_2\text{SO}_4:\text{H}_2\text{O}_2:\text{H}_2\text{O}$ (1:8:1) etchant has been used.¹⁴ This etchant is known to form a unique undercut profile which is desired for our spin-PDs. During the wet etching, the beaker was gently stirred (shaken in a circular fashion) by hand. The direction of the stirring was reversed every minute to improve etching uniformity. The etching was carried out for a total of 30 minutes. Details of the fabricated device will be presented in Ch. 6.

3.3 Helicity-resolved photocurrent measurement

The main technique for characterization of spin-PDs is the helicity-resolved photocurrent measurement. A schematic of a typical setup used in the present study is shown in Fig. 3.3. A light beam from a light source (a laser in this case) is converted into CPL using a linear polarizer (LP) and a quarter-wave plate (QWP). After passing through the LP, the light becomes linearly polarized. The linearly polarized light, in turn, is converted into CPL after passing through the QWP. Furthermore, the helicity of the CPL can easily be switched by rotating the QWP (by 90°) by hand. Note that zero-order QWPs (such as the ones used here) have specific central wavelengths, so that care has to be taken in making sure that the QWP wavelength matches the wavelength of the light. Here, two distinct QWPs were used: a 800 nm QWP has been used for the experiment in Ch. 5, while a 900 nm QWP has been used for the experiments in Ch. 6.

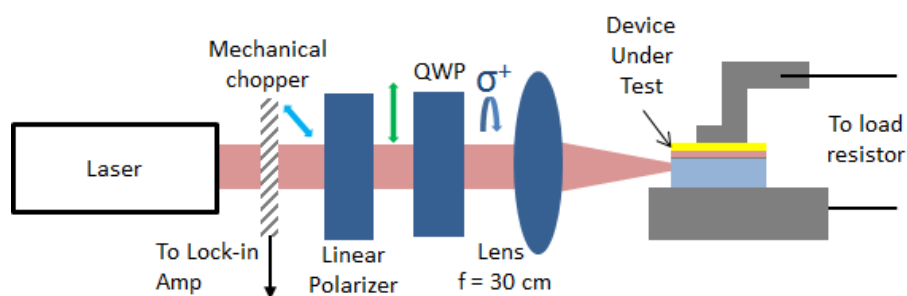


Figure 3.3 Schematic diagram of the helicity-resolved photocurrent measurement setup.

The CPL beam is then focused to the device under test (the spin-PDs) using a conventional lens. All measurements were carried out using lock-in technique by using a

mechanical chopper. Finally, the photocurrent was estimated by measuring the voltage drop across a load resistor connected in series with the spin-PD. The resistance of the load resistor was chosen to be equal to the total resistance of the spin-PD.

In particular, the voltage drop across the load resistor was measured using a lock-in amplifier. The two ends of the resistor were connected to the input port of the lock-in amplifier. The chopper signal was used as the lock-in reference. Since the incident light beam was modulated using the mechanical chopper, only the time-averaged illuminated voltage is measured (dark current from DC bias is taken out of the measurement). A more detailed explanation of the lock-in technique will be presented in the proceeding section. From the lock-in output voltage, the photocurrent was estimated using the following relation

$$I_{ph} = \frac{V_{ph}}{R_{total}} = \frac{V_{ph}}{R_{load} + R_{SPD}} = \frac{V_{ph}}{2R_{SPD}} = \frac{V_{load}}{R_{load}}. \quad (3.1)$$

Here, V_{ph} is the total voltage produced by the spin-PD via the photovoltaic effect, $R_{total} = R_{load} + R_{SPD}$ is the total resistance, which is the sum of the resistance of the spin-PD R_{SPD} and the resistance of the load resistor R_{load} , and V_{load} is the voltage drop across the load resistor whose value was taken from the lock-in output. From Eq. (3.1) it is straightforward to see that, if we let the resistance of the spin-PD to be $R_{SPD} \mp \Delta R/2$ for σ^\pm CPL illumination, the helicity-dependent photocurrent becomes

$$\Delta I = \frac{V_{ph}}{2R_{SPD} - \Delta R/2} - \frac{V_{ph}}{2R_{SPD} + \Delta R/2} \approx \frac{V}{R^2} \Delta R = I_{ph} \frac{\Delta R}{R}, \quad (3.2)$$

which is exactly the same as the expression in Eq. (2.32).

A typical measurement run sequence involves switching the helicity several times (for instance: $\sigma^+ \rightarrow \sigma^- \rightarrow \sigma^+ \rightarrow \sigma^- \rightarrow \sigma^+$). For each helicity, the photocurrent is measured for a time windows of more than 50 s. The average photocurrent value for each measurement window is recorded and is treated as one data point. The standard deviation for each window is also recorded and is treated as the error for that data point. Hence, in the example $\sigma^+ \rightarrow \sigma^- \rightarrow \sigma^+ \rightarrow \sigma^- \rightarrow \sigma^+$, there would be 3 data points for σ^+ photocurrent and 2 data points for σ^- photocurrent. The helicity-dependent photocurrent ΔI for the run is therefore calculated as the difference of the (3 point) average σ^+ photocurrent and (2 point) average σ^- photocurrent. The error in ΔI is estimated as the average error (of the 5 points). In addition, the average photocurrent I_{ph} for the run is calculated as the average of the averages of σ^+ and σ^- photocurrent (so that the difference in number of points for σ^+ and σ^- does not influence I_{ph}).

It can be seen that the number of data points for σ^+ (with 3 points) is more than that for σ^-

(with only 2 points). This was actually chosen by design to avoid the influence of long term drift in the measured photocurrent. In the example $\sigma^+ \rightarrow \sigma^- \rightarrow \sigma^+ \rightarrow \sigma^- \rightarrow \sigma^+$, notice how the order of the steps from the start to the half-way point of the sequence (i.e. $\sigma^+ \rightarrow \sigma^- \rightarrow \sigma^+$) is exactly the same as the steps from the half-way point to the end but in the reverse order (i.e. $\sigma^+ \leftarrow \sigma^- \leftarrow \sigma^+$). This is the characteristic of an odd run sequence. And one important property of an odd sequence is that long term drift can be averaged out. It can be seen that the first step (least affected by drift) is the same as the last step (most affected by drift). This combination of time averaging, error propagation, and run sequence engineering allows us to measure signals down to an accuracy of 0.2%, which would otherwise be too small to be observed directly. To give some context, lock-in amplification typically has an error of about 1%, the power output of a [optically pumped semiconductor (OPS)] laser can drift as much as 2%, while helicity-dependent photocurrent ΔI (which we are supposed to measure) can be as low as an order of 0.1% of the photocurrent.

3.4 Lock-in Technique

Lock-in amplification is a popular technique used in most optical and spectroscopic measurements.¹⁵ The technique involves the use of a reference signal (V_R) to amplify a weak input signal (V_{in}). The main technical requirement for lock-in amplification is that the input signal (the signal we want to amplify) needs to be modulated using some reference signal. In our case, we used a mechanical chopper to modulate the incident light at 400 Hz. We can therefore assume that the output photocurrent also carries some of the characteristics of the modulation. Note that there are other lock-in implementations and the input signal can be modulated using a variety of means.

Recall that in our setup, we have estimated the photocurrent by measuring the voltage drop across a load resistor. Let the voltage of the load resistor be our input signal V_{in} . We can assume that the photocurrent carries same modulation (frequency) characteristics as the chopper signal plus some noise (of different frequencies, uncorrelated with the chopper signal).

$$V_{in}(t) = V_0(t) + N(t). \quad (3.3)$$

Here, $V_0(t)$ is the voltage due to the photocurrent (what we actually want to measure), $N(t)$ is the noise signal. We know that $V_0(t)$ possesses the frequency characteristics of the chopper signal. The chopper signal is actually a square wave and can be expressed as

$$V_{CH}(t) = \frac{4}{\pi} \sum_{n=1,3,5,\dots}^{\infty} \frac{1}{n} \sin(n2\pi ft) \approx \frac{4}{\pi} \sin(2\pi ft). \quad (3.4)$$

Here, f is the chopping frequency (400 Hz in our case), and we have decomposed the chopper signal to its frequency components. The largest component is the first and lowest frequency (the fundamental) term of the series. For simplicity let us only consider this frequency (for now). Since $V_0(t)$ also possesses the same frequency characteristics, we can rewrite Eq. (3.3) as follows:

$$V_{in}(t) = V_0 \sin(2\pi f t + \varphi_{in}) + N(t). \quad (3.5)$$

Here, V_0 is just the amplitude of the input signal (a constant) and φ_{in} is the phase difference of the input signal with respect to the reference signal. The lock-in amplifier takes the input signal $V_{in}(t)$ and multiplies it by the reference signal $V_{CH}(t)$.

$$V_{CH}(t) \cdot V_{in}(t) = V_0 \frac{4}{\pi} \sin(2\pi f t) \sin(2\pi f t + \varphi_{in}) + \frac{4}{\pi} \sin(2\pi f t) N(t). \quad (3.6)$$

Here, we can simplify the first term as follows

$$\begin{aligned} V_0 \frac{4}{\pi} \sin(2\pi f t) \sin(2\pi f t + \varphi_{in}) &= \frac{1}{2} V_0 \frac{4}{\pi} \cos(2\pi f t - 2\pi f t - \varphi_{in}) \\ &\quad - \frac{1}{2} V_0 \frac{4}{\pi} \cos(2\pi f t + 2\pi f t + \varphi_{in}). \end{aligned} \quad (3.7)$$

Here, in the right-hand-side, the first term is actually a constant (DC) because of the $2\pi f t - 2\pi f t$ term, while the second term possesses twice the frequency. Using a low-pass filter, we can remove the second term and only get the first term. So that the final lock-in output can be expressed as

$$V_{out} = \frac{1}{2} V_0 \frac{4}{\pi} \cos(\varphi_{in}). \quad (3.8)$$

From here, it is clear that if the phase difference φ_{in} is known, the input voltage amplitude V_0 can easily be obtained. In an actual lock-in amplifier, φ_{in} is measured by adding a phase to the reference signal, φ_{ref} . By scanning φ_{ref} , a maximum V_{out} can be obtained when $\varphi_{ref} - \varphi_{in} = 0$. This way both V_0 and φ_{in} can be obtained unambiguously.

We note here that, had the input signal not possess the same frequency as the reference ($2\pi f_{in} t - 2\pi f_{CH} t \neq 0$), there would be no DC component and the low-pass filter would remove the entire signal. This has two important implications: (1) any part (or component) of the input signal that does not possess the same frequency as the reference signal is filtered out by the low-pass filter; and (2) if the reference signal has multiple component frequencies, the components of the input signal with the same frequencies would each be amplified. The first point clearly implies that the noise term in Eq. (3.6) would mostly be removed. The second point, on the other hand, implies that if the reference signal is say a square wave, the square wave components of the input signal would be amplified.

References

- 1) W. P. McCray, *Nat. Nanotechnol.* **2**, 259 (2007).
- 2) M. Shur, *GaAs Devices and Circuits* (Plenum Press New York, 1987), Ch. 3, pp. 116 – 120.
- 3) S. M. Sze and M. K. Lee, *Semiconductor Devices Physics and Technology* (John Wiley & Sons Singapore, 2013), Ch. 11, pp. 383 – 387.
- 4) I. A. Dorrity, J. D. Grange, and D. K. Wickenden, *Epitaxial Growth of GaAs in Gallium Arsenide Materials, Devices, and Circuits* eds. M. H. Howes and D. V. Morgan (John Wiley & Sons New York, 1985), Ch. 3, pp. 105 – 108.
- 5) S. Sakaki, *Molecular Beam Epitaxy in Materials Processing Theory and Practice* ed. R. J. Malik (North-Holland Amsterdam, 1989), Ch. 5, pp. 217 – 322.
- 6) N. Nishizawa and H. Munekata, *J. Appl. Phys.* **114**, 033507 (2013).
- 7) R. E. Williams, *Gallium Arsenide Processing Techniques* (ARTECH HOUSE Dedham, 1984), Ch. 6, pp. 125 – 143.
- 8) S. M. Sze and M. K. Lee, *Semiconductor Devices Physics and Technology* (John Wiley & Sons Singapore, 2013), Ch. 13, pp. 432 – 445.
- 9) C. J. Palmstrom and D. V. Morgan, *Metallizations for GaAs Devices and Circuits in Gallium Arsenide Materials, Devices, and Circuits* eds. M. H. Howes and D. V. Morgan (John Wiley & Sons New York, 1985), Ch. 6, pp. 195 – 262.
- 10) S. M. Sze and M. K. Lee, *Semiconductor Devices Physics and Technology* (John Wiley & Sons Singapore, 2013), Ch. 12, pp. 417 – 418.
- 11) S. M. Sze and M. K. Lee, *Semiconductor Devices Physics and Technology* (John Wiley & Sons Singapore, 2013), Ch. 13, pp. 451 – 454.
- 12) R. E. Williams, *Gallium Arsenide Processing Techniques* (ARTECH HOUSE Dedham, 1984), Ch. 4, pp. 101 – 122.
- 13) S. D. Mukherjee and D. Woodward, *Etching and Surface Preparation of GaAs for Device Fabrication in Gallium Arsenide Materials, Devices, and Circuits* eds. M. H. Howes and D. V. Morgan (John Wiley & Sons New York, 1985), Ch. 4, pp. 123 – 143.
- 14) D. Shaw, *J. Electrochem. Soc.: Solid State Sci. Technol.* **128**, 874 (1981)
- 15) J. H. Scofield, *Am. J. Phys.* **62**, 129 (1994).

4. Simulation of spin-photodiodes

4.1 General approach in simulation of spin-photodiodes

In terms of modeling and simulating spin-PDs, there is yet no consensus on a standard approach. Two recent works with proposed spin-PD models are Refs. 1 and 2. The former proposed a simple spin transport model in the semiconductor part of the spin PD by considering the transport geometry, but ultimately did not account for the spin dependent tunneling. Consequently, their approach resulted to a spin dependent tunnel current that appears to be independent of the magnetic property of the ferromagnetic tunnel contact. On the other hand, the latter proposed a more sophisticated (and complicated) theoretical model that considered both spin transport in the semiconductor part, as well as spin-dependent tunneling. Consequently, this resulted in a spin transport solution in the semiconductor that is strongly coupled with the tunneling transport, which leads to the following difficulties: (1) in order to determine the spin transport solution in the semiconductor, extensive information about the tunnel barrier and ferromagnetic contact is required; and (2) in the case of a different spin-PD geometry (such as those for the spin-PDs in the present work), the spin transport solutions become increasingly complex. In another earlier work,³ the spin-polarized carrier transport in a p-n spin-PD was modelled using drift-diffusion equations, but as with Ref. 1, the model failed to take into account how the spins will ultimately be transported through the contacts. This means that, so far, models tend to either too simplistic or excessively complicated.

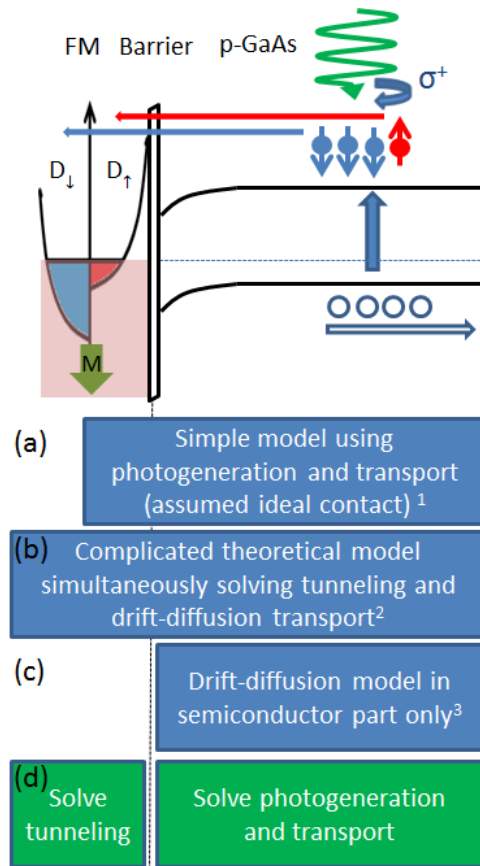


Figure 4.1 Diagram of a spin photodiode and a summary of proposed models. (a) A simple model using photogeneration and transport distance, but assumes an ideal contact. (b) An elaborate theoretical model that simultaneously solves the spin-polarized carrier transport and the tunneling effect. (c) A drift-diffusion model that only considers the transport inside the semiconductor (device contacts were not considered). (d) The proposed model in this work: a modular model that combines transport in the semiconductor and tunneling.

Shown in Fig. 4.1 is a schematic diagram of the relevant parts of a spin-PD, along with a summary of the scopes of proposed models so far. In the present work, we have taken the middle ground. Instead of tackling the problem in one go (simultaneously trying to solve for both the spin-transport in the semiconductor and the spin-dependent tunneling), we divide the problem into two independent parts: (1) we first evaluate the charge and spin transport in the semiconductor (similar to what Refs. 1 and 3 have proposed), either by using drift-diffusion equations or by considering the transport geometry; and (2) we evaluate the spin dependent tunneling by using a modified Julliere model (discussed in the last section of Ch. 2). Combined together, these lead to a modular version of the model proposed in Ref. 2, as shown in Fig. 4.1 (d). This treatment allows for the two parts to be independently

evaluated, which not only allows for greater flexibility but also leads to simpler overall calculations. Note that the first part of our approach can be further broken down into two components: (1) photogeneration of spin-polarized carriers, and (2) spin-polarized carrier transport. So that in all, the model involves 3 components.

In the present work, two approaches have been used in the calculation of the spin-polarized carrier transport. In Ch. 5, the drift-diffusion equations^{4,5} have been used to model the spin-polarized carrier transport. The main advantage of this approach is that, due to the sophistication of the model, additional conditions can easily be integrated into the model without affecting other parts of the model. The main disadvantage, however, is that in order to accurately describe a system, a very detailed knowledge of the boundary conditions is required. This is simple enough for some geometries but can be quite difficult for others. In Ch. 6, on the other hand, a simple mathematical model,¹ wherein only the photogeneration profile and the associated transport lengths are considered. The main advantage of this approach is the simplicity of the model that makes it much easier to implement than the drift-diffusion equations. It is also easy to show that (for certain geometries) the results of this approach are equivalent to those of the drift-diffusion equations. The main disadvantage, however, is the difficulty of introducing additional conditions. Additional conditions can still be introduced, but the model quickly becomes more and more complex as more conditions are introduced. These will be discussed in more detail in the proceeding sections.

4.2 Photogeneration of spin-polarized carriers

The process of optically introducing spins in a semiconductor by CPL illumination is referred to as optical spin injection⁶ or optical spin orientation,⁷ and is accomplished by photogenerating spin-polarized carriers in the semiconductor. There are two relevant generation rates:³ the photogeneration rate of carriers G (in units of number of carriers per unit volume per unit time) and the photogeneration rate of carriers of spins G_s (in units of number of spins per unit volume per unit time). These are described by

$$G = \eta \cdot \Phi \approx \alpha \cdot \Phi, \quad (4.1)$$

$$G_s = \eta_s \cdot \Phi \approx C \cdot P_c \cdot \alpha \cdot \Phi. \quad (4.2)$$

Here, η is the effective quantum efficiency¹ for carriers, η_s the effective quantum efficiency¹ for spins, α is the absorption coefficient in units of cm^{-1} , Φ is the photon flux, C is a constant that is determined by the optical selection rules (generally $|C| \leq 1$), and P_c is the degree of circular polarization [defined in Eq. (2.1)]. Furthermore, if we assume only band-to-band transitions (ignore other transitions such as free carrier absorption), then $\eta \approx \alpha$ (i.e. all absorbed photons generated an electron-hole pair).

In terms of individual spin bands, $\eta = \eta^\uparrow + \eta^\downarrow$ and $\eta_s = \eta^\uparrow - \eta^\downarrow$, where $\eta^{\uparrow(\downarrow)}$ is the effective quantum efficiency for the spin-up (spin-down) band. Hence, it follows that $G = G^\uparrow + G^\downarrow$ and $G_s = G^\uparrow - G^\downarrow$. In the usual convention, the total G for carriers is always the sum of those of the individual spin band (G^\uparrow and G^\downarrow), and the G_s for spins is always difference between those of the individual spin bands. Here, $G^{\uparrow(\downarrow)} = \eta^{\uparrow(\downarrow)} \cdot \Phi \approx \frac{[1 \pm C \cdot P_c]}{2} \cdot \alpha \cdot \Phi$, for which the + (-) is taken for \uparrow (\downarrow). Furthermore, we can also express $G^{\uparrow(\downarrow)}$ in terms of the σ^+ and σ^- components of Φ as follows

$$G^{\uparrow(\downarrow)} = \frac{[1 \pm C]}{2} \cdot \alpha \cdot \Phi^+ + \frac{[1 \mp C]}{2} \cdot \alpha \cdot \Phi^- \quad (4.3)$$

Here, the + (-) is taken for \uparrow (\downarrow) is taken for the first term, while - (+) is taken for \uparrow (\downarrow) for the second term. This means that when $C < 1$, $G^{\uparrow(\downarrow)}$ has contributions from both σ^+ and σ^- illumination. When $C = 1$, however, $G^{\uparrow(\downarrow)}$ only has contributions from $\sigma^{+(-)}$ illumination.

It is also worth noting that taking the ratio of Eq. (4.2) to Eq. (4.1) leads us to the following

$$P_G = G_s/G = C \cdot P_c \quad (4.4)$$

Here, P_G is the polarization of the generation rate, which is also the initial spin-polarization of photogenerated carriers. From Eq. (4.4) it can be seen that for optical spin injection, the highest possible initial spin-polarization photogenerated carriers is $P_G = 1$ (when $C = 1$). Therefore, it not possible to generate pure spins (spins without charges). In addition, the maximum value of P_G is limited by the value of C (since $|P_c| \leq 1$), and since in a spin-PD, photogenerated spin-polarized carriers are ultimately collected as photocurrent, the spin-polarization of the photocurrent P_j is also limited to the value of C . For the spin-PDs in the present study for instance, bulk GaAs and InGaAs have been used as the active layers, for which $C = 0.5$.^{8,9} So that $P_G = 0.5 \cdot P_c$. The means that the initial spin-polarization of photogenerated carriers is half the circular polarization of the incident light. Hence, the spin-polarization of the photocurrent is also limited to half the total photocurrent at best (i.e. $P_j \leq 0.5$). Note that all of these are consistent with the optical selection rules.¹⁰

As a final note, there are certain material systems where C takes on values other than 0.5. For example, for a quantum well (QW) or quantum dot (QD), owing to the splitting of the light hold and heavy hole energy bands due to confinement and possibly strain effects, $C = 1$,^{11,12} whereas for wurtzite GaN, owing to the weak spin-orbit splitting in the valence

band, $C = 0.33$.¹³ In theory, it is desirable to have a high C (to get a high P_G), so that a QW or QD system seem like the best choice, but in practice, the impact of spin-transport to the spin-PD performance tends to be larger than effect of C , and QW (and specially QD) active layers tend to be poor absorbers due to their small physical dimensions, hence are not well suited for spin-PDs.

4.3 Transport of charge and spins

After photogeneration, spin-polarized carriers are transported and collected at the tunnel contact. Therefore, we need a model that would describe the transport process. In the present study, two methods have been used: one is the drift-diffusion model,^{4,5} and the other is a model that simply considers the photogeneration profile and the transport distance¹ (the concept of this model closely resembles the so called collection probability in a solar cells).¹⁴⁻¹⁹ The former is the more traditional and well-known choice. It is flexible (additional boundary conditions can easily be added), but finding solutions can become difficult. On the other hand, the latter is the simpler and faster choice. It is straight-forward and very easy to implement. The downside is that it is not as flexible. Here, it will be demonstrated that both methods are essentially equivalent to each other. For this, we will consider two GaAs-based Schottky diode spin-PD systems: one is a vertical-type spin-PD [Fig. 4.2 (a)], and the other is a cleaved-edge lateral-type spin-PD [Fig. 4.2 (b)]. For simplicity, we chose the same structure for the two spin-PDs that involves a generic top tunnel contact and a p-GaAs active region. There is a Schottky depletion region at the top of the GaAs just below the tunnel contact with an electric field directed toward the z -direction (downward in Fig. 4.2). In addition, we assume that the intensity in the illuminated area is constant. The illuminated area for both cases is a circle with a diameter of 400 μm . Furthermore, inside the GaAs we assume that the light only propagates along the one direction: only along the z -direction for the vertical case and only along the x -direction for the lateral case. Strictly speaking the top contact for the vertical-type spin-PD should be magnetized out of the plane to work, whereas that of the lateral-type spin-PD should be magnetized in the plane. For now, we ignore these issues and focus on the spin-polarized transport in the semiconductor.

Let us start with the vertical-type spin-PD shown in Fig. 4.2 (a). Incident CPL hits the top ferromagnetic metal (FM) layer and is partially transmitted into the GaAs part of the spin-PD. Transmitted photon are then absorbed and spin-polarized carriers are photogenerated in the GaAs. The photon flux profile inside the GaAs is an exponential decay

and is described by

$$\Phi(z) = T \cdot \Phi_0 \cdot \exp(-\alpha z). \quad (4.5)$$

Here, Φ_0 is the initial photon flux (in units of number of photons per unit area per unit time), T is the transmittance of the top tunnel contact, and α is the absorption coefficient (just above the band gap, α is about 10^4 cm^{-1} for GaAs).²⁰ The main disadvantage of vertical-type spin-PDs is the rather low transmittance T of the top tunnel contact. For a 10-nm Fe contact, for example, T is about 10%.²¹

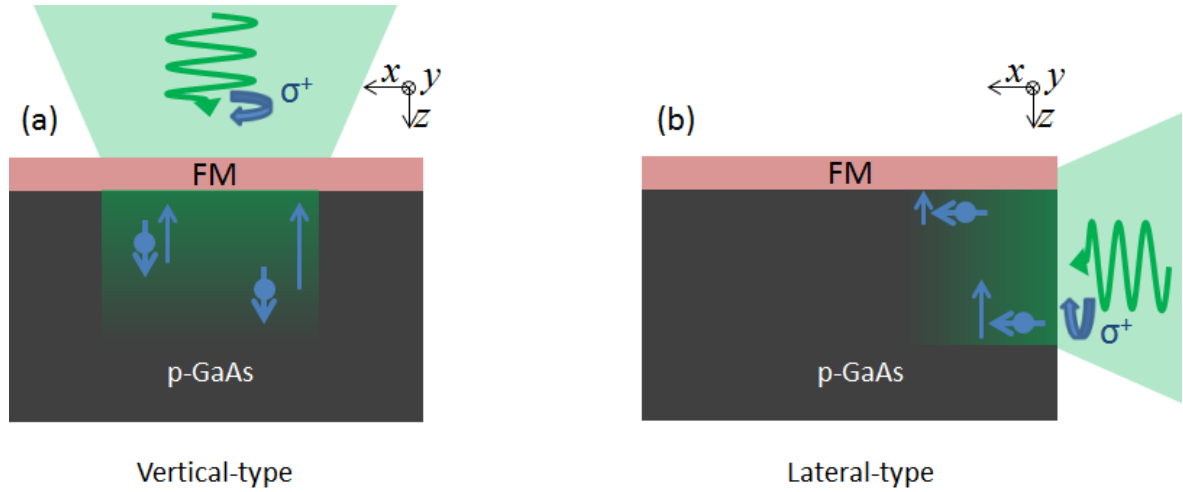


Figure 4.2 Schematic diagrams of (a) a vertical-type GaAs spin-PD and (b) a cleaved-edge lateral-type GaAs spin-PD.

Here, we take $z = 0$ as the top edge of the GaAs. We can then use Eqs. (4.1) and (4.2) to get the spatial profile of the photogeneration rates as follows:

$$G(z) = \alpha \cdot T \cdot \Phi_0 \cdot \exp(-\alpha z) = G_0 \exp(-\alpha z), \quad (4.6)$$

$$G_s(z) = 0.5 \cdot P_c \cdot \alpha \cdot T \cdot \Phi_0 \cdot \exp(-\alpha z) = G_{s,0} \exp(-\alpha z). \quad (4.7)$$

Here, we have gathered the constants into coefficients of the exponential profile, G_0 and $G_{s,0}$. Now, what we want to find out is how much photocurrent I_{ph} and spin-photocurrent I_s do we expect to collect at the top contact for a given Φ_0 . In addition, from here let us consider the case $P_c = 1$, which corresponds to σ^+ CPL.

Let us first try to use the drift-diffusion model. The drift-diffusion equation for charge and spins is described by the following:

$$\frac{\partial \Delta n}{\partial t} = D \nabla^2 \Delta n + \mu E \nabla \Delta n - \frac{\Delta n}{\tau_{rec}} + G(z), \quad (4.8)$$

$$\frac{\partial \Delta s}{\partial t} = D \nabla^2 \Delta s + \mu E \nabla \Delta s - \frac{\Delta s}{\tau_s} + G_s(z). \quad (4.9)$$

Here, Δn and Δs are the non-equilibrium electron and spin densities at the conduction band,

respectively, D is the diffusion coefficient, μ is the electron mobility, E is the electric field, τ_{rec} is the electron lifetime, and τ_s is the spin lifetime. The terms in the left side are the total change in Δn and Δs , while on the right side, the first terms account for diffusion, the second terms account for drift, the third terms account for lifetimes, and the last terms account for photogeneration. From the geometry [Fig. 4.2 (a)], it can be seen that the only relevant transport direction is along the z -axis. Sure, there is diffusion in the lateral directions (x - and y -directions) as well, but carriers that laterally diffuse also need to diffuse in the z -axis and be collected anyway. The net effect is that the area occupied by carriers would increase, but the total number of carriers would be the same as if there was no lateral diffusion. So, for simplicity we only consider a 1-dimensional (1-D) diffusion problem. Furthermore, since the depletion region has a width in the order of only 30 to 40 nm (compared to the diffusion length of about 21 μm), we can ignore the contribution of spin-polarized carriers that are photogenerated inside the depletion region. They typically contribute less than 1% of the total photocurrent (We can still include them later). This simplifies the problem further by allowing us to only solve for the region where there is no electric field (outside the depletion region). Instead, we account for the effect of the built-in electric field as the following boundary conditions at $z = 0$: $J = -e \cdot \partial \Delta n / \partial z = -e \cdot \mu E \cdot \Delta n(z = 0) / D$, and $J_s = -e \cdot \partial \Delta s / \partial z = -e \cdot \mu E \cdot \Delta s(z = 0) / D$. These conditions assure the continuity of the current density J and J_s as we cross the depletion region at $z = 0$. Thus, Eqs. (4.8) and (4.9) are transformed into the following:

$$0 = D \frac{\partial^2 \Delta n}{\partial z^2} - \frac{\Delta n}{\tau_{rec}} + G_0 \cdot \exp(-\alpha z), \quad (4.8)$$

$$0 = D \frac{\partial^2 \Delta s}{\partial z^2} - \frac{\Delta s}{\tau_s} + G_{s,0} \cdot \exp(-\alpha z). \quad (4.9)$$

Here, we are interested in the steady-state solutions so we have set the time derivative term to 0, and we have converted the Laplacian into a 1-D double partial derivative. We can solve Eqs. (4.8) and (4.9) numerically, but the analytical form of the solution is actually known.²²⁻²⁴ The solutions are

$$\Delta n(z) = \left(\frac{G_0 \tau_{rec}}{1 - \alpha^2 \lambda_n^2} \right) \left[\exp(-\alpha z) - \left(\frac{\alpha + \frac{\mu E}{D}}{\frac{1}{\lambda_n} + \frac{\mu E}{D}} \right) \exp(-z/\lambda_n) \right], \quad (4.10)$$

$$\Delta s(z) = \left(\frac{G_{s,0} \tau_s}{1 - \alpha^2 \lambda_s^2} \right) \left[\exp(-\alpha z) - \left(\frac{\alpha + \frac{\mu E}{D}}{\frac{1}{\lambda_s} + \frac{\mu E}{D}} \right) \exp(-z/\lambda_s) \right]. \quad (4.11)$$

Here, $\lambda_n = \sqrt{D \tau_{rec}}$ is the electron diffusion length, while $\lambda_s = \sqrt{D \tau_s}$ is the spin diffusion length. For p-GaAs, λ_n is about 21 μm , while λ_s is about 1.3 μm .²⁵ Shown in Fig. 4.3 are the Δn and Δs profiles for a typical p-GaAs spin-PD.

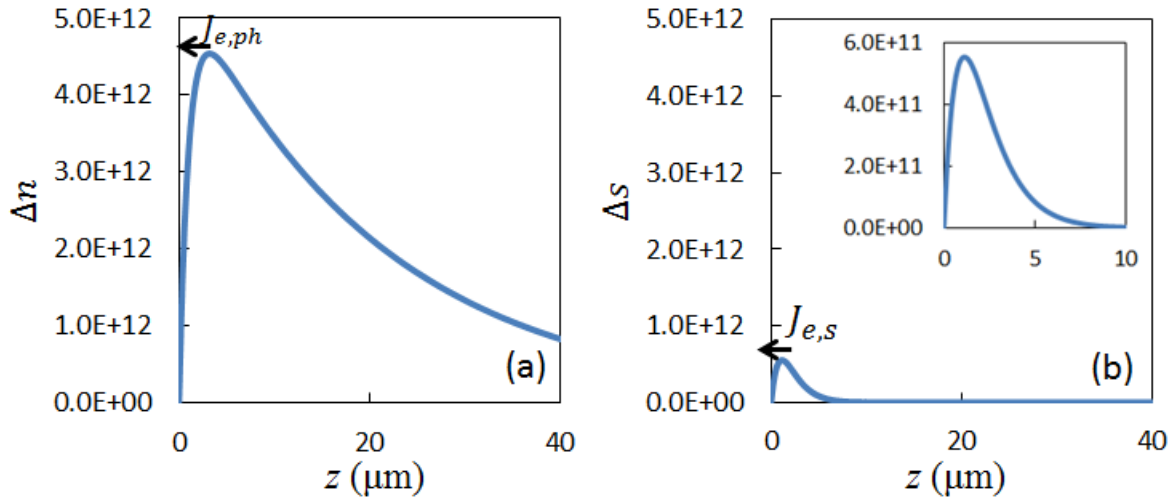


Figure 4.3 Profiles of (a) Δn and (b) Δs as functions of z . Inset of (b): rescaled (zoomed in) plot of Δs . Parameters used are $\Phi_0 = 3.4 \times 10^{19} \text{ cm}^{-2} \text{ s}^{-1}$, $A = 1.26 \times 10^{-3} \text{ cm}^2$, $D = 62 \text{ cm}^2/\text{s}$, $\alpha = 10^4 \text{ cm}^{-1}$,²⁰ $T = 0.1$,²¹ $E = 2.1 \times 10^5 \text{ V/cm}$, $\mu = 2400 \text{ cm}^2 \text{ V}^{-1} \text{ s}^{-1}$,²⁶ $\tau_{rec} = 7.15 \times 10^{-8} \text{ s}$,²⁵ $\tau_s = 2.33 \times 10^{-10} \text{ s}$.²⁷

From the slopes of the profiles, we can immediately guess the direction of the flow of charges $J_{e,ph}$ and spins $J_{e,s}$. Note that due to the negative charge of the electron, the actual photocurrent density $J = -e \cdot J_{e,ph}$ and spin-photocurrent density $J_s = -e \cdot J_{e,s}$ are directed opposite the flows. One of the main advantages of solving the drift-diffusion equations is that we are able to see the actual carrier and spin distributions. To compute for the total photocurrent I_{ph} and spin-photocurrent I_s , all we need to do is to evaluate the current densities J_{ph} and J_s at $z = 0$ and multiply the result by the illuminated area.

$$I_{ph} = A \cdot J = -e \cdot A \cdot D \cdot \left. \frac{\partial \Delta n}{\partial z} \right|_{z=0} = -e \cdot A \cdot D \cdot \left(\frac{G_0 \tau_{rec}}{1 - \alpha^2 \lambda_n^2} \right) \left[-\alpha + \left(\frac{\alpha + \frac{\mu E}{D}}{\frac{1}{\lambda_n} + \frac{\mu E}{D}} \right) \frac{1}{\lambda_n} \right], \quad (4.12)$$

$$I_s = A \cdot J_s = -e \cdot A \cdot D \cdot \left. \frac{\partial \Delta s}{\partial z} \right|_{z=0} = -e \cdot A \cdot D \cdot \left(\frac{G_{s,0} \tau_s}{1 - \alpha^2 \lambda_s^2} \right) \left[-\alpha + \left(\frac{\alpha + \frac{\mu E}{D}}{\frac{1}{\lambda_s} + \frac{\mu E}{D}} \right) \frac{1}{\lambda_s} \right]. \quad (4.13)$$

If J has a spatial dependence in the x - and y -directions (which would have been the case had we considered the effect of lateral diffusion), we would need to integrate J to get photocurrent, $I_{ph} = \int \int J(x, y, z = 0) \cdot dx \cdot dy$. Here we simply assume that J and J_s are uniform. Evaluating the currents, we get $I_{ph} \approx 0.66 \text{ mA}$ and $I_s \approx 0.17 \text{ mA}$. It is also useful to compute the spin polarization of the current $P_J = I_s / I_{ph}$. In this case, P_J is about $\approx 25\%$. We will see later that this value is actually high. Note that the P_J does not change with the incident power. In fact, P_J only depends on a couple of factors: first, the circular

polarization of the incident light (recall that here we assumed $P_c = 1$), and second, the geometry or configuration of the spin-PD (the illumination geometry as well as device configuration matters).

Now let us try to solve the same problem using the collection probability approach.¹⁴⁻¹⁹ Here, we use the same assumptions as before. We only consider the transport along the z -direction. We already know the photogeneration profiles from Eqs. (4.6) and (4.7). According to this approach, an electron that has been photogenerated at a given point z will be diffusively transported to $z = 0$, and the associated probability that the electron would make to $z = 0$ and be collected before recombining is $\exp(-z/\lambda_n)$.¹⁴ For instance, let us consider an electron that was photogenerated close to $z = 0$ (such that $z/\lambda_n \ll 1$), the collection probability would be close to 100%. If, on the other hand, we consider an electron what was photogenerated deep inside the GaAs (such that $z/\lambda_n \gg 1$), the collection probability would be almost 0. So that qualitatively, the collection probability $\exp(-z/\lambda_n)$ makes sense. For spins, the corresponding collection probability is $\exp(-z/\lambda_n) \cdot \exp(-z/\lambda_s)$, because spins not only suffer from recombination but also spin relaxation. The spin relaxation factor $\exp(-z/\lambda_s)$ dominates the collection probability for spins since λ_s is typically shorter than λ_n , so that we can ignore the $\exp(-z/\lambda_n)$.

Now, computing the photocurrent I_{ph} and spin-photocurrent I_s is straight forward. We know the number of electrons and spins being photogenerated at a point z is described by $G(z)$ and $G_s(z)$, so that amount of electrons and spins (being photogenerated at a point z) that would contribute to the I_{ph} and I_s has to be $G(z) \cdot \exp(-z/\lambda_n)$ and $G_s(z) \cdot \exp(-z/\lambda_s)$. To get the total, all we need to do is sum up all the contributions from different positions along the z -axis.

$$I_{ph} = A \cdot J = -eA \int_0^\infty G(z) \exp\left(-\frac{z}{\lambda_n}\right) dz = -eA \left(\frac{G_0 \lambda_n}{\alpha \lambda_n + 1}\right) = -eA \left\{ T \left[\frac{\alpha \lambda_n}{\alpha \lambda_n + 1} \right] \right\} \Phi_0, \quad (4.14)$$

$$I_s = A \cdot J_s = -eA \int_0^\infty G_s(z) \exp(-z/\lambda_s) dz = -eA \left(\frac{G_{s,0} \lambda_s}{\alpha \lambda_s + 1}\right). \quad (4.15)$$

We immediately see the simplicity of this approach. Note that authors of Ref. 1 went a step further by including a voltage dependent factor f to the collection probability (probably to fit their experiment results).¹ Here, we simple assume f is 1. Evaluating I_{ph} and I_s using the same parameters we used earlier, we get $I_{ph} \approx 0.65$ mA and $I_s \approx 0.19$ mA. The difference between these results from those we got from the drift-diffusion equation is in the order of 10%. This means that the predictions of the two methods are essentially the same.

By definition, the external quantum efficiency (EQE) is $\eta_{ext} = J/(e \cdot \Phi_0)$, and the

internal quantum efficiency (IQE) is $\eta_{int} = J/(T \cdot e \cdot \Phi_0)$. We immediately recognize that the quantity inside the curly brackets in Eq. (4.14) is the EQE, while the quantity inside the square brackets is the IQE. In this case, the EQE is about 9.5%, while the IQE is about 95%. From the IQE we can tell that the collection efficiency inside the GaAs is quite high. The low EQE tells us that the problem lies in getting the photon inside the active layer. In this case the low T of 10% significantly reduces the overall efficiency of the device.

By directly dividing Eq. (4.15) with Eq. (4.14), we can express the spin-polarization of the current as follows

$$P_j = \frac{I_s}{I_{ph}} = 0.5 \left[\frac{\lambda_s}{\lambda_n} \cdot \left(\frac{\alpha \lambda_n + 1}{\alpha \lambda_s + 1} \right) \right] = 0.5 \cdot \gamma. \quad (4.16)$$

Here, we can see that the factor 0.5 originally came from the optical selection rules, and the terms inside the square brackets can be gathered into a single term γ . In addition, it seems as though γ is some kind of efficiency. We started with light of circular polarization $P_c = 1$. Right after photogeneration the spin polarization was reduced by 0.5 owing to the selection rules. After transport, the spin polarization is further reduced by a factor γ . So that the spin-polarization of the photocurrent can be expressed as $P_j = 0.5 \cdot \gamma \cdot P_c$. In this case, P_j is about 0.3, so that γ is about 0.6. Since γ depends on the configuration or geometry of the spin-PD, I will just simply refer to it as the geometrical spin transport factor, spin collection efficiency, or spin-transport efficiency. This demonstrates the advantage of using the collection probability method. The method is not only simple, but it also allows us to intuitively recognize which parameters determine the performance of the spin-PD. Here for instance, the factors λ_s/λ_n and $\frac{\alpha \lambda_n + 1}{\alpha \lambda_s + 1}$ determine the value of γ . The former is fixed at 0.06 for p-GaAs, unfortunately. The latter, however, can be changed and γ can be improved by increasing α (through changing the wavelength).

Now let us move on to the lateral-type spin-PD [Fig. 4.2 (b)]. The spin-PD device structure is the same as before. This time the light is incident into the cleaved sidewall ($x = 0$) of the GaAs part of the spin-PD. The photon flux profile inside the GaAs is now described by:

$$\Phi(x) = T \cdot \Phi_0 \cdot \exp(-\alpha x). \quad (4.17)$$

Here, the exponential decay is along now along the x -axis, and T is the transmittance of the cleaved sidewall. The transmittance of a GaAs/air interface is about 0.7.²⁸ The corresponding generation rates are

$$G(x) = \alpha \cdot T \cdot \Phi_0 \cdot \exp(-\alpha x) = G_0 \exp(-\alpha x), \quad (4.18)$$

$$G_s(x) = 0.5 \cdot P_c \cdot \alpha \cdot T \cdot \Phi_0 \cdot \exp(-\alpha x) = G_{s,0} \exp(-\alpha x). \quad (4.19)$$

In order to simplify our problem further, let us first assume that the cleaved sidewall at $x = 0$ has been passivated, so that there is no surface recombination at $x = 0$. Strictly speaking, usually there are defects that act as recombination centers at the cleaved sidewall of GaAs.²⁹ For now let us ignore them (we will deal with them later). In addition, let us again ignore the lateral (y - and x -directions) diffusion. We can again argue that even though there is lateral diffusion, spin-polarized carriers that laterally diffuse also need to diffuse in the z -axis and be collected anyway. Lateral diffusion only changes the lateral area occupied by photogenerated carriers but the total number of carriers is the same as that if there was no lateral diffusion (We can include lateral diffusion but the results would be completely the same). Hence, the only relevant transport direction in determining the photocurrent is along the z -axis.

This time let us first solve the problem using the collection probability method. In this case the current densities J and J_s are described by

$$J = -e \int_0^{\infty} G(x) \cdot \exp(-z/\lambda_n) dz = -e \cdot G(x) \cdot \lambda_n, \quad (4.20)$$

$$J_s = -e \int_0^{\infty} G_s(x) \cdot \exp(-z/\lambda_s) dz = -e \cdot G_s(x) \cdot \lambda_s. \quad (4.21)$$

Here, the integration is still along the z -axis since the collection probability depends the distance along the z -direction. But G and G_s have no dependence on z . Hence, J and J_s have an x dependence, owing to x -dependence of $G(x)$ and $G_s(x)$. The total photocurrent I_{ph} and spin-photocurrent I_s are given by the following:

$$I_{ph} = \int \int J(x) dx \cdot dy = -e \cdot G_0 \cdot \frac{d\lambda_n}{\alpha} = -e \cdot G_0 \delta \cdot d \cdot \lambda_n, \quad (4.22)$$

$$I_s = \int \int J_s(x) dx \cdot dy = -e \cdot G_{s,0} \cdot \frac{d\lambda_s}{\alpha} = -e \cdot G_{s,0} \delta \cdot d \cdot \lambda_s. \quad (4.23)$$

Here, d is the width of the illuminated area in the y -axis ($d = \int dy$), and $\delta = 1/\alpha$ is the optical penetration depth. Here, we can make the following observations: it is as though the photogeneration rates G_0 and $G_{s,0}$ are uniformed spread across a depth δ in the x -direction. This makes sense because most of the optical intensity only penetrates up to δ , so that if we count the total (including photons that penetrate deeper than δ), we would indeed get $G_0 \delta$ and $G_{s,0} \delta$, respectively. Also, I_{ph} and I_s comes from the photogenerated carriers that are evenly spread across a width d in the y -direction, which again make perfect sense, since this is the width of the illuminated area. What is interesting here is that it seems as though I_{ph} and I_s comes from the photogenerated carriers that are evenly spread across heights λ_n and λ_s in the z -direction. This means that only carriers photogenerated within λ_n are collected efficiently. Likewise, only spins photogenerated within λ_s are collected efficiently.

Evaluating I_{ph} and I_s gives us 0.32 and 0.01 mA, respectively. It can be seen that even though the transmittance T of the sidewall is much higher than that of the top metal contacts, we still get a lower I_{ph} for the lateral-type spin-PD. This is because only the photons that enter the region within $\lambda_n = 21 \mu\text{m}$ from the top contact can contribute effectively to I_{ph} . Also, I_s is significantly lower compared to that of vertical-type spin-PD. Similarly, this is because only the photons that enter the region within $\lambda_s = 1.3 \mu\text{m}$ from the top contact can contribute effectively to I_{ph} . This goes to show how inefficient this kind of lateral spin-PD is.

The IQE in this case is about 10%, which is much lower compared to IQE of the vertical case. On the other hand, the EQE is about 7%. This time the EQE is comparable to the IQE because of the relatively high transmittance of the sidewall.

Computing for spin polarization of the photocurrent gives us the following

$$P_j = \frac{I_s}{I_{ph}} = 0.5 \left[\frac{\lambda_s}{\lambda_n} \right] = 0.5 \cdot \gamma. \quad (4.24)$$

Here, we have again gathered the terms inside the square bracket into γ . In this case, P_j is about 3.1% and γ is about 6%. Recall that the structure of this spin-PD is same as that of the earlier vertical spin-PD. We have only changed the illumination configuration, yet the resulting drop in γ is astounding.

For completeness, let us try to solve this lateral spin-PD case using the drift-diffusion equations. We start again with the steady-state diffusion equations

$$0 = D \frac{\partial^2 \Delta n}{\partial z^2} - \frac{\Delta n}{\tau_{rec}} + G_0 \cdot \exp(-\alpha x), \quad (4.25)$$

$$0 = D \frac{\partial^2 \Delta s}{\partial z^2} - \frac{\Delta s}{\tau_s} + G_{s,0} \cdot \exp(-\alpha x). \quad (4.26)$$

Here, we have again ignored the depletion region so that the drift term has been dropped. We again consider only transport along the z -axis, and the photogeneration term, now, is independent of z . The form of the analytical solutions for these is known.

$$\Delta n(z, x) = G_0 \tau_{rec} [1 - \exp(-z/\lambda_n)] \cdot \exp(-\alpha x), \quad (4.27)$$

$$\Delta s(z, x) = G_{s,0} \tau_s [1 - \exp(-z/\lambda_s)] \cdot \exp(-\alpha x). \quad (4.28)$$

Here, we have again ignored lateral diffusion and hence, the x -dependence of Δn and Δs comes from G and G_s , respectively. Solving for the current densities J and J_s at $z = 0$ yields

$$J = -e \cdot D \cdot \left. \frac{\partial \Delta n}{\partial z} \right|_{z=0} = -e \cdot \frac{DG_0 \tau_{rec}}{\lambda_n} = -e \cdot G_0 \cdot \lambda_n \cdot \exp(-\alpha x), \quad (4.29)$$

$$J_s = -e \cdot D \cdot \left. \frac{\partial \Delta s}{\partial z} \right|_{z=0} = -e \cdot \frac{DG_{s,0} \tau_s}{\lambda_s} = -e \cdot G_{s,0} \cdot \lambda_s \cdot \exp(-\alpha x). \quad (4.30)$$

Now, we know these are correct because these are exactly the same as Eqs. (4.20) and (4.21). Note that the way we solved Eqs. (4.29) and (4.30) is entirely different from how we solved Eqs. (4.20) and (4.21). Here we took the derivative of Δn and Δs utilizing the boundary condition at $z = 0$, whereas for Eqs. (4.20) and (4.21), we simply integrated the generation rates, yet we got the exact same results. This demonstrates that the two methods are essentially equivalent.

Up to now we have ignored the contribution of spin-polarized carriers that are photogenerated in the depletion region. We can simply include their contribution by making the following modification to Eqs. (4.22) and (4.23): $\lambda_n \rightarrow \lambda_n + w$ and $\lambda_s \rightarrow \lambda_s + w$.

$$I_{ph} = -e \cdot G_0 \delta \cdot d \cdot (\lambda_n + w), \quad (4.31)$$

$$I_s = -e \cdot G_{s,0} \delta \cdot d \cdot (\lambda_s + w). \quad (4.32)$$

Here, w is the width of the depletion region, which is about 40 nm. These modifications result in an increase of 0.2% and 3% to I_{ph} and I_s , respectively, compared to our previous calculations where we ignored the depletion width contribution. This shows that our approximation is justified.

Finally, let us consider what would happen if we also consider the surface recombination at $x = 0$ (recall that so far we have assumed that the cleaved sidewall is sufficiently passivated). In an actual cleaved sidewall, there are recombination centers such that carriers that are excited near the sidewall are driven towards the cleaved sidewall at a surface recombination velocity $S = 7.7 \times 10^7$ cm/s.²⁹ The effect of this to the spin-PD performance is significant. We can no longer ignore lateral diffusion along the x -axis, since the number of spin-polarized carriers is no longer the same as that if there was no lateral diffusion.

Let us start by using the drift-diffusion equations. Note that now, we cannot simplify the system into 1-D. We need to solve a 2-D diffusion problem (we can still ignore diffusion in the y -direction). One advantage of using the drift-diffusion equations is that we can simply include the effect of surface recombination as the following boundary conditions at $x = 0$: $J_{surf} = -e \cdot \partial \Delta n / \partial x = -e \cdot S \cdot \Delta n(x = 0) / D$, and $J_{s,surf} = -e \cdot \partial \Delta s / \partial x = -e \cdot S \cdot \Delta s(x = 0) / D$, where J_{surf} and $J_{s,surf}$ are the surface recombination current and the surface recombination spin-current, respectively. The diffusion equations become

$$0 = D \nabla^2 \Delta n - \frac{\Delta n}{\tau_{rec}} + G(x), \quad (4.33)$$

$$0 = D \nabla^2 \Delta s - \frac{\Delta s}{\tau_s} + G_s(x). \quad (4.34)$$

We can solve Eqs. (4.33) and (4.34) numerically, but here we will solve them analytically with a couple of approximations. We first assume separable solutions $\Delta n(x, z) \approx$

$\Delta n_x(x)\Delta n_z(z)$ and $\Delta s(x, z) \approx \Delta s_x(x)\Delta s_z(z)$. Note that Eqs. (4.33) and (4.34) are not actually separable, but with the help of a couple of approximations, we can still decouple the x and z dependencies. We first rewrite the equations as

$$-D \frac{\partial^2 \Delta n}{\partial z^2} = D \frac{\partial^2 \Delta n}{\partial x^2} - \frac{\Delta n}{\tau_{rec}} + G(x), \quad (4.35)$$

$$-D \frac{\partial^2 \Delta s}{\partial z^2} = D \frac{\partial^2 \Delta s}{\partial x^2} - \frac{\Delta s}{\tau_s} + G_s(x). \quad (4.36)$$

Here, we will first find the solution at the region $z \gg \lambda_n$. At this region (deep in the bulk of the GaAs), $\frac{\partial^2 \Delta n}{\partial z^2}$ and $\frac{\partial^2 \Delta s}{\partial z^2}$ become negligibly small. This is because the photon flux is uniform and this region is far from the depletion region where there is a built-in electric field, so that nothing would drive the diffusion in the z -direction. However, there is still a gradient in the x -direction, so that we can rewrite Eqs. (4.35) and (4.36) as

$$0 = D \frac{\partial^2 \Delta n_x}{\partial x^2} - \frac{\Delta n_x}{\tau_{rec}} + G(x), \quad (4.35)$$

$$0 = D \frac{\partial^2 \Delta s_x}{\partial x^2} - \frac{\Delta s_x}{\tau_s} + G_s(x). \quad (4.36)$$

The analytical form of the solutions to these equations is known.

$$\Delta n_x(z) = \left(\frac{G_0 \tau_{rec}}{1 - \alpha^2 \lambda_n^2} \right) \left[\exp(-\alpha x) - \left(\frac{\alpha + \frac{S}{D}}{\frac{1}{\lambda_n} + \frac{S}{D}} \right) \exp(-x/\lambda_n) \right], \quad (4.37)$$

$$\Delta s_x(z) = \left(\frac{G_{s,0} \tau_s}{1 - \alpha^2 \lambda_s^2} \right) \left[\exp(-\alpha x) - \left(\frac{\alpha + \frac{S}{D}}{\frac{1}{\lambda_s} + \frac{S}{D}} \right) \exp(-x/\lambda_s) \right]. \quad (4.38)$$

Now, we assume that these solutions hold everywhere (even in the region where z is no longer $\gg \lambda_n$). This is the actual approximation. We now go back to Eqs. (4.35) and (4.36) knowing the solutions for Δn_x and Δs_x . We can rewrite Eqs. (4.35) and (4.36) as follows

$$0 = D \frac{\partial^2 \Delta n_z}{\partial z^2} - \frac{\Delta n_z}{\tau_{rec}} + \left[\frac{G(x)}{\Delta n_x} + D \frac{\partial^2 \Delta n_x}{\partial x^2} \right] = D \frac{\partial^2 \Delta n_z}{\partial z^2} - \frac{\Delta n_z}{\tau_{rec}} + G_{eff}, \quad (4.39)$$

$$0 = D \frac{\partial^2 \Delta s_z}{\partial z^2} - \frac{\Delta s_z}{\tau_s} + \left[\frac{G_s(x)}{\Delta s_x} + D \frac{\partial^2 \Delta s_x}{\partial x^2} \right] = D \frac{\partial^2 \Delta s_z}{\partial z^2} - \frac{\Delta s_z}{\tau_s} + G_{s,eff}. \quad (4.40)$$

Here, we have gathered the terms in the square brackets into constants G_{eff} and $G_{s,eff}$, which are the effective generation rates. G_{eff} and $G_{s,eff}$ are constants with respect to z but are functions of x . It can be seen that we have successfully decoupled the each 2-D diffusion equation into two 1-D diffusion equations. The form of the solutions to Eqs. (4.39) and (4.40) is known. So that we can finally write the whole solution for Δn and Δs .

$$\Delta n(x, z) \approx \left(\frac{G_0 \tau_{rec}}{1 - \alpha^2 \lambda_n^2} \right) \left[\exp(-\alpha x) - \left(\frac{\alpha + \frac{S}{D}}{\frac{1}{\lambda_n} + \frac{S}{D}} \right) \exp(-x/\lambda_n) \right] [1 - \exp(-z/\lambda_n)], \quad (4.41)$$

$$\Delta s(x, z) \approx \left(\frac{G_{s,0} \tau_s}{1 - \alpha^2 \lambda_s^2} \right) \left[\exp(-\alpha x) - \left(\frac{\alpha + \frac{S}{D}}{\frac{1}{\lambda_s} + \frac{S}{D}} \right) \exp(-x/\lambda_s) \right] [1 - \exp(-z/\lambda_s)]. \quad (4.42)$$

Shown in Fig. 4.4 are the plots of Δn and Δs . Again we can infer the direction of the flows of Δn and Δs . The flows that contribute to I_{ph} and I_s are labeled as $J_{e,ph}$ and $J_{e,s}$. Note that the actual currents are opposite these flows. Notice also the sharp slopes near $x = 0$ for both Δn and Δs , these correspond to the surface recombination currents J_{surf} and $J_{s,surf}$, respectively. The photocurrent I_{ph} and spin photocurrent I_s is described the following:

$$I_{ph} = \iint J dx \cdot dy = \iint -e \cdot D \cdot \left. \frac{\partial \Delta n(x, z)}{\partial z} \right|_{z=0} dx \cdot dy, \quad (4.43)$$

$$I_s = \iint J_s dx \cdot dy = \iint -e \cdot D \cdot \left. \frac{\partial \Delta s(x, z)}{\partial z} \right|_{z=0} dx \cdot dy. \quad (4.44)$$

Evaluating Eqs. (4.43) and (4.44) gives us $I_{ph} \approx 6.2 \mu\text{A}$ and $I_s \approx 1.6 \mu\text{A}$. We can see that both I_{ph} and I_s have been reduced due to the presence of the surface recombination. I_{ph} was reduced to 2% of its value without surface recombination, while I_s was reduced to 16% of its value without surface recombination. The reduction in I_{ph} is much bigger than the reduction in I_s because the carrier lifetime τ_{rec} is much longer than the spin lifetime τ_s . When there was no surface recombination, carriers photogenerated moderately far away from the tunnel contact (with z comparable to λ_n) could still contribute to I_{ph} due to relatively long lifetime before recombination occurs, whereas now that there is surface recombination, these carriers could no longer contribute, since the average amount of time it takes for carriers to recombine via surface recombination is about $T_{surf} = \delta/S \approx 1.3 \times 10^{-12}$ s. Consequently, only those carriers that are really close to the tunnel contact can still be collected in this short time interval. I_s is less affected because the spin lifetime τ_s was already fast to begin with. Interestingly, the spin-polarization of the current actually increased to $P_j \approx 26\%$ mostly because of the sharp reduction in I_{ph} .

Let us now try to solve the same problem with the collection probability method. In contrast with the previous method, there is no simple and direct way of including surface recombination. However, one indirect way is to modify Eqs. (4.20) and (4.21) by insert factors to account for surface recombination.

$$J = -e \cdot f(S) \int_0^\infty G(x) \cdot \exp(-z/\lambda_n) dz = -e \cdot f(S) \cdot G(x) \cdot \lambda_n, \quad (4.45)$$

$$J_s = -e \cdot f_s(S) \int_0^\infty G_s(x) \cdot \exp(-z/\lambda_s) dz = -e \cdot f_s(S) \cdot G_s(x) \cdot \lambda_s. \quad (4.46)$$

Here, f and f_s are factors that is used to account the effect of surface recombination that depend of S . From hindsight, we can easily see than for $S = 7.7 \times 10^7$ cm/s, f has to be

about 0.02 and f_s has to be about 0.16 [from the results of Eqs. (4.43) and (4.44)]. However, if we had no known in advance that correct values of I_{ph} and I_s , there would be no way for us to relate f and f_s to S . And this is the weakness of the collection probability method.

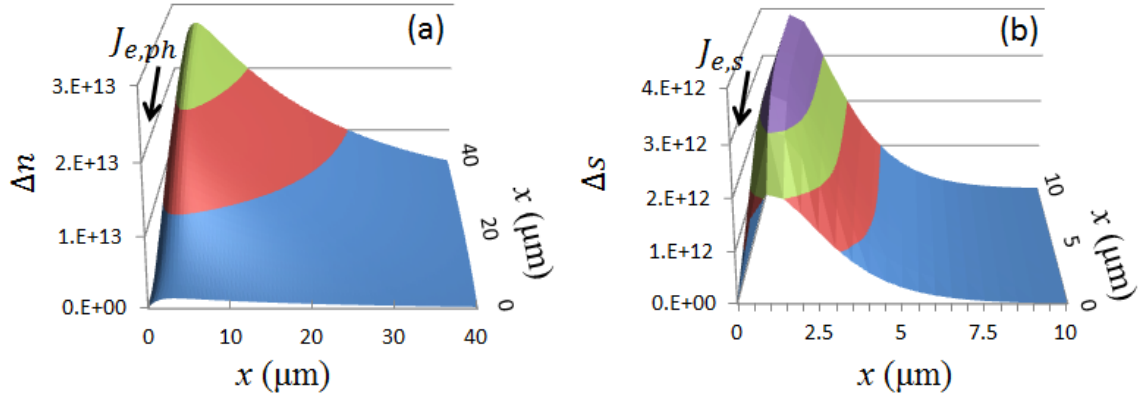


Figure 4.4 Profiles of (a) Δn and (b) Δs as functions of x and z . Parameters used are $\Phi_0 = 3.4 \times 10^{19} \text{ cm}^{-2} \text{ s}^{-1}$, $A = 1.26 \times 10^{-3} \text{ cm}^2$, $D = 62 \text{ cm}^2/\text{s}$, $\alpha = 10^4 \text{ cm}^{-1}$,²⁰ $T = 0.1$,²¹ $E = 2.1 \times 10^5 \text{ V/cm}$, $\mu = 2400 \text{ cm}^2 \text{ V}^{-1} \text{ s}^{-1}$,²⁶ $\tau_{rec} = 7.15 \times 10^{-8} \text{ s}$,²⁵ $\tau_s = 2.33 \times 10^{-10} \text{ s}$,²⁷ and $S = 7.7 \times 10^7 \text{ cm/s}$.²⁹

Additional conditions are difficult to introduce. Note that there are other ways Eqs. (4.20) and (4.21) can be modified to include surface recombination, such as by introducing effective lifetimes. Of course, these are also indirect and some form of optimization is required to make them work. Nonetheless, we have demonstrated that introducing additional conditions to the collection probability method may be difficult but is far from impossible.

4.4 Spin dependent tunneling

The third and final component of spin-PD simulation is the spin dependent tunneling. One may (incorrectly) assume that the spin photocurrent I_s is the equal to the helicity-dependent photocurrent ΔI . That is, if I_s is 5% of the photocurrent I_{ph} then ΔI must also be 5% of I_{ph} . This (incorrect) notion is based on the belief that at the tunnel contact, only the photocurrent in the spin channel that is aligned with the majority band of the ferromagnet is collected, and the other spin channel is somehow blocked. That is if the ferromagnetic tunnel contact is magnetized upward only the spin-up photocurrent I_{ph}^{\uparrow} is collected. Likewise, if we switch the direction of the magnetization of the ferromagnet only spin-down photocurrent is collected I_{ph}^{\downarrow} . If we take the difference $\Delta I = I_{ph}^{\uparrow} - I_{ph}^{\downarrow} = I_s$,

we do indeed get $\Delta I = I_s$ and hence $\frac{\Delta I}{I} = \frac{I_s}{I_{ph}} = P_J$. At first glance, this seems to make sense, but this cannot be farther from the truth. Otherwise, there would be a charge accumulation at blocked spin channel. Electrons in this channel would start flipping to the other channel, and eventually, ΔI would vanish.

The helicity-dependent photocurrent ΔI can actually become roughly equal to the value of I_s . If we had a perfect (half-metallic) tunnel contact, then indeed $\Delta I \approx I_s$ and $\frac{\Delta I}{I} \approx P_J$. But in general, this is not the case, it is easy to see that, if we replace the ferromagnet in the tunnel contact with a non-magnetic metal, I_s would be unchanged (if I_s was 5% of I_{ph} , it would still be 5% even if we replace the contact material), but ΔI would vanish (since ΔI relies on the TMR effect).

As discussed in the last section of Ch. 2, the correct approach involves the use of a modified version of the Julliere tunnel model. It is a simple matter of plugging in the value of P_J into the Eq. (2.29). This leads us to

$$\Delta I = I_{ph} \cdot \frac{\Delta R}{R} = I_{ph} \cdot \left[\frac{2P_{FM}P_J}{1-P_{FM}P_J} \right] = I_{ph} \cdot \left[\frac{2P_{FM}(I_s/I_{ph})}{1-P_{FM}(I_s/I_{ph})} \right]. \quad (4.47)$$

Here, R is the total resistance. In case external loads are added, these need to be considered in the calculation of ΔI . It can be seen that ΔI depends mostly on the spin polarization of the ferromagnet in the tunnel contact P_{FM} and the spin polarization of the photocurrent P_J . Furthermore, whereas the photocurrent current I_{ph} is continuous at the tunnel contact (i.e. the current at the ferromagnet side is equal to the current at the semiconductor side), the spin current I_s is not. The spin current at the semiconductor side is indeed I_s . At the ferromagnet, there is no spin current. At the spin channels in the tunnel barrier, the spin current is non-zero (and depends on the magnetization of the ferromagnet), but at the same time, is not equal to I_s . This is expected since the spin current is converted into a change in the charge current. This completes the discussion about the device simulation of spin-PDs.

References

- 1) C. Rinaldi, S. Bertoli, M. Asa, L. Baldrati, C. Manzoni, M. Marangoni, G. Cerullo, M. Bianchi, R. Sordan, and R. Bertacco, J. Phys. D: Appl. Phys. **49**, 425104 (2016).
- 2) M. Cartoni and C. Rinaldi, J. Appl. Phys. **120**, 104505 (2016).
- 3) I. Zutic, J. Fabian, and S. Das Sarma, Appl. Phys. Lett. **79**, 1558 (2001).
- 4) J. Fabian, A. Matos-Abiague, C. Ertler, P. Stano, and I. Zutic, Acta Phys. Slovaca **57**, 565 (2007).

- 5) J. Fabian and I. Zutic, *Semicond. Sci. Technol.* **23**, 114005 (2008).
- 6) S. A. Crooker, M. Furis, X. Lou, P. A. Crowell, D. L. Smith, C. Adelman, and C. J. Palmstrom, *J. Appl. Phys.* **101**, 081716 (2007).
- 7) R. I. Dzhioev, V. G. Fleisher, L. M. Kanskaya, O. A. Ninu, and B. P. Zakharchenya, *Phys. Status Solidi B* **50**, 39 (1972).
- 8) B. I. Zakharchenya, V. G. Fleisher, R. I. Dzhioev, Yu. P. Veshchunov, and I. B. Rusanov, *J. Exp. Theor. Phys. Lett.* **13**, 137 (1971).
- 9) M. I. D'yakonov and V. I. Perel, *J. Exp. Theor. Phys.* **65**, 362 (1973).
- 10) M. I. Dyakonov, *Spin Physics in Semiconductors* (Springer-Verlag Berlin Heidelberg, 2008) Ch. 1, pp. 12 – 13.
- 11) J. Hubner and M. Oestreich, *Semicond. Sci. Technol.* **23**, 114006 (2018).
- 12) P. Bhattacharya, D. Basu, A. Das, and D. Saha, *Semicond. Sci. Technol.* **26**, 014002 (2011).
- 13) A. Bhattacharya, M. Z. Baten, T. Frost, and P. Bhattacharya, *IEEE Photon. Technol. Lett.* **29**, 338 (2017).
- 14) M. Reuter and S. J. Eisele, *Optical Characterization of Thin Silicon in Ultra-thin Chip Technology and Applications* ed. J. N. Burghartz (Springer Science + Business, 2011) Ch. 24, p. 313.
- 15) C. S. Solanki, *Solar Photovoltaics Fundamentals, Technologies and Applications* 3rd Ed. (PHI Learning Delhi, 2015), Ch. 5, p.109.
- 16) A. A. S. Al-Omar and M. Y. Ghannam, *J. Appl. Phys.* **79**, 2103 (1996).
- 17) P. Kittidachachan, T. Markvart, D. M. Bagnall, R. Greef, and G. J. Ensell, *Sol. Energ. Mat. Sol. Cell* **91**, 160 (2007).
- 18) M. Green, *J. Appl. Phys.* **81**, 268 (1997).
- 19) U. Rau and R. Brendel, *J. Appl. Phys.* **84**, 6412 (1998).
- 20) M. D. Sturge, *Phys. Rev.* **127**, 768 (1962).
- 21) C. Rinaldi, M. Cantoni, D. Petti, A. Sottocorno, M. Leone, N. Caffrey, S. Sanvito, and R. Bertacco, *Adv. Mater.* **24**, 3037 (2012).
- 22) E. W. Williams and R. A. Chapman, *J. Appl. Phys.* **38**, 2547 (1967).
- 23) G. Duggan and G. B. Scott, *J. Appl. Phys.* **52**, 407 (1981).
- 24) H. B. de Vore, *Phys. Rev.* **102**, 86 (1956).
- 25) I. Favorskiy, D. Vu, E. Peytavit, S. Arscott, D. Paget, and A. C. H. Rowe, *Rev. Sci. Instrum.* **81**, 103902 (2010).
- 26) W. Walukiewicz, J. Lagowski, L. Jastrzebski, and H. C. Gatos, *J. Appl. Phys.* **50**, 5040 (1979).

- 27) R. J. Nelson and R. G. Sobers, *J. Appl. Phys.* **49**, 6103 (1978).
- 28) J. S. Blakemore, *J. Appl. Phys.* **53**, R123 (1982).
- 29) H. Ito and T. Ishibashi, *Jpn. J. Appl. Phys.* **33**, 88 (1994).

5. Investigation of a cleaved-edge spin-photodiode with oblique angle surface illumination

5.1 Introduction

In our first attempt to fabricate a lateral-type spin-PD, we have utilized a simple cleaved structure [shown in in Fig. 5.1 (a)].¹ The main advantage of this structure is the simplicity of the fabrication. A P-I-N spin-PD with a similar structure has previously been reported.² In contrast with this previous study, a Schottky diode has been utilized in the present work. Furthermore, in addition to direct edge-illumination into the cleaved sidewall, an investigation using oblique angle surface illumination has also been carried out. This approach has proven to be an effective technique in analyzing the spin-transport dynamics in the spin-PD. It will be shown that the F of $\approx 1.3\%$ is observed for oblique angle illumination, which is about 10 times higher than that of sidewall illumination of $F \approx 0.1\%$. This improvement in the F is due to the better photogeneration profile of spin-polarized carriers, which allows for more efficient collection of spin-polarized carriers, and the avoidance of edge related effects that tend to reduce the spin-dependent tunneling efficiency. Simulations have also been carried out. It will be shown that model calculations match fairly well the experimentally measured F for oblique angle illumination. It will also be shown that

calculations do not match the F measured for sidewall illumination, suggesting that edge related effects, such as magnetic edge curling and defects in the AlO_x tunnel barrier at the cleaved edge, are the origin of the low experimentally measured F for sidewall illumination.

5.2 Methodology

A schematic of the sample is shown in Fig. 5.1 (a). The spin-PD sample is composed of a p-GaAs ($N_A \approx 10^{18} \text{ cm}^{-3}$) layer grown by MBE on a p-GaAs (001) substrate ($N_A \approx 10^{19} \text{ cm}^{-3}$). An MBE grown 1-nm AlO_x has been used as the tunnel barrier,³ which is necessary for efficient spin-dependent tunnel contacts.⁴⁻⁶

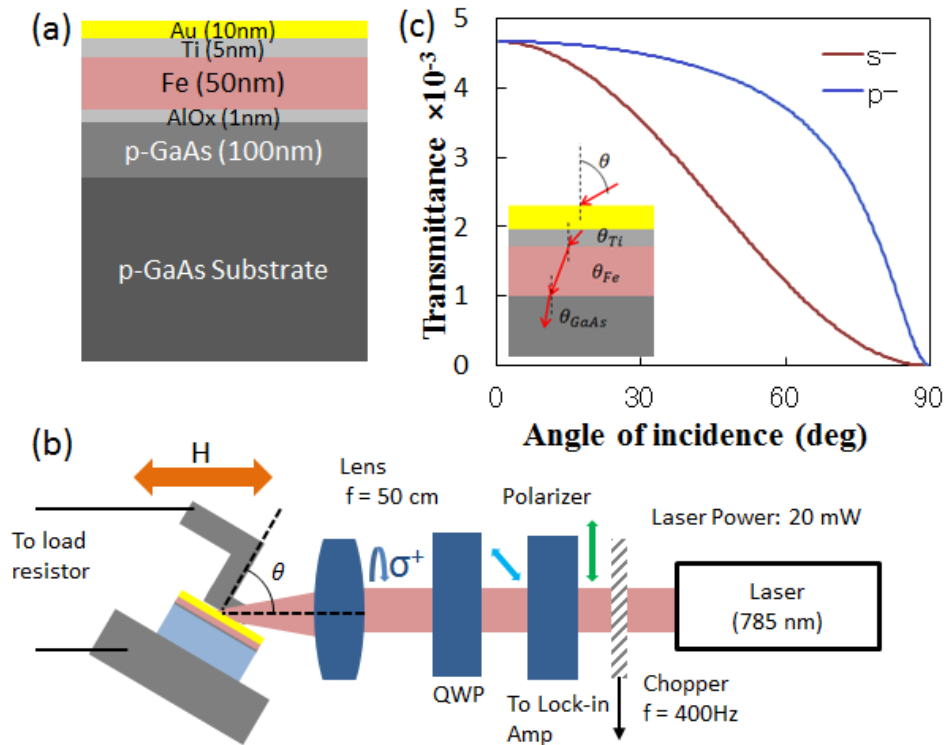


Figure 5.1 (a) Schematic cross section of the sample structure: from the top, 10-nm Au, 5-nm Ti, 50-nm Fe, 1-nm AlO_x , 100-nm Be-doped GaAs epilayer, and a p-GaAs:Zn (001) substrate. (b) Schematic of the helicity-resolved photocurrent measurement setup. Linearly polarized light from a 20mW laser was converted to CPL using LP and a QWP. The CPL beam was focused on the sample using a lens with the focal length $f = 50 \text{ cm}$. (c) Calculated transmittance of the two orthogonal linear polarizations as functions of the incidence angle θ . Inset: Schematic of refraction through the top metal layers for oblique-angle illumination with θ_{GaAs} , the angle of a light beam inside the GaAs.

A top contact composed of 50-nm-thick Fe and 5-nm Ti layers deposited by e-beam

evaporation, and a 10-nm Au layer deposited by resistive evaporation, has been used. In this case, the Fe/AlO_x junction is used as the tunnel contact, which converts the spin-photocurrent into helicity-dependent photocurrent. A 40-nm Indium layer deposited by e-beam evaporation has been used for backside contact. The fabricated sample was then annealed at 230 °C for 1 hour in ambient N₂ environment. Individual spin-PD chips of dimensions 1 mm × 1 mm were made by cleaving the sample. The magnitude of the built-in electric field in depletion region of the Fe/AlO_x/p-GaAs junction is about $\approx 2.1 \times 10^5$ V/cm.

A schematic of the helicity-resolved photocurrent measurement setup is shown in Fig 5.1 (b). Linearly polarized light from an OBIS laser of wavelength $\lambda = 785$ nm was converted into CPL by using a LP and a QWP. The helicity of the light can be switched between σ^+ and σ^- by manually rotating the QWP. The CPL beam was then focused onto the sample through a lens. The width of the beam spot (FWHM) at the sample is approximately 400 μm . An external magnetic field has been applied by using an external electromagnet. The photocurrent was measured by monitoring the voltage drop across a load resistor connected to the device. Lock-in amplification technique has been used using a mechanical chopper.

A typical measurement run sequence involves switching the helicity several times (usually starting with σ^+) while keeping the applied field unchanged. For each helicity, the photocurrent is measured for a time window of more than 50 s. The average photocurrent value for each measurement window is recorded and is treated as one data point. The standard deviation for each window is also recorded and is treated as the error. In order to avoid the influence of long term drift in the measured photocurrent, in each run, the helicity is switched an even number of times (i.e. the last helicity is the same as the first). Finally, the average value for each helicity in a run is recorded as $I_{ph}(\sigma^\pm)$ and the F is calculated by

$$F = \Delta I / I_{ph} = \frac{2 \cdot [I_{ph}(\sigma^+) - I_{ph}(\sigma^-)]}{I_{ph}(\sigma^+) + I_{ph}(\sigma^-)}. \quad (5.1)$$

Here, the I_{ph} term in the denominator is taken as the average of $I_{ph}(\sigma^+)$ and $I_{ph}(\sigma^-)$.

Furthermore, two illumination configurations were used in the measurement. As shown in Fig. 5.1 (a), the sample stage can be tilted. When $\theta = 90^\circ$, the light beam is incident on the cleaved sidewall of the spin-PD, so we call this configuration as sidewall illumination. When $\theta = 60^\circ$, the light beam is incident on top surface of the spin-PD at an oblique angle, so we call this configuration as oblique angle illumination. For the latter case, a beam scan, wherein the beam position at the top of the sample is moved while measuring the photocurrent and helicity dependent photocurrent, was also carried out.

For sidewall illumination, the geometry is fairly simple. Light is incident to the cleaved

edge or sidewall of the spin-PD. As the photons enter the spin-PD, their direction does not change. Once photons are inside the (GaAs) spin-PD, absorption occurs and spin-polarized carriers are photogenerated, which a spin axis in the same direction of the incident light. These spin-polarized carriers then diffuse towards the tunnel contact where they are collected as photocurrent. For sidewall illumination, the geometry is more complicated. In this case light is incident to the top surface of the spin-PD at an angle of incidence $\theta = 60^\circ$ with respect to the normal of the wafer plane, is then transmitted through the top metal contact, and finally makes it to the GaAs layers where absorption and photogeneration occur. In this case, due to refraction, the direction of the beam inside the GaAs ($n_{GaAs} = 3.68$) is $\theta_{GaAs} = 13.6^\circ$ with respect to the normal. Consequently, the spin axis of the photogenerated spin-polarized carriers is also oriented in this direction and this has to be taken into account in the calculations. Furthermore, the transmittance of the top metal layers is different for the s- and p- linear polarization directions, and this reduces the degree of circular polarization of the light as it passes through the metal layers from $P_c = 1$ to $P_c = T_s/T_p \approx 0.33$ [as shown in Fig. 5.1 (c)].

A model calculation has also been carried out. As discussed in the Ch. 4, the model involves three components: first, photogeneration of charge and spins, second, transport of charge and spins, and third, spin dependent tunneling. Here, spin photogeneration is accounted for by using the optical selection rules,^{7,8} whereas the transport is modelled using the drift-diffusion equation for non-equilibrium charge (electrons) Δn and spins Δs ,^{9,10} and is described by the following:

$$\frac{\partial \Delta n}{\partial t} = D \nabla^2 \Delta n + \mu E \nabla \Delta n - \frac{\Delta n}{\tau_{rec}} + G, \quad (5.2)$$

$$\frac{\partial \Delta s(\sigma^\pm)}{\partial t} = D \nabla^2 \Delta s(P) + \mu E \nabla \Delta s(\sigma^\pm) - \frac{\Delta s(\sigma^\pm)}{\tau_s} + 0.5 \cdot G \cdot P_c(\sigma^\pm). \quad (5.3)$$

Here, Δn and Δs are defined in the usual way ($\Delta n = \Delta n^\uparrow + \Delta n^\downarrow$ and $\Delta s = \Delta n^\uparrow - \Delta n^\downarrow$), and we use the parameters $D = 62 \text{ cm}^2/\text{s}$ for the electron diffusion coefficient, $\mu = 2400 \text{ cm}^2/(\text{V}\cdot\text{s})$ for the electron mobility,¹¹ $\tau_{rec} = 7.15 \times 10^{-8} \text{ s}$ for the recombination lifetime,^{12,13} $\tau_s = 2.33 \times 10^{-10} \text{ s}$ for the spin lifetime,¹³ and $P_c(\sigma^\pm) = \pm 1$ for σ^\pm the degree of circular polarization. The optical selection rules are incorporated into Eq. (5.3) through the factor 0.5 in the last term. Steady-state solutions of the form $n \approx \Delta n(x) \cdot \Delta n(y) \cdot \Delta n(z)$ and $\Delta s \approx \Delta s(x) \cdot \Delta s(y) \cdot \Delta(z)$ were used in solving Eqs. (5.2) and (5.3).

At the tunnel junction (where the photocurrent is measured), the photocurrent and spin photocurrent is described by:

$$I_{ph} = -e \iint \mu E \Delta n(z = 0) dx dy, \quad (5.4)$$

$$I_s(\sigma^\pm) = -e \iint \mu E \Delta s(z = 0, \sigma^\pm) dx dy, \quad (5.5)$$

And finally, the simulated helicity-dependent photocurrent is calculated by

$$\Delta I \approx I_{ph} \frac{\Delta R}{2R_{SPD}} = I_{ph} \left\{ \frac{\frac{1}{2}P_{Fe}[I_s(\sigma^+) - I_s(\sigma^-)]/I_{ph}}{1 - \frac{1}{2}P_{Fe}[I_s(\sigma^+) - I_s(\sigma^-)]/I_{ph}} \right\} = I_{ph} \left\{ \frac{P_{Fe}|I_s|/I_{ph}}{1 - P_{Fe}|I_s|/I_{ph}} \right\}. \quad (5.6)$$

Note that, Eq. (5.6) is based on the Julliere tunnel model,¹⁴ that was modified for a ferromagnet-insulator-semiconductor junction. The factor 2 in the denominator of $\frac{\Delta R}{2R_{SPD}}$ was included to account for the effect of the load resistor used in our photocurrent setup. The term $|I_s|/I_{ph} = P_j$ is spin polarization of the photocurrent.

We have been solved Eqs. (5.2) to (5.6) in the two configurations: sidewall illumination and oblique angle illumination [as shown in Fig. 5.2 (a) and (b)]. By comparing values from our simulations to the data from our experiments we are able to make a comprehensive analysis of the spin-PD in the present work.

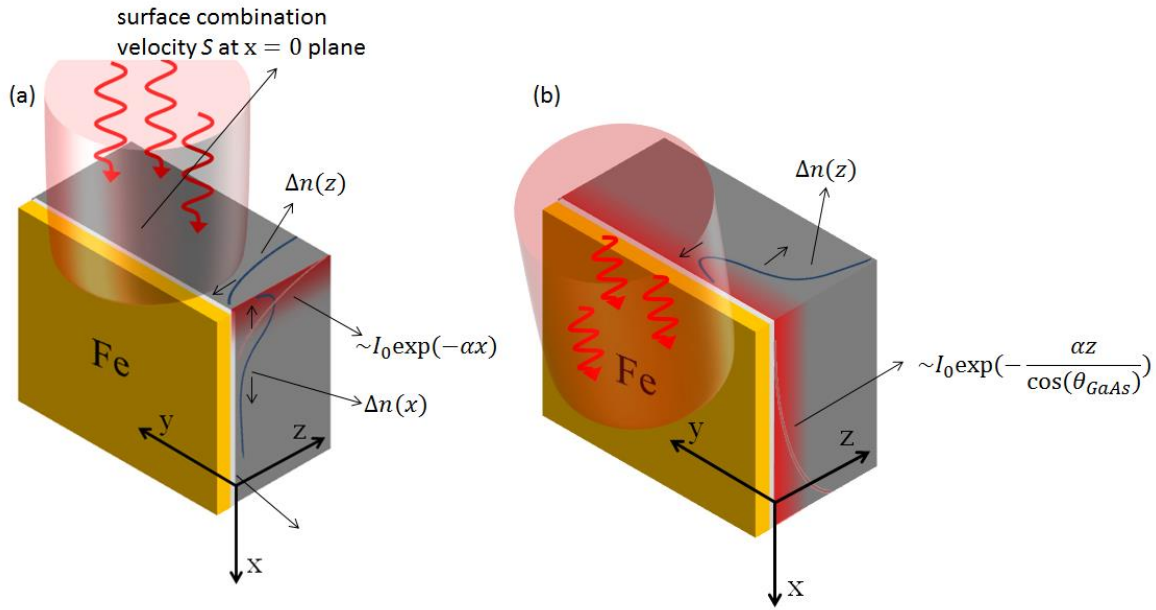


Figure 5.2 Schematic diagram of the simulation geometry for (a) sidewall illumination and (b) oblique angle illumination.

For sidewall illumination, a uniform light beam is incident into the y - z plane at $x = 0$. The generation rate G in has a spatial profile described by the Beer-Lambert law $G(x) = \alpha \cdot (1 - R) \cdot \Phi_0 \cdot \exp(-\alpha x)$. Here, we use $\alpha = 1.4 \times 10^4 \text{ cm}^{-1}$ for the absorption coefficient and $R = 0.3$ for reflectance of the air/p-GaAs interface. Additionally, Φ_0 is the photon flux of the incident beam in the unit of number of photons per cm^2 . The cleaved sidewall at $x = 0$ is assumed to have a surface recombination velocity S , which we have treated as a fitting

parameter in the simulation. The corresponding boundary condition for this is $J_{surf} = \partial \Delta n / \partial x = S \cdot \Delta n(x = 0) / D$.

For oblique angle illumination, light enters through the top surface through the top metal layers (the x - y plane at $z = 0$). As mentioned before, as the light is transmitted through the metal layers, its degree of circular polarization is reduced to from $P = 1$ to $P = T_s / T_p \approx 0.33$. The method reported by Zak¹⁵ was used to estimate the transmittance of the top metal layers as shown in Fig. 5.1 (c). The effect of MCD was ignored in the calculation. The generation rate now takes the form $G(z) = \alpha \cdot T \cdot \Phi_0 \cdot \exp(-\alpha z / \cos \theta_{GaAs}) / \cos \theta$, $\theta = 60^\circ$. We note the low transmittance of the top metal layers at 2.46×10^{-3} . As previously mentioned as well, the direction of propagation of the photon inside the GaAs not becomes $\theta_{GaAs} = 13.6^\circ$. Since, Fe layer is magnetized along the in-plane, only the component of the spins along the in-plane contributes to the helicity-dependent photocurrent. All calculates were implemented in MATLAB.

5.3 Results and discussions

Shown in Figs. 5.3 (a) and (b) are the profiles of the photogenerated charges Δn and spins Δs , respectively, for sidewall illumination. The direction of the flow of charges and spins can be inferred from the gradient of the profile. Note however that the actual current direction is opposite of these flows, directions because the charge of the electron is negative (e.g. $J_{ph} = -e \cdot J_{e,ph}$).

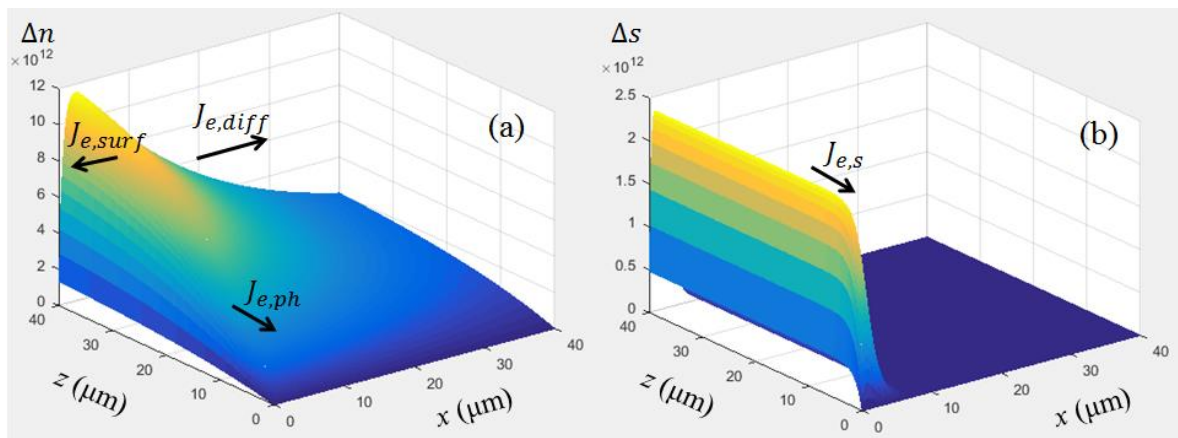


Figure 5.3 Profile of the photogenerated charges Δn and spins Δs in the z - x plane for sidewall illumination. Arrows indicate the flow of charges and spins inferred from the gradient of the profile: the diffusion current $J_{e,diff}$, the surface recombination current $J_{e,surf}$, the photocurrent $J_{e,ph}$, and the spin photocurrent $J_{e,s}$

It can be seen that photogeneration primarily happens close to the surface (within $x < 5 \mu\text{m}$). This is due to the short penetration depth δ of light in GaAs, $\delta = 1/\alpha \approx 0.7 \mu\text{m}$. It can also be seen that only a region within $z < 30 \mu\text{m}$ significantly contribute to the photocurrent and only a region within $z < 2 \mu\text{m}$ significantly contribute to the spin photocurrent. This agrees with the magnitudes of the carrier and spin diffusion lengths $\lambda_d \approx 21 \mu\text{m}$ and $\lambda_s \approx 1.3 \mu\text{m}$, respectively.

Shown in Fig. 5.4 is profile of the photogenerated spins Δs for oblique angle illumination. The corresponding profile of charges Δn is shown in the inset of Fig. 5.4. Analogously, the direction of flow of charges and spins can be inferred from the gradient direction. Note again that the actual current direction is opposite the direction of the flows. It can be seen that only a region within $z < 2 \mu\text{m}$ contributes to the spin photocurrent, and similarly, only a region within $z < 5 \mu\text{m}$ contributes to the photocurrent. In this case, optical generation only happens near the surface, within $z < 5 \mu\text{m}$, which is the reason why the flows primarily originate from near the $z = 0$ surface.

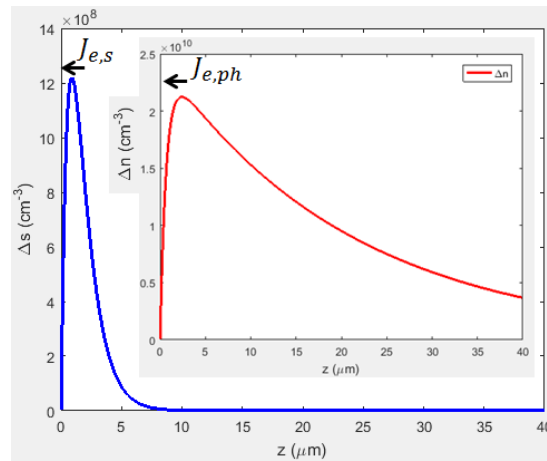


Figure 5.4 Profile of the photogenerated spins Δs along the z -direction for oblique angle illumination. Inset: Corresponding profile of the photogenerated charges Δn . Arrows indicate the flow of charges and spins inferred from the gradient of the profile: the photocurrent $J_{e,ph}$, and the spin photocurrent $J_{e,s}$.

Shown in Fig. 5.5 (a) is the temporal profile of the measured photocurrent for two opposite applied fields. Step-like profiles can be seen in the photocurrent when the helicity of the incident beam is switched. For $H = + 1.35 \text{ kOe}$, there is an increase (decrease) in photocurrent when the helicity is switched from σ^+ to σ^- (from σ^- to σ^+). Notice also that upon application of the opposite field $H = - 1.35 \text{ kOe}$ the step-like profiles reverse. This helicity-dependent photocurrent is a clear indication of spin transport. The average

amplitude of the step profile is about $\Delta I \approx 0.015 \mu\text{A}$. Taking the ratio of this with the average photocurrent value of $I_{ph} \approx 10.46 \mu\text{A}$, a F of $\approx 0.14\%$ has been calculated.

Shown in Fig. 5.5 (b) is the F as a function of the applied magnetic field H for sidewall illumination, plotted along with the M - H curve of the 50-nm Fe layer. It can be seen that although the Fe layer exhibit remanent magnetization, F is almost 0 when no field is applied. A considerable F can only be observed at applied fields with magnitude > 500 Oe.

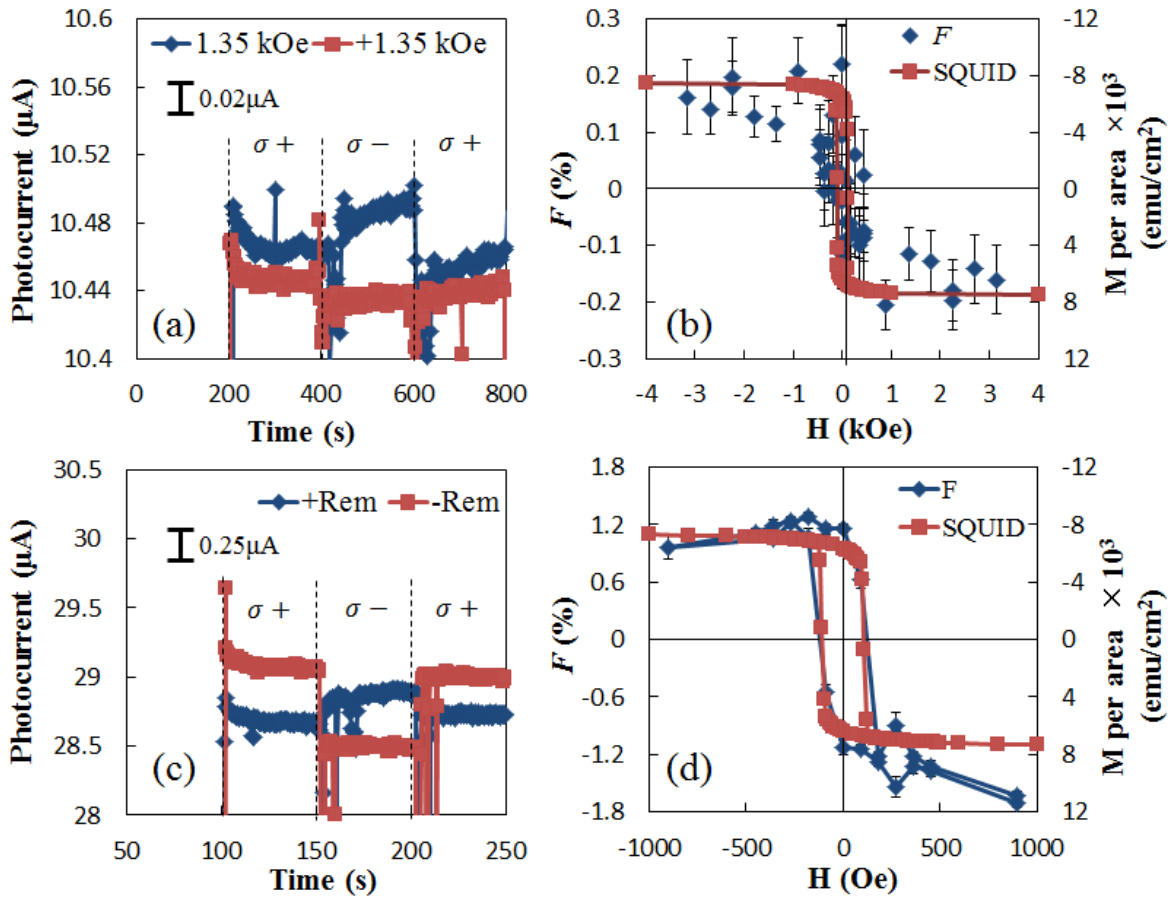


Figure 5.5 (a) Profiles of photocurrent as a function of time for two opposite applied fields $H = \pm 1.35$ kOe for sidewall illumination. (b) F as a function of applied field for sidewall illumination plotted with magnetization hysteresis loop. (c) Profiles of photocurrent as a function of time for two opposite remanent magnetization direction $+Rem$ and $-Rem$ for oblique angle illumination. (d) F as a function of applied field for sidewall illumination plotted with magnetization hysteresis loop. No applied voltage was applied for all measurements.

Shown in Fig. 5.5 (c) is the temporal profile of the measured photocurrent for two opposite remanent states for oblique angle illumination. Similar to the sidewall illumination, clear step-like profiles can be observed, but at a greater magnitude. The average step

amplitude of about $\Delta I \approx 0.33 \mu\text{A}$ is observed. Taking the ratio of this with the average photocurrent value of $I_{ph} \approx 29.0 \mu\text{A}$, a F of $\approx 1.2\%$ has been calculated. This value is about 10 times higher than that of sidewall illumination and comparable to those reported for vertical-type spin-PD.¹⁶

Shown in Fig. 5.5 (d) is the F as a function of the applied magnetic field H , for oblique angle illumination plotted along with the M - H curve of the 50-nm Fe layer. It can be seen that the F follows the profile of the M - H well.

Since light is transmitted through the top magnetic contact, there is an MCD component to the measured F . In order to estimate this MCD component, the influence of applied bias voltage to the F was investigated since the MCD component should be independent of bias. Shown in Figs. 5.6 (a) and (b) are the plots of F as a function of applied field H for applied voltage $V = -1$ and $+1$ [V], respectively. For $V = -1$ [V] (reverse bias), the Schottky depletion width is increased, and the build-in electric field is enhanced. In this case, F is nearly unchanged at $F \approx 1.2\%$. On the other hand, for $V = +1$ [V] (forward bias), the Schottky depletion width is decreased, and the build-in electric field is reduced. In this case, F is significantly reduced at $F \approx 0.4\%$. This residual F is likely due to MCD.

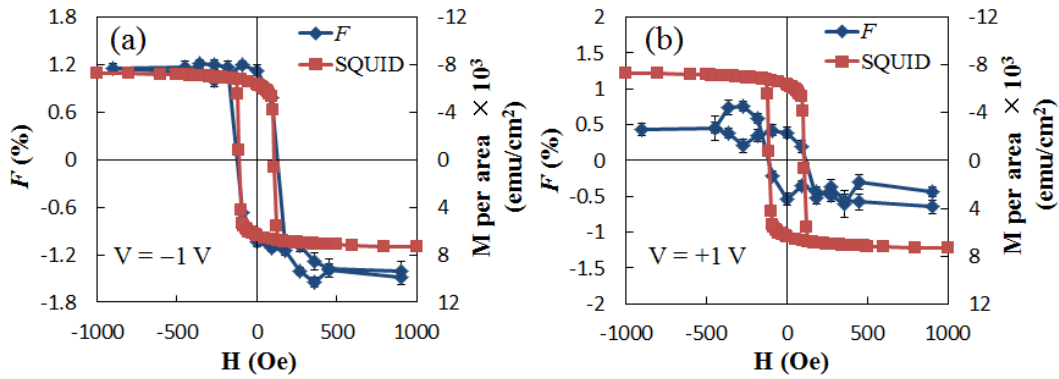


Figure 5.6 F as a function of applied field for oblique angle illumination plotted with magnetization hysteresis loop for (a) $V = -1$ [V] and (b) $V = +1$ [V].

For completeness, we have also studied the effect of the incidence oblique angle to F . Shown in Fig. 5.7 (a) is the F vs H plots for different incidence angles. It can be seen that as the angle of incidence is decreased, F (at remanence) slightly increases. This qualitatively makes sense, since for high incidence angles the difference in transmittances between the s- and p- linear polarizations increases and the degree of circular polarization of the transmitted beam decreases. We estimate that the maximum F should occur for an incidence angle of about 38° .

Shown in Fig. 5.7 (b) is the calculated photocurrent I_{ph} , helicity-dependent photocurrent ΔI , and F as functions of the surface recombination velocity S at the $x = 0$ surface for sidewall illumination and the corresponding surface recombination time T_{surf} . When S is low ($< 10^3$ cm/s), both I_{ph} and ΔI are high. This is expected, since with minimal surface recombination, the photogenerated carriers and spins are collected efficiently as photocurrent. As S increases I_{ph} and ΔI decreases, as expected. This is because the reduced collection efficiency. The onset of the decrease in I_{ph} happens at about $S \approx 10^3$ cm/s ($T_{surf} \approx 10^{-8}$ s) and levels off at $S \approx 10^7$ cm/s ($T_{surf} \approx 10^{-12}$ s), whereas the onset of the decrease in ΔI happens at a higher $S \approx 10^5$ cm/s ($T_{surf} \approx 10^{-9}$ s) and levels off at $S \approx 10^8$ cm/s ($T_{surf} \approx 10^{-13}$ s). This can be understood considering that the onsets for the decrease of I_{ph} and ΔI correspond to when T_{surf} becomes comparable to the bulk recombination lifetime τ_{rec} and the bulk spin lifetime τ_s , respectively. Furthermore, the decrease in I_{ph} is much larger than that in ΔI . For instance at $S \approx 10^7$ cm/s ($T_{surf} \approx 10^{-12}$ s), over 96% of I_{ph} is lost due to surface recombination, whereas only 64% of ΔI is lost at this S value. This becomes obvious when we take a look at the plot of F . As S increases, F actually also increases from about 2% at $S \approx 10^3$ cm/s to over 16% at $S \approx 10^8$ cm/s. This is mainly driven by the sharp decrease in I_{ph} .

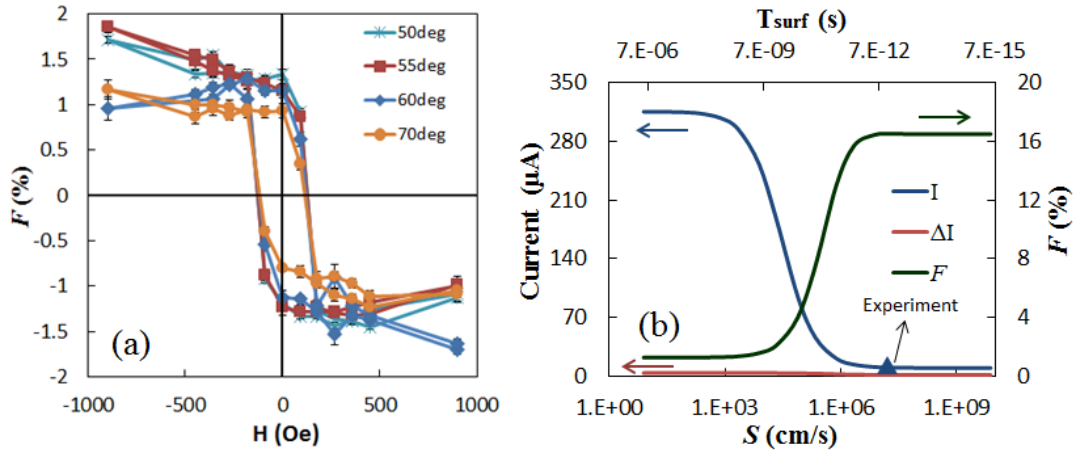


Figure 5.7 (a) Measured F vs applied field H for different incidence angles. (b) Simulated values for the photocurrent I_{ph} , helicity-dependent photocurrent ΔI , and F as functions of the surface recombination velocity S and the surface recombination time $T_{surf} = \delta/S$.

Using S as a fitting parameter and comparing the simulated photocurrent with the experimentally measured photocurrent, a good match can be achieved for $S \approx 10^7$ cm/s

($T_{surf} \approx 10^{-12}$ s). This value is comparable with that of the literature.¹⁷ This result suggests that the model can account for charge transport in the spin-PD for sidewall illumination. On the other hand, the experimental values for ΔI and F are 2 orders of magnitude than the value predicted by the simulation model. This means that the surface recombination does not explain the rather low experimentally measured F .

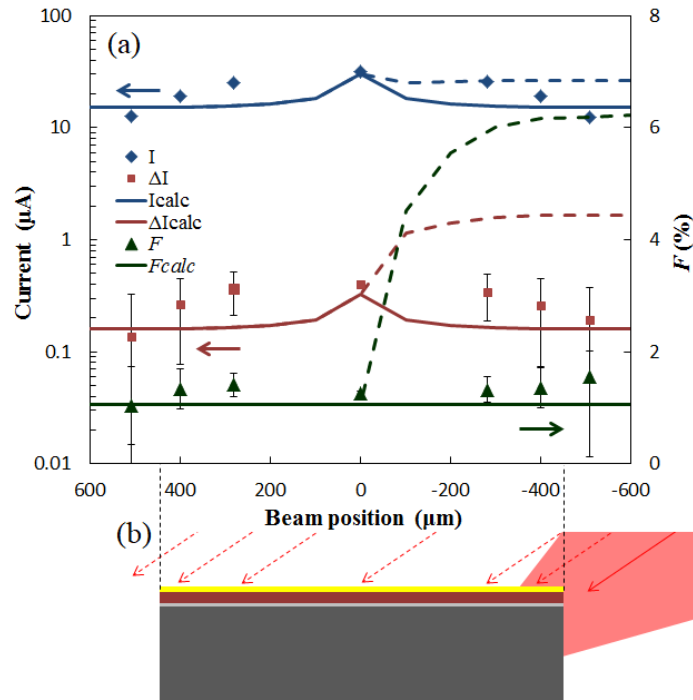


Figure 5.8 (a) Experimental photocurrent I_{ph} (blue diamonds), helicity-dependent photocurrent ΔI (red squares), and F (green triangles), simulated photocurrent I_{ph} (blue lines), helicity-dependent photocurrent ΔI (red lines), and F (green lines) plotted as functions of the beam position. Dashed and solid lines correspond to calculations with and without contribution from light hitting the sidewall, respectively. (b) A schematic diagram of the beam scan in the spin-PD.

Shown in Fig 5.8 (a) is a summary of the experimental and simulation data for oblique angle illumination plotted as functions of beam position. Two calculations were made: one including the contribution from light hitting the sidewall (dashed lines) as shown in Fig. 5.7 (b), and another without the sidewall contribution (solid lines). It can be seen that the experimental data matches well the calculation without the sidewall contribution (solid lines). The slightly higher experimental F compared with the simulation is possibly due to the MCD component, which was ignored in the model calculation. The experimental profiles are nearly symmetric. I_{ph} and ΔI have maximum values when the beam is at the center of the sample. As the beam is moved away from the center of the sample, both I_{ph}

and ΔI start to decrease, whereas F is nearly independent of the beam position. These results clearly suggest the effectiveness of the simulation model in predicting device performance particularly for the oblique angle illumination, and that calculated F values for the sidewall contribution are clearly overestimates.

There is another interesting point that we can get from the simulation results. In oblique angle illumination, even though the degree of circular polarization has been reduced to a third during the transmission through the top metal contacts and despite that the in-plane component of the photogenerated spins is small due to the steep θ_{GaAs} , an F of more than 1% was still observed, which is comparable to that of vertical-type spin-PDs. This tells us that the spin transport efficiency is high enough to compensate for these factors and yield a decent value of F . This high spin-transport efficiency comes from the fact that for oblique angle illumination (and for vertical-type spin-PDs as well) the absorption and hence photogeneration occurs mostly in the region directly below the tunnel contact. This result highlights the relative ease and effectiveness of through-the-top-contact illumination, and the difficulty and complexity of edge illumination, which also explains why most of the previous reports have been about vertical-type spin-PDs.

Finally, let us briefly address the discrepancy of the calculated F when compared with the experimental F for the sidewall illumination case. Since the validity of the model has been demonstrated for the oblique angle illumination, the only plausible explanation for the discrepancy is that there are factors that were not accounted for in the model, which are present in the fabricated spin-PD. One factor that was not accounted for in the model is magnetic edge curling.¹⁸ Since charge and spin transport occurs very near (within a few μm) the cleaved edge for sidewall illumination, the magnetization of the edge of the contact determines the spin-dependent transport (and consequently the helicity-dependent photocurrent). In case of edge curling, the magnetization at edge of the magnetic contact curls and orients perpendicular to the bulk magnetization of the film even with magnetic field application. This qualitatively explains the result that F vanishes at remanence for sidewall illumination. Applying external field, decreases the area of the curling region, which again qualitatively agrees with our results that F increases with applied field. On the other hand, even with the application of a significant field $H > 1$ kOe, F still remains small, suggesting that curling alone may not explain the low F .

Another possible explanation is the poor quality (microscopy damage or defects) of the AlO_x tunnel barrier at the cleaved edge. This would lead to the conductance mismatch problem and to loss of effective spin-dependent tunneling. The relatively small dependence

of the sidewall F to the applied field as shown in Fig. 5.4 (b) seems to qualitatively agree with this. Additional studies are required to investigate these factors, which are outside the scope of the present work. It may, however, be more practical to simply avoid the cleaved edge and its associated edge effects by changing the structure of the spin-PD to a more efficient one.¹⁹

5.4 Conclusions

Here, we have investigated the performance of a cleaved edge Fe/AlO_x/p-GaAs Schottky junction lateral spin-PD. In addition to conventional sidewall illumination experiments, oblique angle surface illumination measurements were also carried out. The spin conversion efficiency F has been determined to be 0.1% for sidewall illumination and 1.3% for oblique angle illumination. A simulation model incorporating the optical selection rules, drift-diffusion change and spin transport, and spin dependent tunneling has also been developed. Simulation results shows a good match between the experiment and simulation results for oblique angle illumination. Further comparison of the experimental and simulated results reveals that the low F for sidewall illumination is caused either by the damage in the AlO_x tunnel barrier at the cleaved edge or by magnetic edge curling. Finally, a possible solution to the low sidewall F by changing the structure of the spin-PD has also been proposed.

References

- 1) R. C. Roca, N. Nishizawa, K. Nishibayashi, and H. Munekata, Jpn. J. Appl. Phys. **56**, 04CN05 (2017).
- 2) H. Ikeda, N. Nishizawa, K. Nishibayashi, and H. Munekata, J. Magn. Soc. Jpn. **38**, 151 (2014).
- 3) N. Nishizawa and H. Munekata, J. Appl. Phys. **114**, 033507 (2013).
- 4) E. I. Rashba, Phys. Rev. B **62**, R16267(R) (2000).
- 5) D. L. Smith and R. N. Silver, Phys. Rev. B **64**, 045323 (2001).
- 6) A. Fert and H. Jaffres, Phys. Rev. B **64**, 184420 (2001).
- 7) B. I. Zakharchenya, V. G. Fleisher, R. I. Dzhioev, Yu. P. Veshchunov, and I. B. Rusanov, J. Exp. Theor. Phys. Lett. **13**, 137 (1971).
- 8) M. I. D'yakonov and V. I. Perel, J. Exp. Theor. Phys. **65**, 362 (1973).
- 9) J. Fabian, A. Matos-Abiague, C. Ertler, P. Stano, and I. Zutic, Acta Phys. Slovaca **57**, 565

(2007).

- 10) J. Fabian and I. Zutic, *Semicond. Sci. Technol.* **23**, 114005 (2008).
- 11) W. Walukiewicz, J. Lagowski, L. Jastrzebski, and H. C. Gatos, *J. Appl. Phys.* **50**, 5040 (1979).
- 12) R. J. Nelson and R. G. Sobers, *J. Appl. Phys.* **49**, 6103 (1978).
- 13) I. Favorskiy, D. Vu, E. Peytavit, S. Arscott, D. Paget, and A. C. H. Rowe, *Rev. Sci. Instrum.* **81**, 103902 (2010).
- 14) M. Julliere, *Phys. Lett. A* **54**, 225 (1975).
- 15) J. Zak, E. R. Moog, C. Liu, and S. D. Bader, *Phys. Rev. B.* **43**, 6423 (1991).
- 16) C. Rinaldi, M. Cantoni, D. Petti, A. Sottocorno, M. Leone, N. Caffrey, S. Sanvito, and R. Bertacco, *Adv. Mater.* **24**, 3037 (2012).
- 17) H. Ito and T. Ishibashi, *Jpn. J. Appl. Phys.* **33**, 88 (1994).
- 18) K. Nonaka, S. Hirono, and I. Hatakeyama, *J. Appl. Phys.* **58**, 1610 (1985).
- 19) H. Fukano, Y. Muramoto, and Y. Matsuoka, *Jpn. J. Appl. Phys.* **39**, 2360 (2000).

6. Refracting-facet spin-photodiode

6.1 Introduction

After our first attempt in fabricating a lateral-type spin-PD (cleaved spin-PD), we have learned several things, and we have decided that for our second attempt, we would design a spin-PD with these concepts in mind. For a simple cleaved-edge spin-PD, absorption (and hence photogeneration) occurs mostly near the cleaved edge. As we have found out, spin transport near the edge region leads to poor helicity-dependent photocurrent. So that first of all, the new design should avoid absorption and transport near the edge of the spin-PD. Secondly, the region where photogeneration occurs determines the spin-transport efficiency and consequently the helicity-dependent photocurrent. When photogeneration occurs near the tunnel contact, spin-transport efficiency is high. So that it is important to keep active region of the spin-PD near the tunnel contact. Thirdly, in order to bring the incident light to the active region a coupler is needed. Furthermore, the coupler should not only be able to maintain the degree of circular polarization of the incident light, but at the same time, keep the in-plane component of the photogenerated spins as high as possible. Motivated with these criteria, we have proposed a new spin-PD structure based on the refracting-facet photodiode.¹

Here, a lateral-type spin-PD with a refracting facet window is demonstrated.² In order to confine photogeneration at the active layer, the operating wavelength of the spin-PD has been set at $\lambda = 900$ nm ($h\nu = 1.38$ eV), at which the GaAs ($E_g = 1.42$ eV) substrate is

transparent. Furthermore, an $\text{In}_{0.05}\text{Ga}_{0.95}\text{As}$ ($E_g = 1.35 \text{ eV}$) active layer has been utilized. In order to achieve a high spin-transport efficiency, the thickness of the active layer is kept thin (with thickness less than the spin diffusion length $\lambda_s \approx 1.3 \mu\text{m}$). Additionally, by keeping the angle of the refracting facet near vertical, the degree of circular polarization of the light is maintained, and the in-plane component of the photogenerated spins is kept high. It will be shown that experimental F up to 0.4% was achieved, which is the highest F value for purely edge-illuminated spin-PDs so far (F of 1.3% has indeed been reported in Ch.5, but this is through oblique angle illumination which is not purely edge illumination). In addition with experiments, model simulations predict F as high as 19% for the same general device geometry. Further simulation analysis reveal that the discrepancy between the experimental and simulated F values is due to the low effective spin polarization of the Fe-based tunnel contact, which suggests that the crystalline quality of the Fe/ AlO_x tunnel junction is poorer than initially expected.

6.2 Methodology

A schematic of the spin-PD structure is shown in Fig. 6.1 (a). The wafer growth involves the following: starting with a p-GaAs (001) substrate ($N_A \sim 10^{19} \text{ cm}^{-3}$), a 280-nm-thick epitaxial p-GaAs ($N_A \sim 5 \times 10^{17} \text{ cm}^{-3}$) followed by a p- $\text{In}_{0.05}\text{Ga}_{0.95}\text{As}:\text{Be}$ ($N_A \sim 5 \times 10^{17} \text{ cm}^{-3}$) was grown by MBE. Two wafers were grown one with a thinner InGaAs active layer of thickness $d = 40 \text{ nm}$, and the other with a thicker active layer with $d = 400 \text{ nm}$. During growth, a substrate temperature of $T_s = 580^\circ\text{C}$ was used for the GaAs layer, while 510°C was used for the InGaAs layer. The wafers were then cooled to $T_s = 80^\circ\text{C}$ in order to grow the 1-nm AlO_x tunnel barrier.³

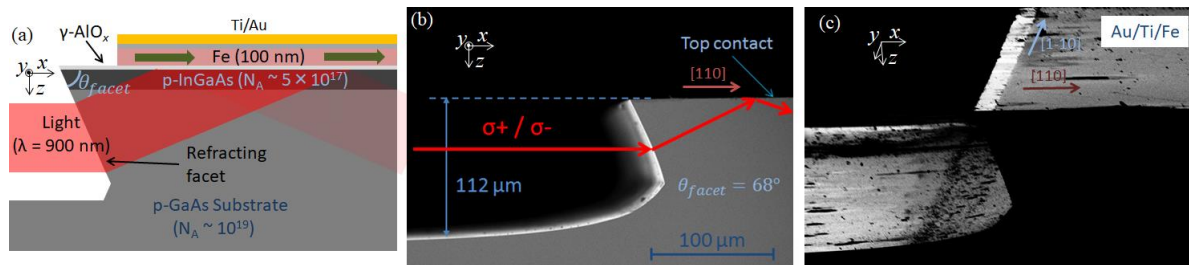


Figure 6.1 (a) Schematic of the refracting-facet spin-PD. (b) A cross-sectional SEM image of the fabricated refracting facet. (c) A bird's-eye-view SEM image of the fabricated refracting-facet spin-PD.

After the wafer growth, the samples were taken out of the MBE chamber for device

fabrication. 480- μm -wide stripe top contacts were fabricated using standard photolithography and vacuum deposition techniques. Note that the long axis of the stripe was aligned parallel to the $[1 -1 0]$ axis of the substrate. The top contact is composed of 100-nm-thick Fe and 10-nm Ti layers deposited by e-beam evaporation, and a 20-nm Au layer deposited by resistive evaporation. Similar to the previous spin-PD, the Fe/ AlO_x junction is used as the tunnel contact, which converts the spin-photocurrent into helicity-dependent photocurrent. There is a built-in electric field ($\approx 1.44 \times 10^5 \text{ V/cm}$) the Schottky depletion region of the Fe/ $\text{AlO}_x/\text{InGaAs}$. The width of the depletion region is approximately 42 nm. A 40-nm In layer was also deposited by resistive evaporation at the back side of the sample. This layer is used as the bottom contact.

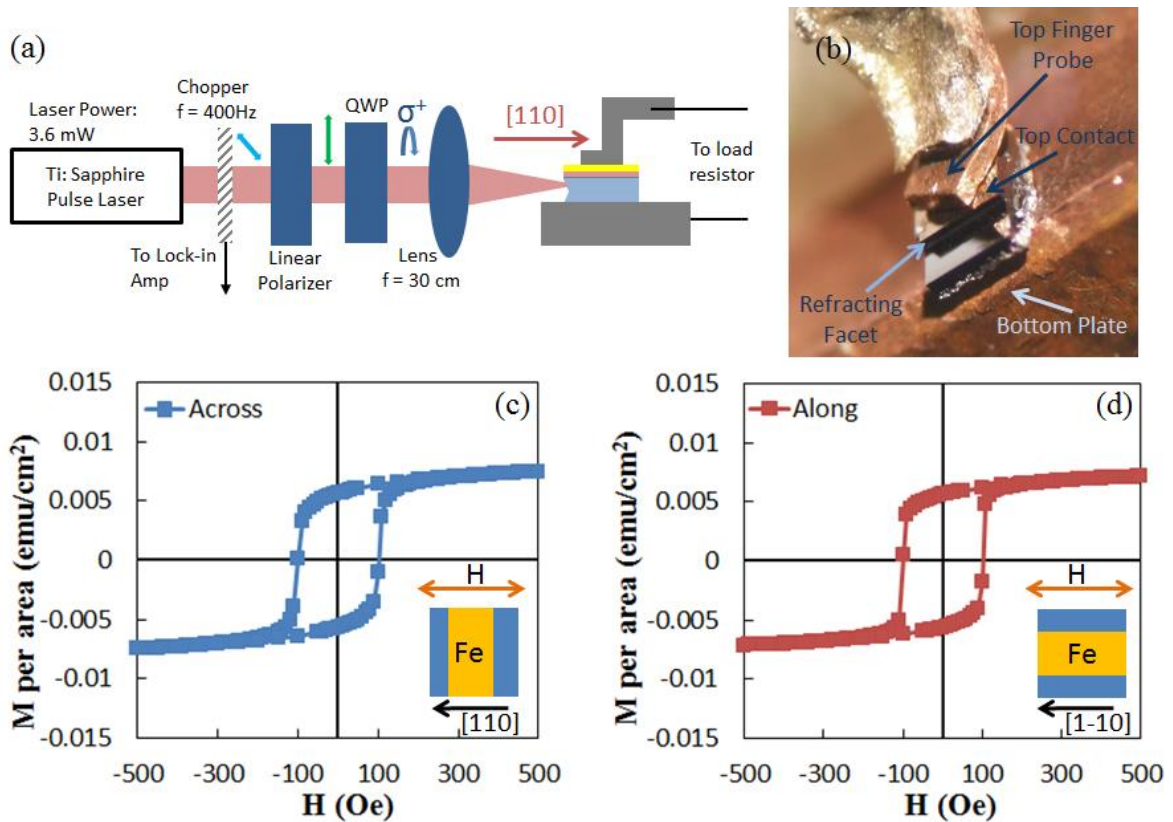


Figure 6.2 (a) Schematic of the helicity-resolved photocurrent measurement setup. (b) Image of an actual spin-PD chip mounted on a sample holder. (c) A bird's-eye-view SEM image of the fabricated refracting-facet spin-PD.

The refracting facet was then fabricated by using anisotropic wet chemical etching. A $\text{H}_2\text{SO}_4:\text{H}_2\text{O}_2:\text{H}_2\text{O}$ (1:8:1) etchant solution was used. This etchant is known to have an etching rate that is dependent on etching direction relative to the crystal orientation of GaAs.⁴ Before etching, the top contacts were protected by patterning 520- μm -wide

photoresist stripes that completely covered the top contacts. The 20- μm margin on each side of the stripes not only ensures that the top contact will be protected from the etchant, but also forms the pseudo-window [notice as how the metal contact does not extend all the way to the edge of the refracting facet in Fig 6.1 (a)] in the final spin-PD structure.⁵ In order to protect the backside contact, the wafer was mounted on a glass cover slip. The wafers were etched for a total of 30 minutes at room temperature. Mild manual stirring was applied during the etching, and the direction of the stirring was reversed every minute in order to improve the uniformity of the etching rate across the wafer.

Shown in Fig 6.1 (b) is the cross-sectional image of the resulting structure after the etching process. The tilted surface formed by the etching acts as the refracting facet. A facet angle $\theta_{facet} \sim 68^\circ$ with respect to the wafer plane, with $\pm 2^\circ$ depending on the position within the wafer was observed. This angle, however, does not correspond to the $\{1\ 1\ 1\}$ crystal plane of GaAs with an angle of 55° . A similar observation was reported in Ref. 4.

After etching, wafers were annealed at 230 $^\circ\text{C}$ for 1 hour in the ambient N_2 environment. Individual spin-PD chips were made by cleaving the wafers across the stripes (along the $[1\ 1\ 0]$ crystal direction). The dimension of the final spin-PD chips is approximately 1 mm \times 1mm. A bird's-eye-view of the fabricated device is shown in Fig. 6.1 (c).

Shown in Fig. 6.2 (a) is the helicity-resolved photocurrent setup. In this case, a Tsunami Ti:Sapphire pulse laser, with pulse width of ~ 150 fs and repetition rate ~ 80 MHz was used in order to vary the central excitation wavelength from 840 (1.48 eV) to 930 nm (1.33 eV). Similar to the setup used in the measurement of the previous spin-PD, CPL is generated by converting light from the pulse laser using a LP and a QWP. The helicity of the CPL beam can be switched by rotating the QWP. A lens of focal length 30 cm was used to focus the CPL beam to a spot of diameter ($1/e^2$) 450 μm at the sample. Lock-in technique was implemented using a mechanical chopper. The power of the beam (measured by interrupting the beam with a power meter) is maintained at 3.6 mW (28 nJ/cm² per pulse) for all measurements. The photocurrent was measured by monitoring the voltage drop across a load resistor connected to the device. Shown in Fig. 6.2 (b) is a spin-PD chip mounted on a sample holder. A Cu finger probe is attached to the top contact of the spin-PD, while the bottom contact is attached to a Cu plate.

Before each measurement run, the magnetization of the Fe layer was aligned by applying an external magnetic field with magnitude > 500 Oe using a hand held permanent magnet. The field is applied parallel to the $[1\ -1\ 0]$ crystal direction. A typical run sequence involves switching the helicity several times (usually starting with σ^+) while not applying any field.

For each helicity, the photocurrent is measured for a time windows of more than 50 s. The average photocurrent value for each measurement window is recorded and is treated as one data point. The standard deviation for each window is also recorded and is treated as the error. In order to avoid the influence of long term drift in the measured photocurrent, in each run, the helicity is switched an even number of times (i.e. the last helicity is the same as the first). Finally, the average value for each helicity in a run is recorded as $I_{ph}(\sigma^\pm)$ and the F is calculated by

$$F = \Delta I / I_{ph} = \frac{2 \cdot [I_{ph}(\sigma^+) - I_{ph}(\sigma^-)]}{I_{ph}(\sigma^+) + I_{ph}(\sigma^-)}. \quad (6.1)$$

Here, the I_{ph} term in the denominator is taken as the average of $I_{ph}(\sigma^+)$ and $I_{ph}(\sigma^-)$. Moreover, runs are carried out in pairs of opposite remanent magnetization states to ensure that the measured the helicity-dependent photocurrent values do come from spin-transport.

Shown in Fig. 6.2 (c) and (d) are the M - H curves of the Fe top contact measured by SQUID along two directions: across (in the $[1\ 1\ 0]$ direction) and along (in the $[1\ -1\ 0]$ direction) the long axis of the stripe. For both cases, coercivity of about 100 Oe was observed. Owing to the large dimensions of the stripe (in the order of mm), there is no observable magnetic shape anisotropy within the wafer plane.

In addition to experiments, a model simulation has also been carried out. Similar to the previous chapter, the model involves three components: optical spin and carrier generation, spin and carrier transport, and spin-dependent tunneling. The first and last components are essentially identical to that used in the previous chapter, while the second component was mainly adopted from Ref. 6. In particular, instead of solving the drift-diffusion equation, we simply consider the rate of photogeneration for each point in the active layer, and then calculate the contribution of each point to the photocurrent and spin-photocurrent by taking into account the distance between each point to the tunnel contact (discussed in detail in Ch. 4).

After the light transmitting through the refracting facet, it is refracted towards the active layer, and upon entering the active layer, propagates at an angle θ_{InGaAs} with respect to the wafer plane. In the optimization of our facet etching process, it was found that the facet angle θ_{facet} , depending on the exact etching conditions, can have values between 65° and 85° . So that, we first consider the facet angle $\theta_{facet} \sim 75^\circ$, for which $\theta_{InGaAs} \sim 15.6^\circ$. In the illuminated active region, the number of photogenerated electrons Δn and in-plane component of spins s_x per unit time are proportional to optical intensity. We have adopted the notation used in Ref. 6.

$$\Delta n = \eta \cdot \Phi, \quad (6.2)$$

$$s_x(\sigma^\pm) = \eta \cdot \Phi \cdot 0.5 \cdot P_c(\sigma^\pm) \cdot \cos(\theta_{InGaAs}). \quad (6.3)$$

Here, η is the effective quantum efficiency in units of cm^{-1} , Φ is the photon flux in units of $\text{cm}^{-2} \cdot \text{s}^{-1}$, P_c is the circular polarization [$P_c(\sigma^\pm) = \pm 1$]. The optical selection rules are incorporated into Eq. (6.3) through the factor 0.5. The photon flux is directly related to the light intensity W , $\Phi = W/h\nu$, where $h\nu$ is the photon energy. Due to the geometry of the spin-PD, incident photons pass through the active layer two times: once going up towards the top contact and once more after being partially internally reflected off the top contact. This effectively doubles the thickness of the active layer. The total photon flux Φ is therefore the sum of the photon fluxes due to the first and the second passes. Furthermore, the fact that pulse excitation was used in the experiment is of no consequence. Equations (6.2) and (6.3) hold for the time-average values of Δn , s_x , and Φ . Assuming only band-to-band transitions, the conservation of energy demands that, for any given time interval, the number of photogenerated spin-polarized carriers must be equal to the number of absorbed photons, whether the photons are continuous wave or pulse.

The total photocurrent is proportional to Δn summed along the z coordinate over the active layer thickness.

$$\begin{aligned} I_{ph} &= e \cdot A \int_0^d \Delta n \, dz = e \cdot A \int_0^d \eta \cdot (\Phi_1 + \Phi_2) \exp(-z/\lambda_z) \, dz \\ &= \frac{e \cdot A \cdot W_0 \cdot T \cdot f}{h\nu \cdot \sin(\theta_{InGaAs})} \eta \cdot \left[\int_0^d W_1(z) \exp(-z/\lambda_n) \, dz + \int_0^d W_2(z) \exp(-z/\lambda_z) \, dz \right]. \end{aligned} \quad (6.4)$$

Here, e is the magnitude of the electron charge, A is the illuminated area in the active region, $\Phi_1 = \frac{W_0 \cdot T}{h\nu \cdot \sin(\theta_{InGaAs})} W_1(z)$ and $\Phi_2 = \frac{W_0 \cdot T}{h\nu \cdot \sin(\theta_{InGaAs})} W_2(z)$ are the photon fluxes for the first and second passes, respectively, W_0 the intensity of the incident light beam, T (≈ 0.68) the facet transmittance, the $\exp(-z/\lambda_n)$ term is the collection probability (discussed in Ch. 4), f the voltage dependent transport efficiency, d the thickness of the active region, and $W_1(z)$ and $W_2(z)$ are the relative light intensity profiles inside the active layer, described by the following:

$$W_1(z) \sim \exp\left[\frac{-(d-z)}{\delta \cdot \sin(\theta_{InGaAs})}\right], \quad (6.5)$$

$$W_2(z) \sim R \cdot \exp\left[\frac{-(z+d)}{\delta \cdot \sin(\theta_{InGaAs})}\right], \quad (6.6)$$

$$\frac{1}{\delta \cdot \sin(\theta_{InGaAs})} \cdot \int_0^{d \rightarrow \infty} [W_1(z) + W_2(z)] \, dz = 1. \quad (6.7)$$

Here, we use $R \approx 0.54$ for the internal reflectivity of the Au/Ti/Fe/InGaAs interface, and $\delta \approx 1 \, \mu\text{m}$ for the optical penetration depth in the active region. Note that the factor f is the

constant of proportionality between the total number of photogenerated carriers and the photocurrent (therefore $f \leq 1$).

One interesting point here is that, because of the relatively small propagation angle of the light in the active layer $\theta_{InGaAs} \sim 15.6^\circ$, the effective optical penetration depth along the z -axis, $\delta_{eff} = \delta \cdot \sin(\theta_{InGaAs}) \approx 0.27 \mu\text{m}$, is much shorter compared actual penetration depth $\delta \approx 1 \mu\text{m}$. This means the distance traveled by the light is about 4 times the actual thickness of the active layer, and hence, a relatively thin active layer can be used without losing too much absorbance.

For the spin-photocurrent, an analogous approach is taken, but this time the spin relaxation has to be taken into account. The spin-photocurrent is described by

$$\begin{aligned} I_s(\sigma^\pm) &= e \cdot A \int_0^d s_x(\sigma^\pm) \exp(-z/\lambda_n) \exp(-z/\lambda_s) dz \\ &= e \cdot A \cdot 0.5 \cdot P_c(\sigma^\pm) \cdot \cos(\theta_{InGaAs}) \int_0^d [\eta \cdot (\Phi_1 + \Phi_2) \cdot \exp(-z/\lambda_n) \exp(-z/\lambda_s)] dz. \end{aligned} \quad (6.8)$$

Here, the spin spin relaxation is accounted for by the spin collection probability, $\exp(-z/\lambda_s)$ factor (discussed in Ch.4). Note that Φ_1 and Φ_2 are defined in the same was as that of Eq. (6.4). We use $\lambda_s \approx 1.3 \mu\text{m}$ for the spin diffusion length. The maximum I_s is half of I_{ph} , which happens when the factor $\cos(\theta_{InGaAs}) = 1$ (incident light is parallel to the wafer plane) and the exponential factor in Eq. (6.9) approaches 1 (or when $d \rightarrow 0$).

As discussed in Ch. 4, calculating the experimentally measurable helicity-dependent photocurrent ΔI from the simulated I_s and I_{ph} is a simple matter of inserting them into the modified Julliere model.

$$\Delta I \approx I_{ph} \frac{\Delta R}{2R_{SPD}} = I_{ph} \left\{ \frac{\frac{1}{2} P_{Fe} [I_s(\sigma+) - I_s(\sigma-)] / I_{ph}}{1 - \frac{1}{2} P_{Fe} [I_s(\sigma+) - I_s(\sigma-)] / I_{ph}} \right\} = I_{ph} \left\{ \frac{P_{Fe} |I_s| / I_{ph}}{1 - P_{Fe} |I_s| / I_{ph}} \right\}. \quad (6.9)$$

Here, we use $P_{Fe} \approx 0.42$ for the spin polarization of Fe. Note that Eq. (6.10) was adopted from Julliere TMR model, and the factor 2 in the denominator of $\frac{\Delta R}{2R_{SPD}}$ was included to account for the effect of the load resistor used in our photocurrent setup. The figure of merit F can then be calculated as follows: $F = \Delta I / I_{ph} = \Delta R / (2R_{SPD}) = P_{Fe} |I_s| / I_{ph} / (1 - P_{Fe} |I_s| / I_{ph})$. The term $P_j = |I_s| / I_{ph}$ is spin polarization of the photocurrent. All numerical calculations were implemented in MATLAB.

In case of the ideal (half-metallic) spin tunnel contact ($P_{ideal} = 1$ instead of $P_{Fe} \approx 0.42$) and assuming moderate P_j ($P_j \ll 1$, which is usually the case), the helicity-dependent photocurrent ΔI is approximately $\Delta I \approx I_{ph} \frac{\Delta R}{2R_{SPD}} \approx |I_s|$. In this case, the entire spin-photocurrent $|I_s|$ is converted into helicity-dependent photocurrent ΔI . This condition

was used in Ref. 6, which led to a low estimate of the spin diffusion length λ_s . In the present work, we do not assume this condition and use a realistic spin polarization $P_{Fe} \approx 0.42$ for our tunnel contact.

6.3 Results and discussions

Shown in Fig. 6.3 (a) are the simulated photocurrent I_{ph} and spin-photocurrent I_s as functions of the active layer thickness d . Parameters used are $W_0 = 2.3 \text{ W/cm}^2$, $A = 6.4 \times 10^{-3} \text{ cm}^2$, $\eta = 0.9 \cdot \alpha$, $\alpha = 10^4 \text{ cm}^{-1}$, $T = 0.68$, $f = 0.9$, and $R = 0.54$. As the active layer thickness d increases, I_{ph} increases monotonically (reflecting the increasing total absorbance), and then saturates at about $d = 1 \text{ }\mu\text{m}$.

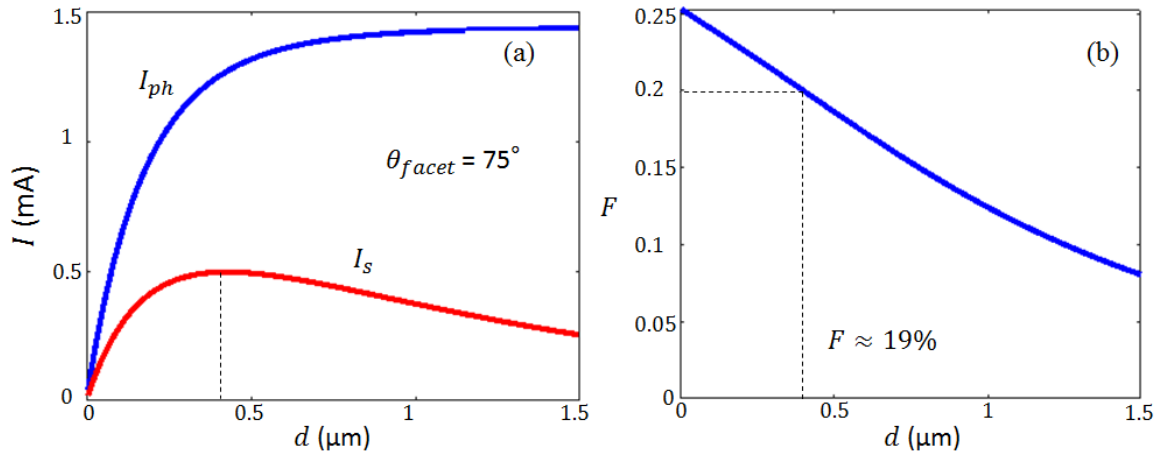


Figure 6.3 (a) Calculated photocurrent I_{ph} and spin-photocurrent I_s as functions of the active layer thickness d . (b) Calculated F as a function of d .

This is expected since at $d = 1 \text{ }\mu\text{m}$, most of the incident photons are already absorbed, and that any further increase in thickness only leads to a marginal increase in I_{ph} . On the other hand, I_s initially increases with d , reaches a maximum at about $d \approx 0.4 \text{ }\mu\text{m}$ (marked by the dashed line), and starts to decrease with further increase in d . Similar with I_{ph} , the initial increase in I_s comes from the increase in total absorbance (and hence photogeneration), whereas the decrease in I_s for $d > 0.4 \text{ }\mu\text{m}$ comes from the increased spin relaxation associated with the increase in transport distance (from the point of photogeneration to the tunnel contact). While the spin relaxation always increases with transport distance, for $d < 0.4 \text{ }\mu\text{m}$ the increase in photogeneration is enough to offset the increase in spin relaxation, resulting in an overall increase in I_s with d . On the other hand, $d > 0.4 \text{ }\mu\text{m}$ the increase in photogeneration starts to drop due to saturation and no longer enough to offset the increase

in spin relaxation, resulting in the decrease in I_s with d . Therefore $d \approx 0.4 \mu\text{m}$ is the optimum active layer thickness that yields the maximum I_s , at which the balance between photogeneration and spin transport is achieved.

Shown in Fig. 6.3 (b) is the calculated F as a function of d . As d increases, F monotonically decreases, reflecting the increasing spin relaxation (decreasing spin transport efficiency). This is expected since from Eq. (6.10), F directly depends on the P_j [since $F = P_{Fe}P_j/(1 - P_{Fe}P_j)$], and from Eqs. (6.8) and (6.9) P_j has a maximum value of about ≈ 0.5 as $d \rightarrow 0$, and then monotonically decreases as d increases. Nevertheless, the calculated F of 19% at $d \approx 0.4 \mu\text{m}$ is impressive. This value is much higher than anything reported (including those for vertical-type spin-PD) up to now.

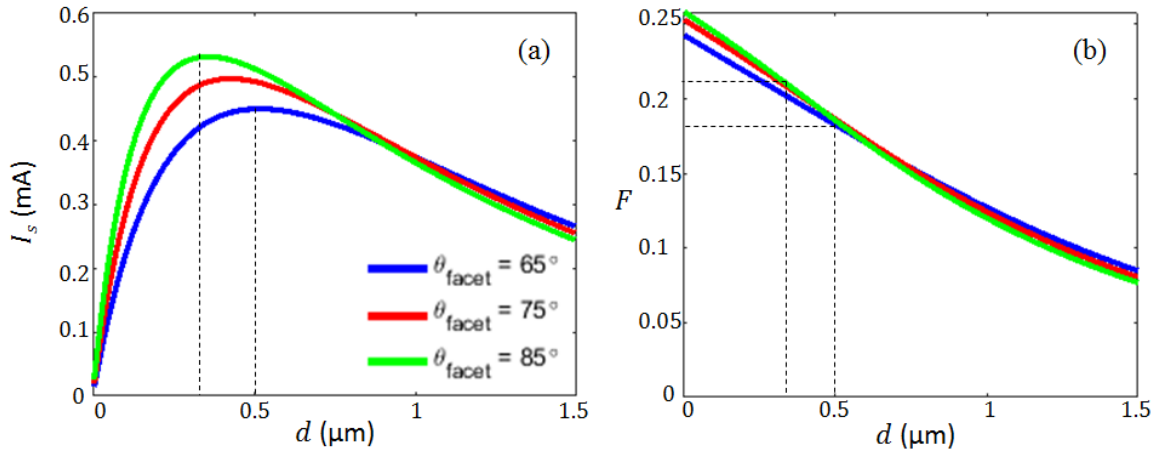


Figure 6.4 Calculated spin-photocurrent I_s (a) and F (b) for θ_{facet} : 65° (blue), 75° (red), and 85° (green) as functions of the active layer thickness d .

We have also studied the effect of the facet angle θ_{facet} to the performance of the spin-PD. As previously mentioned, the facet angle θ_{facet} can have values between 65° and 80° , so here we have calculated the effect of an angular variation of $\pm 10^\circ$ from $\theta_{\text{facet}} \sim 75^\circ$. In the first order approximation, we can assume that all parameters are the same except those that have an explicit θ_{facet} (and hence θ_{InGaAs}) dependence. Shown in Fig. 6.4 (a) are the corresponding I_s for three different facet angles θ_{facet} : 65° (blue), 75° (red), and 85° (green). It can be seen that the general I_s trend for the three facet angles are similar, except that the positions of the maximum I_s tend to occur at different d values and the values of the maximum I_s tend to slightly differ. The position of the maximum I_s shifts from $d \approx 0.5 \mu\text{m}$ to $d \approx 0.3 \mu\text{m}$ (marked by dashed lines) and maximum value of I_s increases from \approx

0.45 to mA to ≈ 0.53 mA as θ_{facet} increases from 65° to 85° . These are expected considering that as θ_{facet} increases from 65° to 85° , θ_{InGaAs} decreases from 21.4° to 11.8° , so that the effective optical penetration depth $\delta_{eff} = \delta \cdot \sin(\theta_{InGaAs})$ also decreases. This means that for a large facet angle $\theta_{facet} \approx 85^\circ$, the light inside the active layer is almost parallel to the wafer plane and hence a much higher absorbance is achieved for a relatively thinner d , hence the shift of the position of the maximum I_s to a smaller d value. At the same time, this thinner d also corresponds to an improved spin transport (lower spin relaxation) which explains the increase in maximum I_s .

Shown in Fig. 6.4 (b) are the corresponding F values for the three different facet angles θ_{facet} : 65° (blue), 75° (red), and 85° (green). For all angles, F monotonically decreases as d increases. There are slight differences in the slopes of the decrease in F due to the charged δ_{eff} , but for a given d , F does not vary very much with θ_{facet} (for $d = 0.4 \mu\text{m}$ for instance, F varies from about 18% to 20%). The optimum range for d is about 0.3 to 0.5 μm , for which I_s is maximized and a resulting F of about 18% to 22% is expected. In practice however, it is desirable to choose just one thickness d . In this case, the best choice would be $d = 0.4 \mu\text{m}$, which should accommodate small variation in θ_{facet} without too much effect on F .

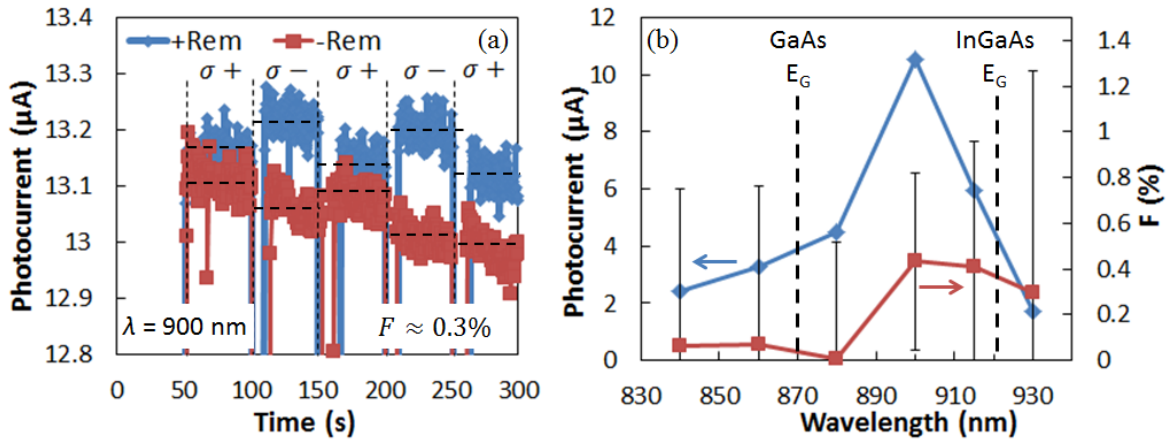


Figure 6.5 (a) Temporal plot of the measured photocurrent I_{ph} from a spin-PD with $d = 0.4 \mu\text{m}$ for two remanent magnetization states. (b) Plot of I_{ph} and F as functions of the wavelength of the incident beam.

Shown in Fig. 6.5 (a) is measured photocurrent I_{ph} plotted against time taken from a fabricated spin-PD with $d = 0.4 \mu\text{m}$, for two remanent magnetization states: magnetized along the $+x$ -axis (+Rem) and along the $-x$ -axis -Rem. No bias voltage is applied. Step-like profiles can be seen in the photocurrent when the helicity of the incident beam is switched.

Note that for +Rem case, there is an increase (decrease) in photocurrent when the helicity is switched from σ^+ to σ^- (from σ^- to σ^+). Notice also that for the –Rem case, the step-like profiles are reverse. This helicity-dependent photocurrent is a clear indication of spin transport.

A slight drift, in the order of less than 1%, can be seen particularly in the –Rem data. This likely comes from a slight mechanical drift of a mirror (not shown) used to steer the incident laser beam onto the device. We estimate that the angular drift in the order of 10^{-6} deg. causes approximately 1% change in the photocurrent for the mirror-to-sample distance of 85 cm. This drift, however, is averaged out of our measurements by the designing a run sequence in which the helicity switched an even number of times. This kind of run sequence (e.g. $\sigma^+ \rightarrow \sigma^- \rightarrow \sigma^+ \rightarrow \sigma^- \rightarrow \sigma^+$) is an “odd” sequence (the steps from the start to half-way of the run is the same as the steps from half-way of the run to the end but in reverse order).

Shown in Fig. 6.5 (b) is the wavelength dependence of photocurrent I_{ph} and spin conversion efficiency F . No bias was applied here as well. Note also that the power was kept 3.6 mW for all measurements. It can be seen that I_{ph} and F are maximum at $\lambda = 900$ nm ($h\nu = 1.38$ eV) as expected. It is assumed that at this wavelength, photons travel through the GaAs substrate without absorption, and absorbed only at the InGaAs active layer. Because of the proximity of the InGaAs layer to the tunnel contact, efficient charge and spin transport occurs at this wavelength. As the wavelength is increased from 900 nm to 930 nm, both I_{ph} and F decrease. This is due to the decrease in the absorption coefficient of the InGaAs active layer (and hence photogeneration) for photon energies around and below the InGaAs bandgap of 1.35 eV (with corresponding wavelength of $\lambda = 920$ nm). As the wavelength is decreased from 900 nm to 840 nm, again both I_{ph} and F decrease. This is due to the increase in the absorption coefficient of the GaAs substrate for photon energies around and above the GaAs band gap of 1.42 eV (with corresponding wavelength of $\lambda = 870$ nm). When photons are absorbed in the GaAs, due to conservation of energy, the number of photons arriving at the InGaAs substrate decreases. Furthermore, photogenerated carriers and spins in the GaAs do not contribute effectively to I_{ph} and F due to the large travel distance between the point of photogeneration (deep inside the GaAs) to the tunnel contact. In this case, spin transport is affected significantly more (due to the short $\lambda_s \approx 1.3$ μm) than carrier transport (with $\lambda_d \approx 21$ μm), and this qualitatively agrees with the sharp decrease in F and the relatively milder decrease in I_{ph} as the wavelength decreases.

An F of around $\approx 0.4\%$ was obtained for $\lambda = 900$ nm. This value is about 4 times higher

than that obtained from our previous spin-PD (the simple cleaved spin-PD), yet this is still far lower than the value predicted in our simulations. In an attempt to increase the performance of the spin-PD, bias dependence of I_{ph} and ΔI was also carried out. When a reverse (negative) bias is applied to the spin-PD, the width of the depletion region is increased and the built-in electric field is enhanced. This is expected to promote more efficient transport of spin-polarized carriers towards the tunnel contact.

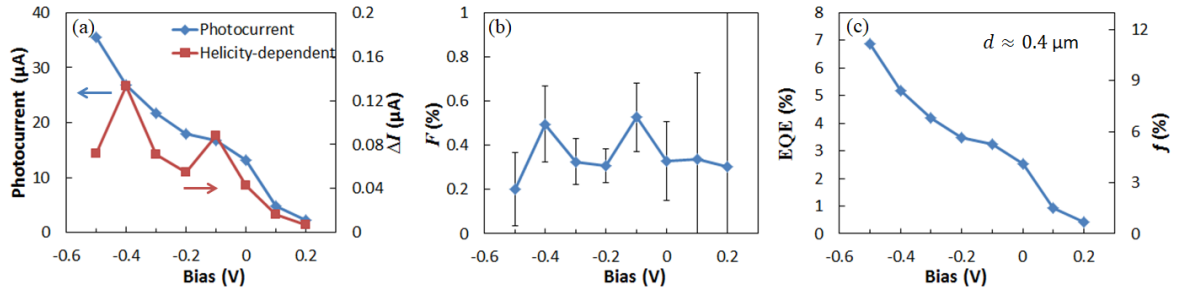


Figure 6.6 (a) Plot of I_{ph} and ΔI as functions of the applied bias voltage for the spin-PD with $d = 0.4 \mu\text{m}$. (b) Plot of F as a function of bias. (c) Plot of the estimated EQE and f as functions of bias.

Shown in Fig. 6.6 (a) is the plot of I_{ph} and ΔI as functions of the applied bias voltage. It can be seen that when an increasing reverse bias is applied, both I_{ph} and ΔI increase as expected. On the other hand, when a forward bias is applied, both I_{ph} and ΔI decrease. The forward bias narrows of the width of the depletion region as well as counteracts the built-in electric field.

Shown in Fig. 6.6 (b) is the plot of F as a function of bias. In contrast with I_{ph} and ΔI , F is largely independent of the applied bias with an average of about $F \approx 0.3 \pm 0.1\%$. This may seem counter-intuitive, but upon closer examination of Eqs. (6.4) and (6.8), it can be seen that the voltage dependent factor f cancels out when we compute for F . In the first order approximation, f is the only parameter with a direct voltage dependence. Note, however, that with a sufficiently high bias λ_s also changes and becomes a function of bias, but this is not the case here, where only mild voltages (less than 1 V) has been applied.^{7,8}

Shown in Fig. 6.6 (c) is a plot of the external quantum efficiency (EQE) as a function of voltage and its corresponding collection efficiency f . Since the EQE is directly proportional to the photocurrent (by definition $\text{EQE} = \text{number of carriers collect} / \text{number of incident photons}$), the EQE naturally follows the trend of I_{ph} . The EQE is improved from 2.5% at no bias to 6.8% by the application of a reverse bias voltage of -0.5 V , and is reduced to 0.4%

with forward bias of +0.2 V. Note that the EQE of the present spin-PD is relatively low compared with those of conventional photodiodes of similar structure (with typical EQE of more than 30%),⁹ but is slightly higher than that reported for vertical-type spin-PD.¹⁰ On the other hand, the collection efficiency f here possess the same profile as the EQE, which is expected since EQE and f are directly proportional to each other. Furthermore, f is closely related to the internal quantum efficiency (IQE), with the only distinction being that the IQE also includes losses associated with free carrier absorption (and other transitions that are not band-to-band), whereas f only considers band-to-band absorption. For the present work, f and IQE are essentially the same. Note also that, although the f value used in the simulation is much higher than the experimentally measured f , but does not have an effect to the prediction of the model since f is cancelled in the calculation of F .

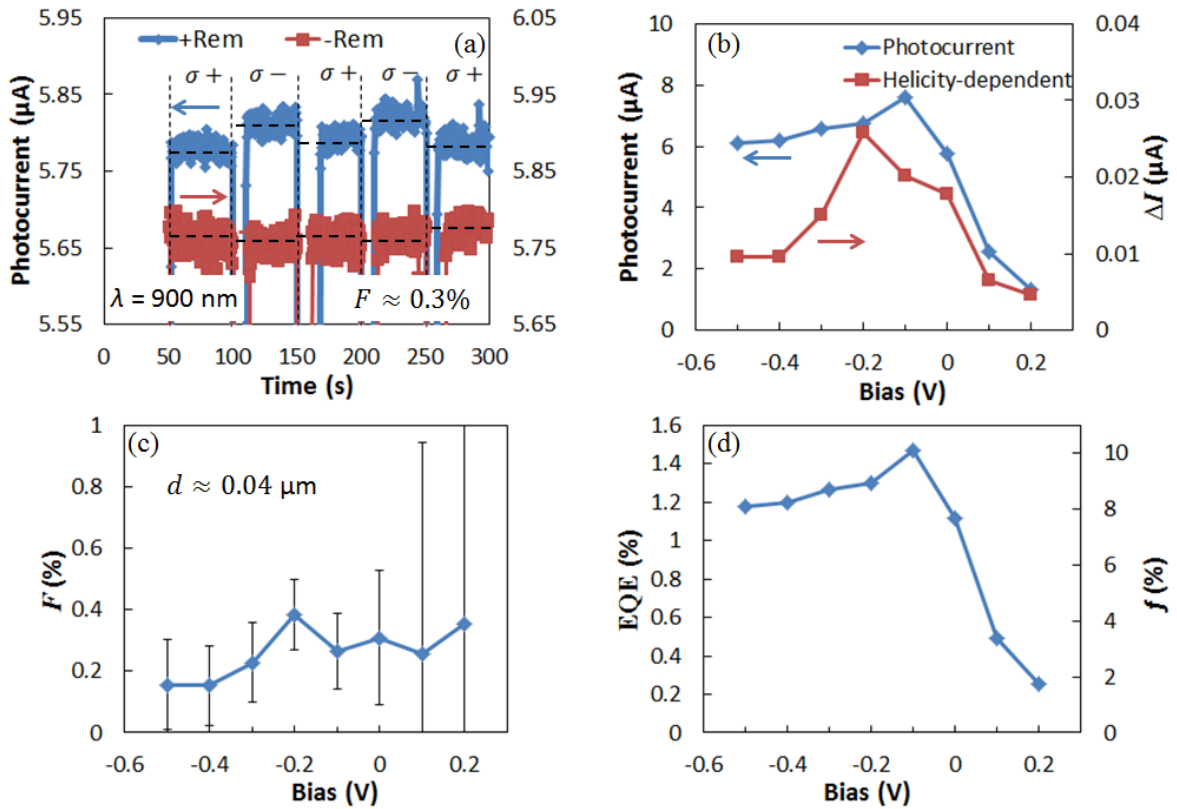


Figure 6.7 (a) Temporal plot of the measured photocurrent I_{ph} from a spin-PD with $d = 0.04 \mu\text{m}$ for two remanent magnetization states. Profiles were vertically separated for visibility. (b) Plot of I_{ph} and ΔI as functions of the applied bias voltage. (c) Plot of F as a function of bias. (d) Plot of the estimated EQE and f as functions of bias.

It can be seen that there is a discrepancy between the F ($\approx 0.4\%$) obtained in the simulation and the experimentally determined F ($\approx 19\%$). One factor whose effect is difficult

to assess in our simulations is the influence of possible defect in the p-InGaAs/ p-GaAs interface. These defects originate from dislocations caused by lattice mismatch between InGaAs and GaAs. In this case the mismatch is about $\Delta a/a_{\text{GaAs}} \approx 0.38\%$, for which a critical thickness of ≈ 40 nm is expected.¹¹ Since the InGaAs active layer thickness ($d \approx 400$ nm) in the present spin-PD is greater than the critical thickness, it is expected that dislocations would form in the InGaAs/GaAs interface. In order to address this issue, we have also prepared a spin-PD from the wafer with a thinner active layer ($d \approx 40$ nm) for which the defects should not be present. Shown in 6.7 (a) is measured photocurrent I_{ph} plotted against time from a spin-PD with $d = 0.04$ μm . No bias was applied. Again clear step-like profiles that indicate spin transport are observed. The $F \approx 0.3\%$ obtained here is comparable with that obtained from the earlier spin-PD with thick $d = 0.4$ μm , and no significant improvement was observed. This eliminates the defects from being the cause of the discrepancy between the simulated and experimental F .

Shown in Fig. 6.7 (b) is the bias dependence of I_{ph} and ΔI . In contrast with the earlier spin-PD with thick $d = 0.4\mu\text{m}$, here I_{ph} only slightly increase and then saturates with applied reverse bias, while ΔI increases and then starts to decrease with reverse bias. This further supports the hypothesis that the defects were significantly reduced (if not eliminated) by using a thinner active layer. Since there are no defects in the InGaAs/GaAs interface, even without bias, most the photogenerated spin-polarized carriers are already collected by the tunnel contact. Application of reverse bias only increases I_{ph} slightly since there are no more additional carriers to be collected. On the other hand, if there are defects in the InGaAs/GaAs interface, application of reverse bias would improve I_{ph} and ΔI , since the enhanced built-in electric field would counteract the carrier diffusion towards the defects, which is exactly what we observed with the spin-PD with thick $d = 0.4\mu\text{m}$.

Shown in Fig. 6.7 (c) is the bias dependence of F . We observe once again that F is nearly independent of the applied bias. More importantly, we note that F has an average value of $\approx 0.3 \pm 0.1\%$, which is comparable to that from the spin-PD with thick $d = 0.4\mu\text{m}$.

Shown in Fig. 6.7 (d) is the bias dependence of the EQE and f . Note again that the both EQE and f are proportional to I_{ph} by definition and hence have the same profile. What is interesting to note here is that, although EQE is low at about 1.4% at its highest owing to the low absorbance of the thin active layer, the f of about 8% at no bias is higher compared to that from the spin-PD with thick d ($f \approx 4\%$ at no bias). This is again consistent with the hypothesis that the defects are significantly reduced in the spin-PD with thin $d = 0.04\mu\text{m}$.

These results suggest that the origin of the low experimentally F is found elsewhere. Going back to the simulation, this time instead of using $P_{Fe} \approx 0.42$, we treat P_{Fe} as a fitting parameter to fit the simulation to the experimental F . From this, a P_{Fe} of about 1% was extracted. This means that in order to explain our experimental, we have to assume an effective spin polarization of 1%, which is 40 times lower than the literature value. This suggests that the quality of the Fe/AlO_x tunnel contact is poorer than what we expected. Incidentally, in an earlier report, poor spin-transport was also observed that for a NiFe/Al₂O₃/p-GaAs vertical-type spin-PD.¹² The paper did not state any conclusion on the cause of the poor spin-transport, but it should be noted that in their spin-PD the NiFe and Al₂O₃ were not crystalline. It can therefore be inferred that low F in the present work is caused by the poor crystalline property of the Fe/AlO_x tunnel contact. Consequently, this also means that depositing the Fe/AlO_x epitaxially should significantly improve the F . This, however, is outside the scope of the present work and is left for future study.

Lastly, for completeness, let us address the possible issue of MCD in our spin-PD. Due to the structure of the spin-PDs in the present study (where light is incident to the active layer from below), we can expect that the effect of MCD to F is much less significant than that of typical vertical-type spin-PDs (where light is transmitted through the ferromagnetic metal contacts). The only conceivable contribution of MCD would come from photons reflected off the top ferromagnetic metal contacts [from the Φ_2 term in Eqs. (6.4) and (6.8)]. Photons arriving into the active layer from below [the Φ_1 term in Eqs. (6.4) and (6.8)] cannot possibly possess an MCD component. Based on our previous study (discussed Ch. 5), where a similar top metal contact structure was used, the contribution of MCD to F is in the order of $\approx 0.5\%$ for oblique angle incidence. This value agrees with MCD estimates from other works.¹⁰ Let us first assume that the effect of MCD in present study is of comparable magnitude to that of our previous study (in the order of 0.5%). For the spin-PD with thick ($d = 0.4\ \mu\text{m}$) active layer, we estimate that, of the photons arriving at the active layer, 69.5% are absorbed during the first pass (Φ_1), 14% are absorbed by the top metal layers, 11.5% are absorbed during second pass (Φ_2), and 5% escape without being absorbed. If we apply the MCD to the Φ_2 portion, we expect an MCD contribution to F of about 7.1×10^{-4} . For the spin-PD with thin ($d = 0.04\ \mu\text{m}$) active layer, we estimate that, of the photons arriving at the active layer, 11.2% are absorbed during the first pass (Φ_1), 40.8% are absorbed by the top metal layers, 5.4% are absorbed during second pass (Φ_2), and 42.6% escape without being absorbed. If we now apply the MCD to the Φ_2 portion, we expect an MCD contribution to F of about 1.6×10^{-3} . For both thin and thick spin-PDs, the MCD contribution is expected to be

small compared to the experimentally measured F , which suggest that F is primarily due to spin transport. One may argue that if the MCD is say 3 % (an inconceivably high MCD value) then the MCD contribution to F would be around 0.4 % for the thick spin-PD. This, however, does not explain why the experimental F for both thin and thick spin-PDs are both around 0.4 % (the MCD contribution to F for the thin spin-PD would have to be at least 0.8 % in this case).

6.4 Conclusions

Here, we have proposed and demonstrated a novel Fe/AlO_x/p-InGaAs Schottky spin-PDs design with a refracting facet. An F of 0.4% has been experimentally achieved from measurements of the fabricated refracting-facet spin-PDs, which is the highest value so far for purely lateral spin-PDs. In addition to experiments, a simulation model for the refracting-facet spin-photodiode involving the optical selection rules, carrier and spin collection probability, and spin-dependent tunneling, has also been developed. Simulation results show that a potential F up to 19% is potentially achievable for the proposed spin-PD design. A comparison of the simulation and experimental results suggest that the quality of the Fe electrode is poor, and that an improvement of the electrode quality will lead to a significantly enhancement in the F .

References

- 1) H. Fukano, Y. Muramoto, and Y. Matsuoka, Jpn. J. Appl. Phys. **39**, 2360 (2000).
- 2) R. C. Roca, N. Nishizawa, K. Nishibayashi, and H. Munekata, submitted to JJAP (2017).
- 3) N. Nishizawa and H. Munekata, J. Appl. Phys. **114**, 033507 (2013).
- 4) D. Shaw, J. Electrochem. Soc.: Solid State Sci. Technol. **128**, 874 (1981).
- 5) T. Takeuchi, K. Makita, and K. Taguchi, IEEE Photon. Technol. Lett. **10**, 255 (1998).
- 6) C. Rinaldi, S. Bertoli, M. Asa, L. Baldrati, C. Manzoni, M. Marangoni, G. Cerullo, M. Bianchi, R. Sordan, and R. Bertacco, J. Phys. D: Appl. Phys. **49**, 425104 (2016).
- 7) M. I. Miah, Sci. Technol. Adv. Mater. **9**, 035014 (2008).
- 8) S. Rakheja, and A. Naeemi, IEEE Trans. Nanotechnol. **12**, 796 (2013).
- 9) H. Fukano, A. Kozen, K. Kato, and O. Nakajima, IEEE Electron. Lett. **32**, 2346 (1996).
- 10) C. Rinaldi, M. Cantoni, D. Petti, A. Sottocorno, M. Leone, N. Caffrey, S. Sanvito, and R. Bertacco, Adv. Mater. **24**, 3037 (2012).
- 11) J. Zou, D. J. H Cockayne, and B. F. Usher, J. Appl. Phys. **73**, 619 (1993).

R. C. I. Roca, A study on lateral-type spin-photodiodes... (August 2017)

12) T. Manago, Y. Suzuki, and E. Tamura, *J. Appl. Phys.* **91**, 12 (2002).

7. Conclusions

In this study, the performance of a cleaved edge Fe/AIO_x/p-GaAs Schottky junction lateral spin-PD has been investigated. In addition to conventional sidewall illumination experiments, oblique angle surface illumination measurements were also carried out. The spin conversion efficiency F has been determined to be 0.1% for sidewall illumination and 1.3% for oblique angle illumination. A simulation model incorporating the optical selection rules, drift-diffusion change and spin transport, and spin dependent tunneling has also been developed. Simulation results shows a good match between the experiment and simulation results for oblique angle illumination. Further comparison of the experimental and simulated results reveals that the low F for sidewall illumination is cause either by the damage in the AIO_x tunnel barrier at the cleaved edge or by magnetic edge curling. With this, we have successfully experimentally determined the origin of the low F in cleaved-edge spin-PDs and developed a device model for lateral spin-PDs.

Furthermore, a novel Fe/AIO_x/p-InGaAs Schottky spin-PDs design with a refracting facet has also been proposed and experimentally demonstrated. An F of 0.4% has been experimentally achieved from the fabricated refracting-facet spin-PDs, which is the highest value so far for purely lateral spin-PDs. In addition to experiments, a simulation model for the refracting-fact spin-photodiode involving the optical selection rules, carrier and spin collection probability, and spin-dependent tunneling, has also been developed. Simulation results show that a potential F up to 19% is potentially achievable for the proposed spin-PD

design. A comparison of the simulation and experimental results suggest that the quality of the Fe electrode is poor, and that an improvement of the electrode quality will lead to a significantly enhancement in the F . With this, we have successfully modelled and implemented an improved design for lateral spin-PDs.

Our results suggest that, in order to further improve the performance of the spin-PDs in general, additional studies at improving the quality of the spin dependent tunnel contact is necessary. At the present study, only an MBE grown AlO_x tunnel barrier has been used, but perhaps the use of more novel tunnel barrier materials such as MgO and MgAl_2O_4 might yield better results. In particular, MgAl_2O_4 has two advantages: it exhibits a spin-filtering effect when paired with an Fe electrode, and it has a close lattice parameter with both Fe and GaAs. These make MgAl_2O_4 a prime candidate for tunnel contact to GaAs based spin-optoelectronic devices.

Acknowledgements

I would like to acknowledge the scholarship support from the Ministry of Education, Culture, Sports, Science and Technology of Japan (MEXT) that made my doctoral study here in Japan possible.

I would like to thank Prof. Munekata for the constant supervision in research direction, Dr. Nishizawa for guidance in MBE, device process, and optical characterization experiments, and Dr. Nishibayashi for guidance in ultrafast optics experiments, and my labmates for their constant support and discussion.

I would also like to acknowledge Prof. Arnel Salvador who was my thesis adviser during my undergraduate and master's studies, one of my first mentors in science, and through whose recommendation I got a scholarship and got accepted in Tokyo Tech.

I would also like to thank members of my previous research laboratory, the semiconductor group of CMPL NIP. CMPL provided me a solid foundation and training for research in semiconductor and materials physics, which became vital in my graduate studies in Japan: Doc. Armando Somintac for the discussions, Ate Jenn Constantino for the training in device fabrication, and many others who have helped me in one way or another during my time at CMPL.

I also thank my family and friends for their support which I would not have made it without, especially:

to my parents who have always done their best, I can only hope to make them proud

to my brother whom I can always count on

to Maria Emma Villamin, who has always been there for me, for all the love and support.

I would also like to recognize that I could not have gotten this far without the help of countless unnamed people who have helped me along the way. I may not be able to name each of them, but I want to express my gratitude nonetheless.

And above all, to Him, who wrote the laws that all scientists endeavor to uncover and understand.

List of publications and presentations

Publications

- R. C. Roca, et al., “A lateral-type spin-photodiode based on Fe/ x -AlO $_x$ /p-InGaAs junction with refracting-facet side window”, Submitted to JJAP June 2017.
- R. C. Roca, et al., “Progress in the room temperature operation of GaAs-based lateral-type spin-PD in near-infrared wavelength region”, Accepted to Proc. SPIE 2017.
- R. C. Roca, et al., “Investigation of helicity-dependent photocurrent at room temperature from a Fe/ x -AlO $_x$ /p-GaAs Schottky junction with oblique surface illumination”, Jpn. J. Appl. Phys. **56**, 04CN05, Feb 24, 2017.
- H. Munekata, M. Aoyama, R. C. Roca, K. Nishibayashi, and N. Nishizawa, “Spin-photonic devices based on crystalline-AlO $_x$ /GaAs for emission and detection of circularly polarized light”, Proc. SPIE 9551, 955120, Sep 8, 2015.

International Conferences

- R. C. Roca, et al., “Refracting-Facet Spin Photodiode based on Fe/ x -AlO $_x$ /p-InGaAs Schottky Junction”, SpinTECH IX, B-64, Jun 8, 2017.
- R. C. Roca, et al., “Highly Efficient Helicity-dependent Photocurrent at Room Temperature using a Fe/ x -AlO $_x$ /p-GaAs Schottky Junction”, SSDM 2016, C-5-04, Sep 29, 2016.
- H. Munekata, R. C. Roca, K. Nishibayashi, and N. Nishizawa, “Progress in the room temperature operation of GaAs-based lateral-type spin-LED and spin-PD in near-infrared wavelength region”, SPIE Spintronics X, 10357-47, Aug 8, 2017.
- N. Nishizawa, R. C. Roca, M. Aoyama, K. Nishibayashi, and H. Munekata, “Semiconductor-based spin-photonic devices for emission and detection of circularly polarized light at room temperature”, SPIE Spintronics IX, 9931-2, Aug 28, 2016.

Domestic Conferences

- R. C. Roca, et al., “Simulation of an edge-illuminated refracting-facet spin photodiode”, 64th JSAP Spring Meeting, 15a-501-10, Mar 15, 2017.
- R. C. Roca, et al., “Helicity dependent photocurrent at RT from a Fe/ x -AlO $_x$ /p-GaAs Schottky Junction”, 63rd JSAP Spring Meeting, 14p-W241-4, Mar 19, 2016.
- R. C. Roca, et al., “A Phenomenological model for the helicity dependent photocurrent in a ferromagnet-insulator-semiconductor junction”, 62nd JSAP Spring Meeting, 14p-D2-1, Mar 2, 2015.

Curriculum Vitae

Ronel Christian Intal Roca

Doctoral Student

Munekata Laboratory (宗片研究室)

Department of Electronics and Applied Physics (物理電子システム創造専攻)

Interdisciplinary Graduate School of Science and Engineering (大学院総合理工学研究科)

Tokyo Institute of Technology (東京工業大学)

4259 Nagatsuta-cho, Midori-ku, Yokohama City, Kanagawa, 226-8503, Japan

General

Date of Birth: January 25, 1987 (Age: 30)

Nationality: Philippines

Sex: Male

Marital Status: Single

Languages: Filipino (Tagalog), English, and Japanese (Intermediate)

Education

University of the Philippines Diliman — Bachelor of Science in Physics June 2003 — April 2008

Thesis title: Fabrication and Characterization of Planar Square-Spiral
Micro-Inductors on SI GaAs for MMIC Applications

University of the Philippines Diliman — Master of Science in Physics June 2008 — May 2010

Thesis title: Fabrication and Characterization of Passive Integrated Circuit
Filters for Gallium Arsenide based Microwave Applications

Tokyo Institute of Technology — Research Student April 2014 — Sept 2014

MEXT Research Scholarship Recipient

Japanese Language Intensive Course Student at Tokyo Tech

Tokyo Institute of Technology — Doctor of Engineering Oct 2014 — Sept 2017

MEXT Research Scholarship Recipient

Dissertation Title: A study on lateral-type spin-photodiodes based on
metal-insulator-semiconductor junctions

Work Experience

University of the Philippines Diliman — Instructor Nov 2008 — May 2011

Faculty member of the National Institute of Physics

Courses Taught:

- Electromagnetism, wave phenomena, and optics lecture and laboratory classes.
- Thermal Physics, relativity, and quantum mechanics recitation classes.

Hitachi Global Storage Technologies Philippines Corp. — Senior Engineer Sept 2011 — March 2014

Member of Design of Experiment Team in Head Prototyping Department

- Developed method of advanced characterization of hard disk drive heads based on magnetic force microscopy (MFM).

- Developed method advanced characterization of hard disk drive heads using Wyko optical profilometer and atomic force microscope (AFM).

Tokyo Institute of Technology— Research Assistant

Jan 2016 — March 2017

Supported maintenance of laboratory

- Managed laboratory chemicals (procurement, storage, organization, and disposal).
- Helped maintain cleanroom.
- Managed disposal of waste materials from experiments.

Tokyo Institute of Technology— Teaching Assistant

April 2017 — July 2017

Teaching support for undergraduate and graduate classes

- Preparation and clean-up of class materials.
- Proctoring during examinations.

Skills & Abilities

- Growth of III-V compound semiconductors by MBE (RIBER).
- Fabrication of semiconductor devices including: standard photolithography, vacuum metal deposition, and wet and dry etching techniques.
- Electrical and optical characterization of GaAs semiconductor optoelectronic devices including: circular polarization resolved electroluminescence (EL), photocurrent (PC), and photoluminescence techniques (PL).
- Structural characterization of semiconductor materials: Wyko, AFM, SEM, and XRD.
- Magnetic characterization by SQUID (Quantum Design MPMS machine)
- Numerical simulation of semiconductor devices (using MATLAB, SCILAB, or Mathematica).

References

- Hiro Munekata (Doctoral Supervisor)
Professor, Tokyo Institute of Technology
4259-J3-15, Nagatsuta, Midori-ku, Yokohama 226-8503
e-mail: munekata.h.aa@m.titech.ac.jp
- Arnel Salvador (BS and MS Thesis Advisor)
Professor, University of the Philippines Diliman
National Institute of Physics, University of the Philippines Diliman Quezon City, 1101, Philippines
e-mail: asalvador.nip@gmail.com
- Butch Jandayan (Direct Supervisor)
Senior Manager
HGST, a Western Digital company Philippines Corp.
SEPZ, Laguna Technopark, Biñan, Laguna, Philippines
e-mail: butch.jandayan@wdc.com